UNIVERSITÀ DI PARMA

UNIVERSITA' DEGLI STUDI DI PARMA

DOTTORATO DI RICERCA IN

"Scienza e Tecnologia dei Materiali"

CICLO XXXII

TAILORING CALCIUM PHOSPHATE NANOPARTICLES FOR MEDICAL APPLICATIONS: A FUNCTIONAL BY DESIGN APPROACH

Coordinatore:

Chiar.mo Prof. Enrico Dalcanale, PhD

Tutore:

Dott.ssa Monica Sandri, PhD

Co-tutore:

Dott. Michele Iafisco, PhD

Dottorando: Lorenzo Degli Esposti, M. Sc.

Anni 2016/2018

Table of contents

AIM OF THE WORK

Medicine is a field in continuous expansion as the molecular and genetic causes of pathologies are discovered and new therapeutic treatments are developed. On the viewpoint of material science there is an ever-growing demand of new advanced materials such as therapeutic agents, tissues substitutes, regenerative agents, and as component of biomedical devices. The materials must have at the same time excellent properties, minimal costs, and do not have side reactions with the biological environment. For this reason there is a high interest in nanomaterials for medicine, since these advanced materials promise to have all of the above-mentioned features. However, the development of nanomaterials designed to have specific functions is a complex process. Nano-objects cannot be processed or controlled directly, and their behavior and properties fall in between the domain of chemistry and physics. A lot of research effort is devoted on understating and controlling nanomaterials characteristics in order to fulfil the requirements of nanomedicine.

The research activity reported in this Ph. D. Thesis was focused on the development of new calcium phosphate nanomaterials for medical application. The research was carried out at the Institute of Science and Technology for Ceramics, belonging to the National Research Council of Italy (ISTEC C.N.R.) under the supervision of Dr. Michele Iafisco. The materials presented in this Ph. D. Thesis possess different physicochemical properties and are employed in very different applications, but were all developed with the "*functional by design*" approach. This novel approach, which is the basis of this Ph. D. Thesis, is based on the concept that the nanomaterial is knowingly designed and tailored to fulfil a specific function. The functional by design approach was achieved through a bottom-up preparation of nanoparticles employing organic and inorganic templates to tailor nanoparticles physicochemical properties.

The first part of the Ph. D. work was dedicated to the design of calcium phosphate nanoparticles for cardiac drug delivery. Nanoparticles were designed to encapsulate a biomolecular drug and to deliver it to the cardiac district for treating cardiovascular diseases. Furthermore, the nanoparticles design allowed drug delivery through the inhalation route, which proved to be more effective and pain-free than the conventional parenteral administration routes. The second part of the Ph. D. work was focused on the design of calcium phosphate nanoparticles for enamel remineralization and dentin desensitization. The nanoparticles were tailored to quickly dissolve in the mouth environment and to form a new fluorine-doped mineral phase onto enamel and dentine, thus restoring enamel resistance and occluding exposed dentinal tubules. The third part

of this Ph. D. work was devoted to basic research on calcium phosphate nanoparticles formation, with the aim to deepen the knowledge on nanoparticles crystallization and growth in presence of template molecules. Calcium phosphate nanoparticles nucleation, growth and maturation in presence of one or more regulator molecules has been thoroughly studied in order to understand the effect such regulators.

List of acronyms

ACP: Amorphous Calcium Phosphate

ANOVA: One-Way Analysis of Variance Test

ATP: Adenosine Triphosphate

BET: Brunauer–Emmett–Teller theory

CaP/CaPs: Calcium Phosphate(s)

CaP NPs: Calcium Phosphate Nanoparticles

Cit-HA: Citrate-Hydroxyapatite

CitOH-HA: Hydroxycitrate-Hydroxyapatite

CMC: Carboxymethyl Chitosan

CPP: Casein Phosphopeptides

CVDs: Cardiovascular Diseases

Cy7: Sulfo-Cyanine 7 Amine Fluorophore

DCPD: Dicalcium Phosphate Dihydrate

DLS: Dynamic Light Scattering

DNA: Deoxyribonucleic Acid

ECG: Electrocardiogram

EDS: Energy Dispersive Spectroscopy

EPR: Enhanced Permeation and Retention effect

FACP: Fluoride-doped Amorphous Calcium Phosphate

FBS: Fetal Bovine Serum

FHA: Fluoro-hydroxyapatite, Fluorapatite

FMT: Fluorescence Molecular Tomography

FT-IR: Fourier Transform Infra-Red Spectroscopy

FWHM: Full Width Half Maximum peak parameter

GERD: Gastroesophageal Reflux Disease

Glr: Glutaric Acid

Glr-HA: Glutarate-Hydroxyapatite

HA: Hydroxyapatite

HEPES: 4-(2-Hydroxyethyl)-1-Piperazineethanesulfonic acid

HRTEM: High Resolution Transmission Electron Microscopy

ICP-OES: Inductively Coupled Plasma Optical Emission Spectroscopy

IL: interleukin

ISE: Ion selective electrode

K_3(CitOH): Potassium Hydroxycitrate Tribasic Monohydrate

LTCC: L-Type Calcium Channel

LV: Left Ventricle

Mg,Sr-FACP: Magnesium and/or Strontium doped, Fluoride-doped Amorphous Calcium Phosphate

MIP: Mercury Intrusion Porosimetry

MRI: Magnetic Resonance Imaging

Na_3(Cit): Sodium Citrate Tribasic Dihydrate

NIR: Near-Infrared

NIST: National Institute of Standards and Technology

NPs: Nanoparticles

OCP: Octacalcium Phosphate

PBS: Phosphate Buffered Saline solution

PEG-PLA: Poly(Ethylene Glycol)-block-Polylactide

PET: Positron Emission Tomography

Peptide HA: Hemagglutinin Peptide YPYDVPDYA

Peptide MP: Mimetic Peptide DQRPDREAPRS

Peptide R7W-MP: Arginin-modified Mimetic Peptide RRRRRRRDQRPDREAPRS

PXRD: Powder X-Ray Diffraction

RNA: Ribonucleic Acid

SAED: Selected Area Electron Diffraction

SEM: Scanning Electron Microscope

SSA: Specific Surface Area

STED: Stimulated Emission Depletion 3D z-stack microscopy

STZ: Streptozotocin

TEM: Transmission Electron Microscope

TGA: Thermogravimetric Analysis

TISAB: Total Ionic Strength Adjustment Buffer

TNF: Tumor Necrosis Factor

Chapter 1. Introduction

1.1 Nanomaterials

Nanomaterials are defined as materials that possess at least one dimension in the nanometer scale ($1*10^{-9}$ – $1*10^{-6}$ m; in general, the research interest is focused in the range between $1*10^{-9}$ and $5*10^{-7}$ m). Depending on the number of dimensions in the nanometer scale the material can be defined as nanoplate (one-dimensional nanomaterial), nanofiber (two-dimensional nanomaterial) of nanoparticle (NP, three-dimensional nanomaterial) [1]. Nanomaterials possess several unique features that are strictly related to their dimension and are not present in their bulk counterpart. First, nanomaterials have an enormous surface-to-volume ratio, which means that surface properties are much more relevant than in bulk materials. Second, nanomaterial can exhibit special quantum-mechanical properties related to their high surface-to-volume ratio such as electron spatial confinement. Third, nanometric dimension facilitate colloidal stability, since Brownian motion becomes more influent than gravitational force. Furthermore, nanomaterials have a different behavior in the organism compared to their micro- or macroscopic counterpart, which will be discussed in the section 1.2.

The unique properties of nanomaterials have been harnessed for several advanced applications, ranging from medicine to energy, electronics, environment, agriculture, and industrial production [2-5]. The application of nanomaterials to these fields should have an enormous impact, but there are some hurdles that are to be taken into account. First, nanomaterials could have a noxious influence on human health. This topic will be discussed in detail in section 1.2. Second, the ultra-small dimensions of nanomaterials require special techniques to be manufactured, since these materials could not be handled like bulk materials. Nanomaterials can be prepared with a "top-down" or a "bottom-up" approach [6]. In top-down approach, also called physical method, the nanomaterials are prepared from bigger objects that are progressively "divided" until nano-dimensions are reached.

Part of the content of this chapter has been published in Drug development and industrial pharmacy 2018, 44(8), 1223-1238 as "*Degli Esposti L., Carella F., Adamiano A., Tampieri A., Iafisco M. Calcium phosphate-based nanosystems for advanced targeted nanomedicine*", in Nanotechnologies in Preventive and Regenerative Medicine (Elsevier Publishing 2018) as *"Degli Esposti L., Tampieri A., Iafisco M. Nanostructured calcium phosphates for theranostic nanomedicine"*, and in Electrofluidodynamic Technologies (EFDTs) for Biomaterials and Medical Devices (Woodhead Publishing 2018) as *"Degli Esposti L., Carella F., Iafisco M. Inorganic nanoparticles for theranostic use"*

Typical examples of top-down nanomaterial preparation are photolithography and micro-machining. Top-down approach allows a great control on nanomaterials morphology, but it is energy and time consuming, is a highly inefficient method (nano-objects are manufactured one at a time) and it does not allow to reach the smallest size range (current resolution is above 50 nm). On the other hand the bottom-up approach, also called chemical approach, starts with either a solution or a vapor of atoms, molecules, or precursors that react to form the nanomaterial population [6]. With this method the nanomaterials are formed and grown from the controlled assembly of building blocks. Some typical examples are growth from melt or solution, chemical vapor deposition, and self-assembly of supramolecular units. The bottom-up approach allows to form nanomaterials with smaller size (the size limit depends on the nature of the material and the fabrication process) and with high efficiency (moles of nanomaterials are manufactured at the same time). However, with this approach is complex to control nanomaterials dimensions, morphology, and properties and often it is needed the use of advanced material processing technologies or the use of templates, chemical species that direct and control building blocks union and growth. However, the advantages of bottom-up approach are more than the hurdles and for this reason the materials science research is more focused on this approach. This Ph. D. work inserts in the field of research on nanomaterials preparation and characterization using bottom-up approach, producing nanomaterials for medical application.

1.2 Medicine and Nanomedicine – The perspective of a material scientist

According to the European Technology Platform, “nanomedicine” is defined as the application of nanotechnology and nanomaterials to address healthcare problems. The unique and novel properties displayed by materials at the nanoscale that were discussed above are harnessed to achieve performances, specificity, and biological activity not achievable by materials at the bulk scale [7]. An unique property of nanomaterials is that when are administered in the human body their nanometric dimensions allow a prolonged circulation in the bloodstream escaping the capture from macrophages or other cells of the reticuloendothelial system avoiding a rapid clearance and improving circulation time [8, 9]. In addition, nanomaterials are able to easily penetrate in tissues and cells and have fewer chances to be entrapped in the excretory system. Some NPs are also able to pass the notoriously extremely selective hemato-encephalic barrier, which is one of the biggest obstacles in the brain disorders treatment [10]. In general, NPs smaller than 100 nm in diameter have been suggested to be ideal or nanomedicine because of their favorable biodistribution and clearance/accumulation behavior. There features of

nanomaterials make nanomedicine a very promising discipline that could allow ultra-localized drug administration, early diagnosis of pathologies, precise disease site localization and *in situ* treatment. So nanomedical therapies could have lower risk of side effects, minimal or null damage of healthy tissues, decreased administered doses, limit the use of invasive surgery, and simpler drug administration causing less stress and discomfort for the patients. Furthermore, with nanomaterials a "personalized medicine" could be achieved, where the drug dosage and effects are tailored on the needs of the patient. It must be pointed out that these properties of nanomaterials are related not only to the dimensions and morphology, but also to composition, solubility, and surface characteristics as hydrophilic-lipophilic balance, surface charge, etc. [11]. For example, on the basis of surface charge NPs could undergo reticuloendothelial system uptake, nonspecific sticking to cells, or be taken up by scavenger endothelial cells in the liver [9]. So there is a strong demand to the material scientist to design nanomaterials with controlled morphological and physicochemical properties to fulfil the criteria established by the clinician.

It must be taken into account that the nanomaterial's excellent penetration and diffusion properties can be also a health risk [12]. The long-term toxicity of several nanomaterials has not been elucidated yet; thus, their capacity to penetrate into tissues could become a double-edged sword as non-biodegradable nanomaterials can accumulate in healthy tissues inducing inflammatory and toxic effects [13, 14]. Some examples are inhaled ultrafine particles can induce pulmonary inflammation, oxidative stress, and even cardiotoxicity [15]. Several NPs can induce ROS generation, which is currently the main concern for nanoparticle toxicity [16]. Nowadays there is a high interest on "nanosafety", that means to say to assess the long and short term toxicity of nanomaterials on human organism and the environment [17]. Indeed, the biological impact of nanomaterials and the biokinetics of NPs are dependent on size, chemical composition, surface structure, solubility, shape, and aggregation. These parameters can modify cellular uptake, protein binding, translocation, and the possibility of causing tissue injury. So there is a strong demand to the material scientist to control nanomaterials properties not only for exerting a beneficial effect, but also for reducing potential noxious effects.

1.2.1 Drug delivery

The first and most studied application of nanomaterials in medicine is drug delivery, that means to say that the NPs act as a carrier of a drug toward a target site. The function of the nano-carrier is to bind and deliver the therapeutic agents and thus to offer a protection of the payload against a possible immediate degradation in the bloodstream, and using their superior biodistribution to deliver the payload to the disease site [18]. In addition, drug delivery nanomaterials can transport hydrophobic drugs increasing drug bioavailability, or reduce side effects (e.g. cardiotoxicity, nephrotoxicity, and hepatotoxicity) of highly cytotoxic drugs (e.g. antineoplastic drugs) by minimizing drug interaction with healthy cells and tissues [19-21]. Moreover, nanomaterials' enormous surface-to-volume ratio allows a high relative drug loading, thus leading to high therapeutic activity with small doses [22]. Advanced drug delivery nanosystems can also have triggered drug release mechanisms, in order to have drug administration localized in diseased areas alone. One of the strategies developed for this purpose is to use materials that are responsive to environmental stimuli such as temperature, pH, or redox activity. Another strategy is to design nanomaterials that are responsive to external stimuli such as light (photodynamic therapy), magnetic fields (hyperthermia), or high-energy particles (neutron capture therapy) [23].

Several families of drugs were used as payload for nano drug delivery. The most studied drugs were chemotherapeutic agents, since cancer is among the leading cause of morbidity and mortality worldwide, according to World Health Organization data. Agents for cancer therapy must be extremely efficient due to the large variety and radical variances of the different kinds of tumor as well as the overproliferative nature of cancerous cells. However, the current therapeutic agents are extremely toxic, nonspecific, invasive, and damage also healthy tissues, causing prolonged treatments and hospitalization. For this reason drug delivery of chemotherapeutic agents has been one of the most studied field since the birth of nanomedicine [24]. Among the most used chemotherapeutic agents loaded onto NPs are doxorubicin [25, 26], platinum complexes [27], and methotrexate [28]. Another class of therapeutic agents that could have great benefits from drug delivery are biomolecules. Recent development in molecular biology and biotechnology have shown that several biomolecules, especially polypeptides and polynucleotides, could have a therapeutic effect by correcting dysregulated levels of proteins or nucleic acid, by inhibiting pathological protein activity or silencing pathological gene expression, or by adding new genes to replace defective genes [29]. Drug delivery of biomolecules has a twofold beneficial effect. First, with nano-carrier the biomolecules are more easily translocated from the administration site to inside the cells or

nuclei in the target tissues. Second, the nano-carrier can protect the payload from degradation in the biological environment. This feature is particularly relevant, since biomolecules can be easily degraded by peptidases and nucleases before reaching their target site [30].

1.2.2 Imaging and Theranostics

Another use of nanomaterials in medicine is for medical imaging. NPs for this application emit a signal that can be visualized through an imaging technique and can be tracked in the organism. This allows non-invasive real-time monitoring of NPs *in vivo* [31]. The monitoring of NPs behavior is essential to clearly assess their bio-distribution, namely tissue penetration, organ accumulation, and excretion; these information are the key-points of important pharmacodynamics aspects of NPs such as hematic lifetime, drug delivery kinetic, toxicity, specificity, and efficacy [32]. However, the main application of NPs for imaging is the localization and visualization of a target site, e.g. a pathologic tissue. In this case the NPs must accumulate preferentially in the target site, thus enhancing the imaging contrast in comparison with other tissues. For example, imaging plays a fundamental role in cancer therapy, from diagnosis, to the pinpointing of diseased areas during treatments, and extending to post-treatment monitoring. The primary objective of tumor imaging is to pinpoint tumor location at the earliest possible stage since the accurate diagnosis of cancer in its earliest stages is of extreme clinical importance to avoid tumor metastatization. NPs for medical imaging have several advantages in comparison with conventional imaging agents. Materials at the nano scale possesses unique optical, magnetic, and chemical properties that allow the creation of imaging probes with increased density, amplification, and quantification of the signal, as well as with improved contrast [31]. In this domain, NPs are efficiently used as imaging agents in magnetic resonance imaging (MRI) [33], positron emission tomography (PET) [34], and near-infrared (NIR) adsorption [35]. Moreover, advanced imaging NPs are often designed to provide multiple diagnostic signals at the same time (i.e., a combination of MRI and PET), because each one can have different advantages such as spatial resolution, tissue penetration, noise-to-signal ratio or can deliver a different diagnostic insight, expanding the field of available information [36].

In addition, nanomaterials can also be “theranostic” agents, which can fulfill a therapeutic action and at the same time deliver diagnostic information through imaging [37]. Theranostic agents are designed to contain both diagnostic and therapeutic functions in a single integrated system that is capable to exert a therapeutic functions and at the same time to provide a noninvasive *in vivo* monitoring of the local environment (Figure 1.1). So the theranostic agents enable to “see”

(i.e., predict, treat, monitor) the disease in the patient, that differs case by case in terms of gravity, site of interest, and extension. Therefore, this *ad hoc* disease management could allow to treat patients according to the situation and in the best way in terms of dosage, number of treatments, relapse control, etc. maximizing therapeutic action and minimizing side effects and discomfort.

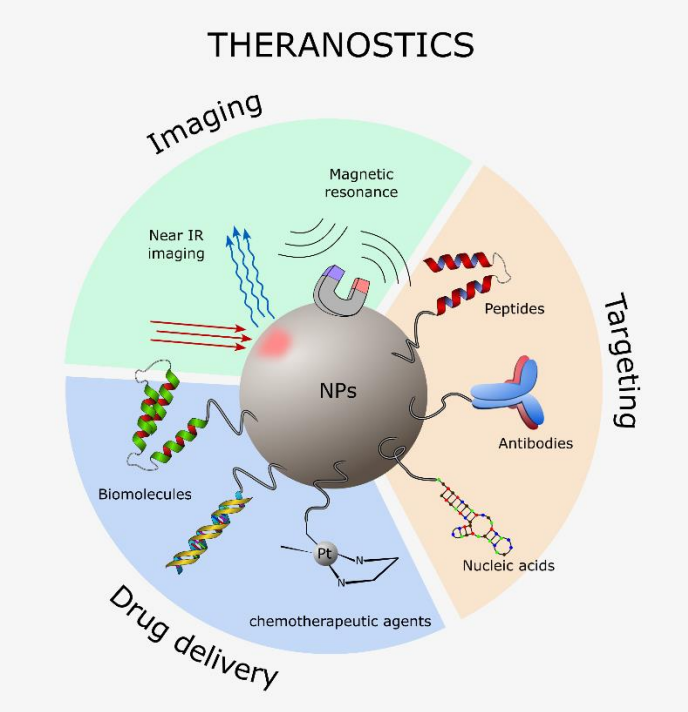

Figure 1.1. Schematic representation of a theranostic nanosystem.

1.2.3 Targeting

The efficacy a nanomaterial for drug delivery or imaging can be further incremented by making it tissue or disease specific, called "targeting". This means that the NPs are able to accumulate only in the desired tissues, and/or perform their action only if the environment is in pathological conditions [38]. The benefit of targeting in the case of drug delivery is that the nano-carrier is localized only in the regions of interest, thus minimizing drug accumulation in off-target organs that could lead to cytotoxicity effects. In case of NPs for imaging the targeting would improve the signal in the pathological region and decrease aspecific signal, improving resolution and giving a precise localization. There are several approaches to induce a targeting effect. First, it must be mentioned that nanomaterials are naturally targeted for tumors through the enhanced permeation and retention (EPR) effect, consisting in their spontaneous accumulation in the leaky

and over-vascularized cancerous tissues [39]. However this form of targeting, that is called “passive targeting”, is not always efficient because the degree of tumor vascularization and porosity of tumor vessels can vary within tumor types and conditions [40, 41]. Furthermore EPR effect does apply only to cancerous diseases. The most promising and efficient approach to improve the specificity of NPs is the “active targeting” method, where a targeting moiety is added as surface decoration of the NPs. The targeting moiety is a molecule capable to recognize and bind with high efficacy and selectivity to receptors overexpressed or expressed only by specific cells, usually pathologic cells (Figure 1.2) [42, 43]. Once the NPs functionalized with the targeting molecules arrive near the target cells, they interact with membrane receptors on cells surface via ‘targeting moiety-receptor’ mechanisms and, in some cases, penetrate in the cells by specific receptor-mediated internalization processes. Consequently, NPs exert their therapeutic effect in close proximity or inside the target cells [42-44]. Several targeting moieties have been exploited to achieve active targeted NPs [45]. The most studied targeting moieties include monoclonal antibodies [46], antibody derivatives [47], peptides [48], aptamers [49], transferrin [50], carbohydrates [51], and small organic molecules [52]. Some of the above mentioned targeting moieties have a specific target receptor, for example transferrin, carbohydrates and small molecules are usually related to cell metabolism and their receptors are overexpressed in hypermetabolic cells like tumor cells. On the other hand, other targeting moieties can be “custom-made”, that means to say that are designed and produced to target a chosen receptor, thus allowing to target every tissue or pathology. Examples of this latter category of targeting agents are monoclonal antibodies, aptamers, and peptides.

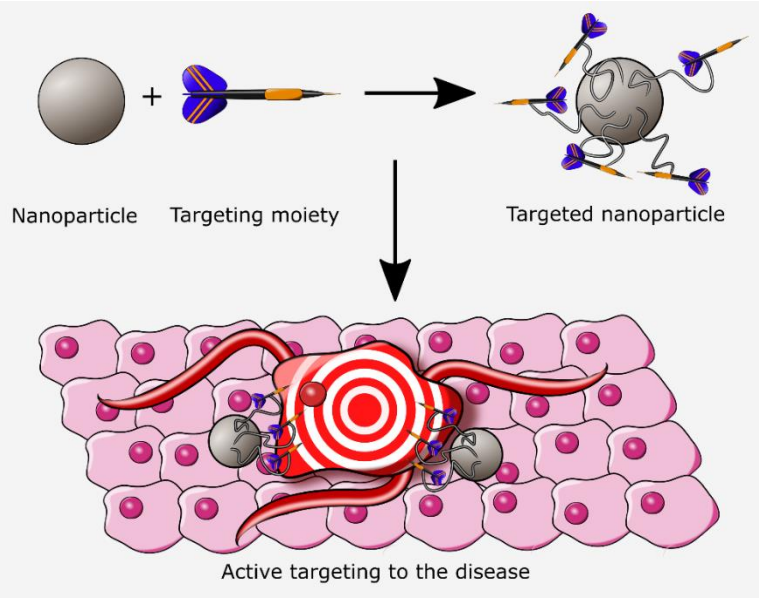

Figure 1.2. Schematic representation of active targeting.

1.3 Nanoparticles in human body: hard tissue biomineralization

Some nanomaterials are natural-occurring, and some of them are synthesized by living organisms. The process of formation of nanomaterials *in vivo* can be a source of inspiration for the production of synthetic nanoparticles. The research work reported in this Ph. D. Thesis is inspired by the process of formation of nanoparticles during calcification of hard tissues, called biomineralization. Biomineralization consists in the formation of inorganic crystals in a biological matrix [53]. In chordates, calcium phosphates (CaPs) are the main inorganic constituent of normal (bone, dentine, fish scales, horns of different animals) and pathological (e.g. dental and urinary calculi, tendon mineralization, calcification of blood vessels) calcifications [54]. Natural CaPs occur in the form of ionic substituted, poorly crystalline hydroxyapatite nanocrystals, with the exception of enamel that is composed by nanocrystals with high degree of crystallinity [55]. In this Ph. D. Thesis calcium phosphates nanocrystals and nanoparticles will be defined as *CaP NPs*.

CaP NPs crystallization in biological tissues is still far from being fully comprehended. In bone, the biomineralization is controlled to by osteoblast cells and the organic matrix made by those cells. The cells have the function to produce the organic matrix, control the flux of ions in the mineralization region, and register and emit the signals that control the beginning and end of the mineralization process [53]. The main structural unit of the organic matrix is collagen type I, an insoluble fibrous protein that self-assembles in a repeating triple-helical fibril (tropocollagen). The tropocollagen is arranged in a staggered head-to-tail disposition with other fibrils [53]. The hydroxyapatite nanoparticles nucleate in the holes between the individual collagen molecules and between the tropocollagen fibrils. After nucleation, hydroxyapatite nanocrystals are confined in the hole zones and grow as nanoplatelets, approximately 45 nm in length, 20 nm in width and 3 nm in thickness. The individual nanocrystals are oriented in respect of collagen matrix, such as the crystallographic *c* axis and particle length axis is oriented along fibril axis and the crystallographic *a* axis and particle width axis is oriented along fibril groove [53]. Afterward, the apatite nanocrystals grow within the holes and then spread throughout the collagen matrix. The control on hydroxyapatite nanocrystals nucleation, morphology, dimensions, orientation, and growth inside tropocollagen fibrils is thought to be exerted by collagen, non-collagenous proteins, other organic molecules, and the extracellular fluid ionic concentration. Non-collagenous proteins are an ensemble of water-soluble proteins whose the more relevant families are proteoglycans, glycoproteins, and γ-carboxy-glutamic acid-containing proteins [56]. These proteins and polysaccharides have several anionic sites that could bind Ca^{2+} ions, and at the same time tend to bind to specific sites of collagen [53, 57]. However, hydroxyapatite

nanocrystals biomineralization in bone is a very complex process and the precise effect of the above-mentioned components is still under investigation. Furthermore, the effect of small organic molecules has been often undervalued; for example, only recently it has been proved the molecule of citrate has a strong influence on biomineralization.

1.3.1 Role of citrate in biomineralization

For a long time it was thought that the main regulators of hydroxyapatite nanocrystals growth during bone tissue biomineralization were mainly collagen and non-collagenous proteins. However, even if both types of proteins are surely involved in biomineralization [56], none of them could limit nanocrystal thickness to the values observed in nature (approx. 3-5 unit cells). In detail, collagen holes are much larger than nanocrystals thickness and the non-collagenous proteins are not sufficiently abundant *in vivo* to bind to nanocrystal surfaces at concentrations high enough to inhibit thickness growth [58]. Recently, Hu *et al.* have proven that citrate (2-hydroxypropane-1,2,3-tricarboxylic acid) is strongly immobilized on bone apatite nanocrystal surfaces, with an approximately density of coverage of one molecule per 2 nm^2 [58]. Citrate is a relatively abundant non-macromolecular organic component of bone, approx. 5.5 wt% of bone organic fraction, and thus it could provide more COO^- groups for binding to calcium of apatite than all bone non-collagenous proteins together. The work suggested that strongly bound citrate molecules could interfere with the crystal thickening and stabilize the size of the hydroxyapatite nanocrystals in bone [58], and has prompted high interest on understanding the effect of this molecule. Further works have suggested that citrate could also help to stabilize the amorphous clusters that are the precursor of bone apatite and to facilitate interfacial compatibility between nonpolar proline and alanine residues of the collagen matrix and hydroxyapatite nanocrystals surface by making it more hydrophobic [59]. However, these hypotheses must be confirmed by *in vivo* data. *In vitro* experiments have proven that citrate has a strong effect on hydroxyapatite nanocrystals formation. These studies have proved that citrate plays a dual role in hydroxyapatite nanocrystals crystallization, driving the growth via an amorphous precursor and inducing a non-classical oriented aggregation of the nanocrystals [60-63], although the aggregation could be influenced by the hydrated ionic layer on the surface of apatite. In addition, synthetic citrate-apatite nanocrystals were proven to possess a platy morphology, suggesting that a similar mechanism might occur in bone mineralization [63]. The influence of citrate on hydroxyapatite nanocrystals formation and growth is a critical topic in this Ph. D. Thesis that will be discussed in detail in the next chapters.

1.4 Calcium phosphate nanomaterials: a multipotent material in medicine

Synthetic CaPs are probably the most important compounds for biomaterials applications, due to their chemical similarity with the inorganic component of bone and teeth, as well as excellent biological properties, such as biocompatibility, bioactivity, lack of toxicity or inflammatory and immunity responses, osteoconductivity, osteoinductivity, and also tailorable biodegradability. For this reason, CaP were mainly studied for hard tissues substitution and regeneration [55, 64]. It is interesting to point out that when CaPs are prepared in mild conditions the products naturally tend to be in the form of nanoparticles or nanocrystals with dimensions that not exceed 500 nm. For this reason CaP NPs were recently proposed as novel material for nanomedicine, thus for biomedical applications not strictly connected to bone. In the last decades CaP NPs were successfully employed in drug delivery, gene delivery, vaccination, imaging, and theranostic for the treatment of tumors, autoimmune diseases, cardiovascular diseases, and for restoring mineralized tissues [30, 65-71].

1.4.1 Nanomedicine

CaP NPs have several advantages that make them a promising material for nanomedicine. As mentioned above CaP NPs have superior biological compatibility in comparison to other kinds of inorganic nanomaterials [72]. In addition, CaP NPs do not over-accumulate in the filtering organs on a long time scale on the contrary to what happens with non-degradable inorganic NPs such as quantum dots, metal clusters and metal oxides that could lead to toxic effects [73]. This feature is due to the fact that CaP NPs are slowly degraded by the cells, with a release of non-toxic calcium and phosphate ions. At the same time CaP NPs are much more stable than synthetic liposomes or similar organic nanomaterials and can be more resistant to damage in the organism [74]. It is important to remark that some synthetic CaP NPs, designed to have a high similarity (in terms of chemical composition, crystal structure, and morphology) with the mineral phase of bone, the so-called “biomimetic” CaP NPs, are more appealing materials for nanomedical applications respect to their non-biomimetic counterparts. In fact, optimal characteristic of CaP NPs in terms of biocompatibility, biodegradability, and bioactivity can be achieved by improving their biomimetism, that is to say by preparing them with similar dimensions, morphology, crystallinity, and physicochemical properties as for biological ones [75]. In principle, the organisms can recognize biomimetic CaP NPs as a sort of endogenous materials, thus leading to a totally positive biological response.

In the last decades a plethora of synthetic CaP NPs have been developed leading to a huge variety of NPs differing in terms of composition (i.e., Ca/P ratio, anionic or cationic substituents), hydration level, crystal phase, crystallinity degree, dimension, morphology, aspect ratio, polydispersity index, aggregation degree, surface area, surface charge (total charge and charges present in surface), and colloidal stability [76-78]. Overall, CaP NPs are versatile materials because all the cited parameters can be tuned for different specific requirements.

CaP NPs do not intrinsically possess imaging or therapeutic features, but the high density of surface charges of CaP NPs, both positive (Ca^{2+}) and negative (PO_4^{3-} or OH^-), allows an efficient and stable adsorption of organic molecules as imaging probes, drugs, targeting molecules (i.e. ligands for cell surface receptor, antibodies, aptamers, etc.), and other kinds of biomolecules (i.e. nucleic acids, peptides, drugs, etc.) [79, 80]. In addition, CaP NPs allow also to incorporate some bioactive molecules within their structure as opposed to surface decoration or adsorption, thus protecting the therapeutic agent from the biological environment [65, 69]. CaP NPs can also be functionalized with organic molecules through covalent bonding e.g. using the reaction of surface hydroxyl groups with substituted alkoxysilanes [81]. Moreover, thanks to their highly flexible structure CaP NPs are able to accommodate several substituting ions (i.e. the same process occurring in biological CaPs), maintaining their crystal structure and physicochemical properties. Doping with luminescent ions, radionuclides, or MRI contrast agents can impart peculiar functionalities such as luminescence, magnetism, or hyperthermia [82, 83]. In the context of nanomedical application the most interesting characteristic of CaP NPs is their pH-dependent solubility. CaP NPs are stable in physiological conditions and in blood plasma (pH 7.4), but get degraded in biological acidic environments as found in endosomes and lysosomes after cellular intake [84] or in the acidic extracellular fluid of tumor tissues caused by the accumulation of lactic and carbonic acid produced by glycolysis, glutaminolysis, and ATP hydrolysis of tumor cells [85]. The consequences of CaP NPs pH-dependent solubility are that (i) the nanoparticles are biodegradable when are internalized in cells and (ii) in case of tumor environment the CaP NPs have an intrinsic pathology-triggered dissolution, which can be harnessed for chemotherapeutic drug release. Another interesting feature of CaP NPs is to facilitate internalization of molecules by modulating cell membrane properties, allowing internalization also in cells that do not have endocytic capability, like red blood cells [86, 87]. In addition, biomimetic CaP NPs have the advantage to be a low-cost nanomaterial, with cheap precursors and synthetic procedures that are simple to be scaled up and respect the principles of green chemistry [54].

1.4.2 Hard tissue regeneration

Historically CaPs were investigated as materials for hard tissues substitution and regeneration [55, 64]. In modern medicine CaP-based biomaterials are used in a wide number of different applications throughout the body, covering all areas of the skeleton [88]. Applications include dental implants, percutaneous devices, periodontal treatment, bone defects treatment, fracture treatment, total joint replacement, orthopedics, cranio-maxillofacial reconstruction, otolaryngology, and spinal surgery [55, 64]. Depending upon the desired characteristics of the material (resorbability, bioactivity, etc.) different CaP-based materials can be prepared and used. In general, for hard tissue applications CaPs are primarily processed as three-dimensional dense or porous monolithic ceramics, porous composites with synthetic or natural polymers, injectable cements, and coatings of metallic implants [89].

However, nowadays there is interest to use CaPs also as single nanoparticles for some application in hard tissue regeneration. This is especially true in dental field, where CaP NPs have been proposed for dental remineralization [90-94]. These NPs can be added to restorative materials or can be directly applied on the tooth surface [90]. It has been demonstrated that CaP NPs are more efficient for remineralization therapies in comparison to their macro-sized counterparts due to higher surface area and reactivity as well as better ability to adhere and penetrate into the dental lesions [95, 96]. In addition, CaP NPs can be functionalized to possess additional features, like to exert an antibacterial effect. In detail, CaP NPs were proposed for enamel remineralization, that means to restore dental enamel nanocrystal structure, coherence and mechanical properties, and for dentinal hypersensitivity treatment, that involves the permanent occlusion of exposed dentinal tubules. Furthermore, CaP NPs were also proposed as nano-fillers for dental resins with the purpose to improve adhesion, biocompatibility, and induce remineralization [97].

1.4.3 Description of the most relevant calcium phosphate phases

Hydroxyapatite (HA, $Ca_{10}(PO_4)_6(OH)_2$)

Hydroxyapatite is the most important CaP phase for biomedical application. Human hard tissues are mineralized by HA nanocrystals, and all the medical applications aimed to treat bone and teeth dysfunctions rely to use or induce the formation of this mineral. In addition, biomimetic HA nanocrystals – that is to say synthetic HA nanocrystals prepared to mimic biogenic HA chemistry and morphology – are well accepted by the organism since are recognized as a sort of endogenous material.

HA chemical formula is $Ca_5(PO_4)_3OH$, with a Ca/P molar ratio of 1.67. HA brute formula is often written as $Ca_{10}(PO_4)_6(OH)_2$ to indicate that the crystal unit cell comprises two entities, and this convention will be the used in this Ph. D. thesis. HA crystal structure is hexagonal with space group $P6_3/m$ with approximate unit cell parameters a = 9.37 Å and c = 6.88 Å. In HA unit cell the calcium ions are present into two different symmetry sites, called Ca(I) and Ca(II). The Ca(I) ions are identified in columns along the three-fold axes and each is nine-coordinated with O atoms. The Ca(II) ions are seven-coordinated, with six O atoms and one OH^- ion [98, 99]. Ca(II) ions form an equilateral triangular arrangement that extends along the c unit cell parameter, with OH^- ions placed between two Ca(II) triangles. This arrangement is called "OH channel" and is though that several ion substitutions – especially of hydroxyl ions – occurs through this channel [100]. A peculiarity of HA is its highly flexible structure and its capacity to tolerate high lattice distortion accommodating substituting ions very different from Ca and P while still maintaining its intrinsic structure. In particular, Ca^{2+} ions can be substituted by mono, di-, tri- and tetravalent cations (e.g. Ag^+, Na^+, Fe^{2+}, Zn^{2+}, Fe^{3+}, and Ti^{4+}), PO_4^{3-} can be replaced by di-, tri- and tetravalent anions (e.g. CO_3^{2-}, HPO_4^{2-}, AsO_4^{3-}, VO_4^{3-}, and SiO_4^{4-}) while OH^- can be replaced by mono- and divalent anions (e.g. F^-, Cl^-, and CO_3^{2-}) [82, 83]. Doping of synthetic HA is commonly used to introduce additional functionalities such as luminescence (lanthanides ions), magnetism and hyperthermia (iron ions), or to stimulate biologic responses such as osteoinduction (strontium ions), angiogenesis (copper ions), antibacterial (silver, zinc ions). One of the most common substitutions is carbonate doping, where CO_3^{2-} ions substitute PO_4^{3-} (called B-type carbonate substitution) or OH^- (called A-type carbonate substitution).

As previously stated, HA nanocrystals are the mineral crystal phase of mammalian mineralized tissues. With the exception of dental enamel, biogenic HA is poorly crystalline, nonstoichiometric (Ca/P molar ratio less than 1.67), nanometric in size (length 20–50 nm, width 15–30 nm, and thickness 1.5–4 nm), calcium (and OH^-) deficient, and incorporates foreign ions in

its crystal lattice (i.e. Na^+, Mg^{2+}, K^+, F^-, CO_3^{2-}, etc.) [101]. In addition, biogenic HA is a "living mineral" since its composition, surface and crystallographic properties can change with maturation, age or pathologies.

HA has been extensively used in the biomedical field. The most studied application was as material for restoration of mineralized tissues, that means to say in orthopedics and dentistry. HA was employed as 3-dimensional scaffold for bone replacement, as coating of metallic implants, or as particles for enamel remineralization [55, 64]. In addition to those applications, HA nanoparticles were also studied for medical imaging and for drug or gene delivery [89, 102-105].

Amorphous calcium phosphate (ACP, $Ca_9(PO_4)_6 \cdot xH_2O$)

Amorphous calcium phosphate is a non-crystalline calcium phosphate mineral phase. Interestingly, even if ACP is an amorphous material it possesses both a short-range order and a medium-range order, a feature uncommon for glasses. Indeed ACP basic structural unit, as proposed by Betts and Posner, is a roughly spherical cluster of ions having an average diameter of 9.5 Å consistent with the chemical composition $Ca_9(PO_4)_6$ [106, 107]. Betts and Posner suggest that ACP particles are a random aggregate of Posner's clusters, with water molecules that "glue" clusters together and thus explaining the formula $Ca_9(PO_4)_6 \cdot xH_2O$ (Figure 1.3). Posner's cluster has a Ca/P molar ratio of 1.5, however several ACPs with different stoichiometry were reported and are believed to possess different local arrangement of atoms [108, 109]. For this reason some authors have proposed to define different ACP on the basis of their stoichiometry – e.g. ACP with a Ca/P molar ratio of 1.5 has been defined as ATCP (amorphous tricalcium phosphate) [108, 109]. Interestingly, calcium and phosphate ion disposition in the Posner's cluster closely resembles part of atom arrangement in HA or OCP unit cell [110]. This structural similarity might be the reason why ACP tends to crystallize forming HA or OCP. In general ACP is an unstable material that rapidly transforms into the more thermodynamically stable CaP phases in solution or in dry state by reacting with atmospheric water [111] and for this reason the research on this material is not as deep as for other CaP phases. ACP is a biogenic calcium phosphate, and it is believed to be the precursor (transient) phase of biogenic HA of bones and teeth [91, 96, 112, 113]. Indeed, it was demonstrated by Robinson *et al.* that the formation of enamel occurs through the deposition of spherical ACP nanoparticles into chains, being subsequently transformed into HA [114].

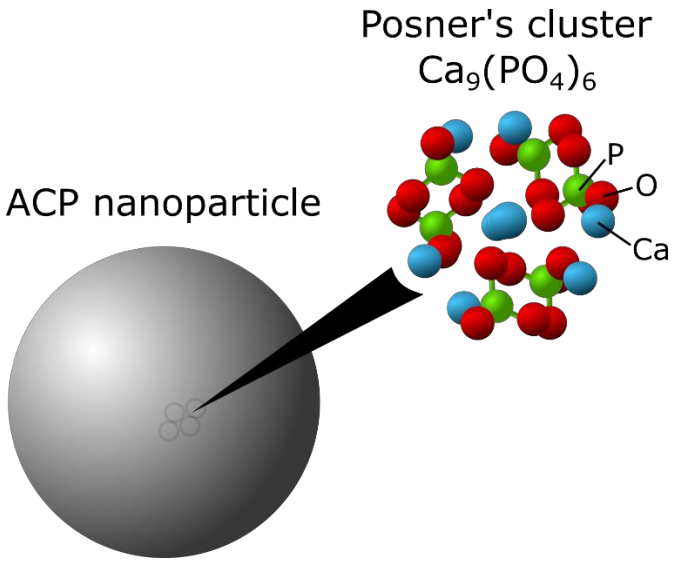

Figure 1.3. Schematic representation of Posner's cluster in ACP.

As stated before, ACP is not extensively used for biomedical application as well as other CaP phases due its intrinsic metastability that hinders material storage. Furthermore, ACP cannot be consolidated by conventional sintering without triggering crystallization and thus 3-dimensional structures made from ACP are not amorphous and have poor mechanical properties. However, recently it was reported the first sintered amorphous bioceramic material, that was achieved by the use of innovative sintering technologies such as Spark Plasma Sintering combined with ACP with tailored composition [115]. ACP has excellent bioactivity, high cell adhesion, tailorable biodegradation and good osteoconductivity and it is currently employed to manufacture several biomaterials for bone repair [108, 116]. It is used, for example, in the preparation of coatings on metallic prostheses, self-setting injectable cements and hybrid composites [108, 113, 116]. ACP most successful application is in dental field, where it is used and marketed for enamel remineralization [117, 118] and as dentin desensitizer, where its action is to fill and occlude dentinal tubules [119, 120].

Fluorapatite (FHA, $Ca_{10}(PO_4)_6F_2$) and Fluorhydroxyapatite ($Ca_{10}(PO_4)_6(OH)_{2-x}F_x$)

Fluorapatite is a fluorine-substituted hydroxyapatite. Fluoride (F^-) ions are able to substitute hydroxyl (OH^-) ions completely (isomorphous substitution). For this reason fluorapatites (or, more correctly, fluorhydroxyapatites) are defined as a family of apatitic material with a general

stoichiometry of $Ca_{10}(PO_4)_6(OH)_{2-x}F_x$, where $0 < x < 2$. Fluorapatites have the same atomic arrangement as HA and produce an identical diffraction pattern. However, FHA's *a* unit cell parameter is shorter than HA *a* unit cell parameter and can be observed as a shift in FHA (310) diffraction peak position. This unit cell shortening is due to the shorter Ca-F equilibrium distance compared to the Ca-OH distance of HA [121-124]. In identical crystallization conditions FHA is usually more crystalline than HA, because it is more thermodynamically stable [109]. Even if FHA is not a biogenic material, the use of fluorine supplement in the diet is used to induce the formation of FHA in the outer layer of dental enamel [125]. This condition is sought because FHA, being more crystalline than HA, is more resistant to acidic degradation and thus is more caries-resistant [126, 127].

In biomedical literature FHA has been studied for (i) enamel protection and remineralization, due to its higher resistance to acids, (ii) for osteoporosis treatment, since fluoride stimulates HA crystallization, and (iii) as antibacterial biomaterial, considering that fluoride ions are believed to inhibit the metabolic and physiological pathways of several microorganisms [128-133]. In addition FHA is interesting as nanomaterial for imaging application because F is believed to improve the luminescence of the rare earth-doped HA [134, 135].

Octacalcium phosphate (OCP, $Ca_8H_2(PO_4)_6{\cdot}5H_2O$)

Octacalcium phosphate is one of the several calcium phosphates crystal phases, and it has a close relationship to HA. Even if OCP has not the same stoichiometry as HA – it has a Ca/P molar ratio of 1.33 instead of 1.67 – nor the same crystal structure, it has an interesting crystallographic resemblance. OCP unit cell can be subdivided in regions that have an atomic arrangement very close to HA – called apatitic layers – interposed between regions that contain HPO_4^{2-} ions and water molecules, called hydrate layers [136]. For this reason OCP diffraction pattern closely resembles HA diffraction pattern, with the exception for the presence of the high intensity (100) peak at very low diffraction angle. OCP is a common precursor of HA when prepared from wet precipitation process, since it is less thermodynamically stable and the OCP -> HA conversion is predicted by Ostwald's rules of phases [63]. For this reason OCP has been proposed to be a precursor of biogenic HA during early bone and teeth formation [137], but now it is believed that ACP is biogenic HA precursor.

In biomedical literature OCP has been proposed as bone substitute material as bulk granules or coating of metallic implants [138]. OCP has been proved to convert in HA when implanted in bone defects, and this transformation induces a osteoconductive effect [139].

1.5 Functional by design approach

Functional by design is a new bottom-up approach for nanomaterials preparation which is the basis of the research work reported in this Ph. D. thesis. In nanomedical science the most common approach is to choose the nanomaterial on the basis of the required features. With this standard approach the first step is the definition of the application and the evaluation of material requirements. Afterward, most suitable nanomaterial is chosen and tested, studying its behavior in the framework of the application. So physicochemical properties of the material like biocompatibility, cell and tissue penetration, colloidal stability, surface properties, degradability, drug loading, and traceability are evaluated in the context of required features, such as hemodynamic lifetime, barrier crossing, diseased cell marking, etc. If the nanomaterial does not satisfy the requisites it is discarded in favor of another nanomaterial or, more commonly, extra properties are added through functionalization, that means to say that chemical moieties are grafted on nanomaterial's surface. The result of this approach is that (i) the list of used nanomaterials is short and nanomaterials for very different applications share the same chemical nature, and (ii) the nanomaterials have to undergo a plethora of extra functionalization steps in order to possess all the required features. This approach leads to several shortcomings in the development of nanomaterials for medicine:

- It is a long and time-consuming process that has to be restarted from the very beginning every time the application and/or the nanomaterial changes.
- The final nanomaterial is an ultra-complex product that is highly expensive and very difficult to scale-up for an industrial application.
- Unforeseeable interactions between nanomaterial, functionalization and organism could arise leading to undesired side effects or hindering the desired effect.

The functional by design approach is thought to bypass these shortcomings. With this approach the nanomaterial is knowingly designed to fulfill a specific function. In detail, the first step remains the choice of the application and the definition of the requirements for the nanomaterial. Afterward the nanomaterial is synthesized, altering the reaction in order to change the physicochemical properties of the product and tailoring them to the requisites

established in the first step. If the final product does not match the requisites, the nanomaterial re-prepared changing the reaction and tailoring conditions. The tailoring is the most complex step of the functional by design approach and can be achieved using templates molecules to control the formation and the properties of the nanomaterial. Recent findings in scientific literature have shown that with these templates is possible to finely control nanoparticles formation and growth and thus the tailoring can be applied [140]. At the end of this process, the product has almost all the required features and no or minimal functionalization is required to produce the desired nanomaterial. The functional by design approach has several advantages:

- It develops an extended library of similar but not identical nanomaterials.
- It develops a library of tailoring parameters for each nanomaterial, to be used to adjust nanomaterial properties to satisfy the chosen criteria.
- If a new application is chosen the library of nanomaterials and tailoring methods can speed up the translation process to set up a new product.
- Only the synthesis process has to be scaled up for an industrial application, increasing the feasibility of a commercial development.
- Since no extra functionalization steps are performed, the interaction of a new nanomaterial with the organism can be foreseen from previous works.

CaPs materials are very well suited for the functional by design approach. Several CaP mineral phases exist and easily form nanoparticles with slightly different physicochemical properties, thus giving a base of nanoparticles library. In addition, several factors involved in CaP preparation can work as tuning parameter, e.g. Ca and P precursor nature and concentration, reaction temperature and time, doping ions, and additives. Furthermore, CaP NPs biogenic and pathological formation in the organisms has been extensively studied and several of the mechanisms that control CaP NPs mineralization can be harnessed to tailor the nanoparticles properties [60, 63, 141, 142]. For examples, organic molecules like citrate that have been proved to be involved in bone mineralization and can be used to control CaP NPs formation with the functional by design approach.

Therefore, in this Ph. D. Thesis is reported the research work aimed to develop CaP NPs for nanomedicine using the functional by design approach, employing the citrate molecule as template regulator.

1.6 Bibliography

1. Nanotechnologies, I., *Vocabulary–Part 1: Core Terms.* International Stanardisation Organisation (ISO), Technical Specification ISO/TS, 2015: p. 80004-1.
2. Arico, A.S., et al., *Nanostructured materials for advanced energy conversion and storage devices*, in *Materials for sustainable energy: a collection of peer-reviewed research and review articles from Nature Publishing Group*. 2011, World Scientific. p. 148-159.
3. Sattler, K.D., *Handbook of nanophysics: nanoelectronics and nanophotonics*. 2010: CRC Press.
4. Wang, P., et al., *Nanotechnology: a new opportunity in plant sciences.* Trends in plant science, 2016. **21**(8): p. 699-712.
5. Agarwal, A. and H. Joshi, *Application of nanotechnology in the remediation of contaminated groundwater: a short review.* Recent Research in Science and Technology, 2010. **2**(6).
6. Tantra, R., et al., *Nanomaterial syntheses.* Nanomaterial Characterization: Introduction, An, 2016: p. 25-48.
7. Moghimi, S.M., A.C. Hunter, and J.C. Murray, *Nanomedicine: current status and future prospects.* Faseb Journal, 2005. **19**(3): p. 311-330.
8. Moghimi, S.M., A.C. Hunter, and J.C. Murray, *Long-circulating and target-specific nanoparticles: Theory to practice.* Pharmacological Reviews, 2001. **53**(2): p. 283-318.
9. Barreto, J.A., et al., *Nanomaterials: applications in cancer imaging and therapy.* Advanced Materials, 2011. **23**(12): p. H18-H40.
10. Kreuter, J., *Nanoparticulate systems for brain delivery of drugs.* Advanced drug delivery reviews, 2001. **47**(1): p. 65-81.
11. Albanese, A., P.S. Tang, and W.C.W. Chan, *The Effect of Nanoparticle Size, Shape, and Surface Chemistry on Biological Systems*, in *Annual Review of Biomedical Engineering, Vol 14*, M.L. Yarmush, Editor. 2012, Annual Reviews: Palo Alto. p. 1-16.
12. Nel, A., et al., *Toxic potential of materials at the nanolevel.* Science, 2006. **311**(5761): p. 622-627.
13. Singh, N., et al., *Potential toxicity of superparamagnetic iron oxide nanoparticles (SPION).* Nano reviews, 2010. **1**(1): p. 5358.
14. Stroh, A., et al., *Iron oxide particles for molecular magnetic resonance imaging cause transient oxidative stress in rat macrophages.* Free Radical Biology and Medicine, 2004. **36**(8): p. 976-984.
15. Savi, M., et al., *Titanium dioxide nanoparticles promote arrhythmias via a direct interaction with rat cardiac tissue.* Particle and fibre toxicology, 2014. **11**(1): p. 63.
16. Shvedova, A.A., et al., *Unusual inflammatory and fibrogenic pulmonary responses to single-walled carbon nanotubes in mice.* American Journal of Physiology-Lung Cellular and Molecular Physiology, 2005. **289**(5): p. L698-L708.
17. Krug, H.F., *Nanosafety research—are we on the right track?* Angewandte Chemie International Edition, 2014. **53**(46): p. 12304-12319.
18. Doane, T.L. and C. Burda, *The unique role of nanoparticles in nanomedicine: imaging, drug delivery and therapy.* Chemical Society Reviews, 2012. **41**(7): p. 2885-2911.
19. Singal, P.K. and N. Iliskovic, *Doxorubicin-induced cardiomyopathy.* New England Journal of Medicine, 1998. **339**(13): p. 900-905.
20. Davis, M.E., Z. Chen, and D.M. Shin, *Nanoparticle therapeutics: an emerging treatment modality for cancer.* Nature Reviews Drug Discovery, 2008. **7**(9): p. 771-782.
21. Peer, D., et al., *Nanocarriers as an emerging platform for cancer therapy.* Nat Nano, 2007. **2**(12): p. 751-760.
22. Pietronave, S., et al., *Functionalized nanomaterials for diagnosis and therapy of cancer.* J Appl Biomater Biomech, 2009. **7**(2): p. 77-89.

23. Minelli, C., S.B. Lowe, and M.M. Stevens, *Engineering nanocomposite materials for cancer therapy.* Small, 2010. **6**(21): p. 2336-2357.
24. Davis, M.E., Z. Chen, and D.M. Shin, *Nanoparticle therapeutics: an emerging treatment modality for cancer*, in *Nanoscience And Technology: A Collection of Reviews from Nature Journals*. 2010, World Scientific. p. 239-250.
25. Tacar, O., P. Sriamornsak, and C.R. Dass, *Doxorubicin: an update on anticancer molecular action, toxicity and novel drug delivery systems.* Journal of pharmacy and pharmacology, 2013. **65**(2): p. 157-170.
26. Deepa, K., S. Singha, and T. Panda, *Doxorubicin nanoconjugates.* Journal of nanoscience and nanotechnology, 2014. **14**(1): p. 892-904.
27. Xue, X., et al., *Nanoscale drug delivery platforms overcome platinum-based resistance in cancer cells due to abnormal membrane protein trafficking.* ACS nano, 2013. **7**(12): p. 10452-10464.
28. Prasad, R. and V. Koul, *Transdermal delivery of methotrexate: past, present and future prospects.* Therapeutic delivery, 2012. **3**(3): p. 315-325.
29. Romaine, S.P., et al., *MicroRNAs in cardiovascular disease: an introduction for clinicians.* Heart, 2015. **101**(12): p. 921-928.
30. Mostaghaci, B., B. Loretz, and C.M. Lehr, *Calcium Phosphate System for Gene Delivery: Historical Background and Emerging Opportunities.* Current Pharmaceutical Design, 2016. **22**(11): p. 1529-1533.
31. Chapman, S., et al., *Nanoparticles for cancer imaging: The good, the bad, and the promise.* Nano today, 2013. **8**(5): p. 454-460.
32. Kelkar, S.S. and T.M. Reineke, *Theranostics: combining imaging and therapy.* Bioconjugate chemistry, 2011. **22**(10): p. 1879-1903.
33. Neuberger, T., et al., *Superparamagnetic nanoparticles for biomedical applications: possibilities and limitations of a new drug delivery system.* Journal of Magnetism and Magnetic materials, 2005. **293**(1): p. 483-496.
34. de Rosales, R.T., *Potential clinical applications of bimodal PET-MRI or SPECT-MRI agents.* Journal of Labelled Compounds and Radiopharmaceuticals, 2014. **57**(4): p. 298-303.
35. Pansare, V.J., et al., *Review of long-wavelength optical and NIR imaging materials: contrast agents, fluorophores, and multifunctional nano carriers.* Chemistry of Materials, 2012. **24**(5): p. 812-827.
36. Xie, J., et al., *PET/NIRF/MRI triple functional iron oxide nanoparticles.* Biomaterials, 2010. **31**(11): p. 3016-3022.
37. Del Vecchio, S., et al., *Nuclear imaging in cancer theranostics.* The Quarterly Journal of Nuclear Medicine and Molecular Imaging, 2007. **51**(2): p. 152.
38. Singh, R. and J.W. Lillard Jr, *Nanoparticle-based targeted drug delivery.* Experimental and molecular pathology, 2009. **86**(3): p. 215-223.
39. Maeda, H., H. Nakamura, and J. Fang, *The EPR effect for macromolecular drug delivery to solid tumors: Improvement of tumor uptake, lowering of systemic toxicity, and distinct tumor imaging in vivo.* Advanced drug delivery reviews, 2013. **65**(1): p. 71-79.
40. Danhier, F., O. Feron, and V. Préat, *To exploit the tumor microenvironment: Passive and active tumor targeting of nanocarriers for anti-cancer drug delivery.* Journal of Controlled Release, 2010. **148**(2): p. 135-146.
41. Nichols, J.W. and Y.H. Bae, *EPR: Evidence and fallacy.* Journal of Controlled Release, 2014. **190**: p. 451-464.
42. Steichen, S.D., M. Caldorera-Moore, and N.A. Peppas, *A review of current nanoparticle and targeting moieties for the delivery of cancer therapeutics.* European journal of pharmaceutical sciences, 2013. **48**(3): p. 416-427.

43. Torchilin, V.P., *Passive and Active Drug Targeting: Drug Delivery to Tumors as an Example*, in *Drug Delivery*, M. Schäfer-Korting, Editor. 2010, Springer Berlin Heidelberg: Berlin, Heidelberg. p. 3-53.
44. Toporkiewicz, M., et al., *Toward a magic or imaginary bullet? Ligands for drug targeting to cancer cells: principles, hopes, and challenges.* International Journal of Nanomedicine, 2015. **10**: p. 1399-1414.
45. Wang, M. and M. Thanou, *Targeting nanoparticles to cancer.* Pharmacological Research, 2010. **62**(2): p. 90-99.
46. Shaughnessy, A.F., *Monoclonal antibodies: magic bullets with a hefty price tag.* Bmj, 2012. **345**: p. e8346.
47. Holliger, P. and P.J. Hudson, *Engineered antibody fragments and the rise of single domains.* Nature biotechnology, 2005. **23**(9): p. 1126.
48. Laakkonen, P. and K. Vuorinen, *Homing peptides as targeted delivery vehicles.* Integrative Biology, 2010. **2**(7-8): p. 326-337.
49. Dua, P., S. Kim, and D.-k. Lee, *Nucleic acid aptamers targeting cell-surface proteins.* Methods, 2011. **54**(2): p. 215-225.
50. Daniels, T.R., et al., *The transferrin receptor and the targeted delivery of therapeutic agents against cancer.* Biochimica et Biophysica Acta (BBA)-General Subjects, 2012. **1820**(3): p. 291-317.
51. Irache, J.M., et al., *Mannose-targeted systems for the delivery of therapeutics.* Expert opinion on drug delivery, 2008. **5**(6): p. 703-724.
52. Chen, C., et al., *Structural basis for molecular recognition of folic acid by folate receptors.* Nature, 2013. **500**(7463): p. 486.
53. Mann, S., *Biomineralization: principles and concepts in bioinorganic materials chemistry*. Vol. 5. 2001: Oxford University Press on Demand.
54. Gómez-Morales, J., et al., *Progress on the preparation of nanocrystalline apatites and surface characterization: overview of fundamental and applied aspects.* Progress in Crystal Growth and Characterization of Materials, 2013. **59**(1): p. 1-46.
55. Dorozhkin, S.V. and M. Epple, *Biological and Medical Significance of Calcium Phosphates.* Angewandte Chemie International Edition, 2002. **41**(17): p. 3130-3146.
56. Boskey, A.L. and P.G. Robey, *The regulatory role of matrix proteins in mineralization of bone*, in *Osteoporosis*. 2013, Elsevier. p. 235-255.
57. Boskey, A.L., *Mineralization of bones and teeth.* Elements, 2007. **3**(6): p. 385-391.
58. Hu, Y.-Y., A. Rawal, and K. Schmidt-Rohr, *Strongly bound citrate stabilizes the apatite nanocrystals in bone.* Proceedings of the National Academy of Sciences, 2010.
59. Xie, B. and G.H. Nancollas, *How to control the size and morphology of apatite nanocrystals in bone.* Proceedings of the National Academy of Sciences, 2010. **107**(52): p. 22369-22370.
60. Delgado-López, J.M., et al., *Crystallization of bioinspired citrate-functionalized nanoapatite with tailored carbonate content.* Acta biomaterialia, 2012. **8**(9): p. 3491-3499.
61. Chatzipanagis, K., et al., *Crystallization of citrate-stabilized amorphous calcium phosphate to nanocrystalline apatite: a surface-mediated transformation.* CrystEngComm, 2016. **18**(18): p. 3170-3173.
62. Delgado-López, J.M., et al., *Crystal Size, Morphology, and Growth Mechanism in Bio-Inspired Apatite Nanocrystals.* Advanced Functional Materials, 2014. **24**(8): p. 1090-1099.
63. Iafisco, M., et al., *The growth mechanism of apatite nanocrystals assisted by citrate: relevance to bone biomineralization.* CrystEngComm, 2015. **17**(3): p. 507-511.
64. Dorozhkin, S.V., *Bioceramics of calcium orthophosphates.* Biomaterials, 2010. **31**(7): p. 1465-85.

65. Miragoli, M., et al., *Inhalation of peptide-loaded nanoparticles improves heart failure.* Science translational medicine, 2018. **10**(424): p. eaan6205.
66. Victor, S.P. and T.S.S. Kumar, *Tailoring calcium-deficient hydroxyapatite nanocarriers for enhanced release of antibiotics.* Journal of biomedical nanotechnology, 2008. **4**(2): p. 203-209.
67. Victor, S.P., et al., *Supramolecular hydroxyapatite complexes as theranostic near-infrared luminescent drug carriers.* CrystEngComm, 2014. **16**(38): p. 9033-9042.
68. Iafisco, M., et al., *Superparamagnetic iron-doped nanocrystalline apatite as a delivery system for doxorubicin.* Journal of Materials Chemistry B, 2016. **4**(1): p. 57-70.
69. Di Mauro, V., et al., *Bioinspired negatively charged calcium phosphate nanocarriers for cardiac delivery of MicroRNAs.* Nanomedicine, 2016. **11**(8): p. 891-906.
70. Zhou, L., et al., *DNA-mediated biomineralization of rare-earth nanoparticles for simultaneous imaging and stimuli-responsive drug delivery.* Biomaterials, 2014. **35**(30): p. 8694-8702.
71. He, Q., et al., *Calcium phosphate nanoparticles induce mucosal immunity and protection against herpes simplex virus type 2.* Clin. Diagn. Lab. Immunol., 2002. **9**(5): p. 1021-1024.
72. Epple, M., *Review of potential health risks associated with nanoscopic calcium phosphate.* Acta biomaterialia, 2018. **77**: p. 1-14.
73. Blanco, E., H. Shen, and M. Ferrari, *Principles of nanoparticle design for overcoming biological barriers to drug delivery.* Nature biotechnology, 2015. **33**(9): p. 941.
74. Faraji, A.H. and P. Wipf, *Nanoparticles in cellular drug delivery.* Bioorganic & medicinal chemistry, 2009. **17**(8): p. 2950-2962.
75. Roveri, N., B. Palazzo, and M. Iafisco, *The role of biomimetism in developing nanostructured inorganic matrices for drug delivery.* Expert Opin Drug Deliv, 2008. **5**(8): p. 861-77.
76. Sadat-Shojai, M., et al., *Synthesis methods for nanosized hydroxyapatite with diverse structures.* Acta biomaterialia, 2013. **9**(8): p. 7591-7621.
77. Lin, K., C. Wu, and J. Chang, *Advances in synthesis of calcium phosphate crystals with controlled size and shape.* Acta biomaterialia, 2014. **10**(10): p. 4071-4102.
78. Lee, H.J., et al., *Modification of Hydroxyapatite Nanosurfaces for Enhanced Colloidal Stability and Improved Interfacial Adhesion in Nanocomposites.* Chemistry of Materials, 2006. **18**(21): p. 5111-5118.
79. Iafisco, M., et al., *Cell surface receptor targeted biomimetic apatite nanocrystals for cancer therapy.* Small, 2013. **9**(22): p. 3834-3844.
80. Iafisco, M., et al., *Conjugation of hydroxyapatite nanocrystals with human immunoglobulin G for nanomedical applications.* Colloids and Surfaces B: Biointerfaces, 2012. **90**(0): p. 1-7.
81. Tseng, Y.-C., et al., *Lipid–calcium phosphate nanoparticles for delivery to the lymphatic system and SPECT/CT imaging of lymph node metastases.* Biomaterials, 2014. **35**(16): p. 4688-4698.
82. Šupová, M., *Substituted hydroxyapatites for biomedical applications: a review.* Ceramics International, 2015. **41**(8): p. 9203-9231.
83. Boanini, E., M. Gazzano, and A. Bigi, *Ionic substitutions in calcium phosphates synthesized at low temperature.* Acta biomaterialia, 2010. **6**(6): p. 1882-1894.
84. Rodríguez-Ruiz, I., et al., *pH-Responsive Delivery of Doxorubicin from Citrate–Apatite Nanocrystals with Tailored Carbonate Content.* Langmuir, 2013. **29**(26): p. 8213-8221.
85. Stubbs, M., et al., *Causes and consequences of tumour acidity and implications for treatment.* Molecular medicine today, 2000. **6**(1): p. 15-19.
86. Stefanic, M., et al., *Apatite nanoparticles strongly improve red blood cell cryopreservation by mediating trehalose delivery via enhanced membrane permeation.* Biomaterials, 2017. **140**: p. 138-149.

87. Choimet, M., et al., *Nanomedicine: interaction of biomimetic apatite colloidal nanoparticles with human blood components.* Colloids and Surfaces B: Biointerfaces, 2016. **145**: p. 87-94.
88. Vallet-Regí, M. and E. Ruiz-Hernández, *Bioceramics: From Bone Regeneration to Cancer Nanomedicine.* Advanced Materials, 2011. **23**(44): p. 5177-5218.
89. Navarro, M., et al., *Biomaterials in orthopaedics.* Journal of the Royal Society Interface, 2008. **5**(27): p. 1137-1158.
90. Zhang, X., X. Deng, and Y. Wu, *Remineralizing Nanomaterials for Minimally Invasive Dentistry*, in *Nanotechnology in Endodontics: Current and Potential Clinical Applications*, A. Kishen, Editor. 2015, Springer International Publishing: Cham. p. 173-193.
91. Zhao, J., et al., *Amorphous calcium phosphate and its application in dentistry.* Chemistry Central Journal, 2011. **5**(1): p. 1-7.
92. Enax, J. and M. Epple, *Synthetic hydroxyapatite as a biomimetic oral care agent.* Oral Health and Preventive Dentistry, 2018. **16**(1): p. 7-19.
93. Roveri, N., et al., *Surface Enamel Remineralization: Biomimetic Apatite Nanocrystals and Fluoride Ions Different Effects.* Journal of Nanomaterials, 2009.
94. Ruan, Q. and J. Moradian-Oldak, *Amelogenin and enamel biomimetics.* Journal of Materials Chemistry B, 2015. **3**(16): p. 3112-3129.
95. Li, L., et al., *Repair of enamel by using hydroxyapatite nanoparticles as the building blocks.* Journal of Materials Chemistry, 2008. **18**(34): p. 4079-4084.
96. Melo, M.A.S., et al., *Nanotechnology-based restorative materials for dental caries management.* TRENDS in Biotechnology, 2013. **31**(8): p. 459-467.
97. Braga, R.R., *Calcium phosphates as ion-releasing fillers in restorative resin-based materials.* Dental Materials, 2019. **35**(1): p. 3-14.
98. Elliott, J., R. Wilson, and S. Dowker, *Apatite structures.* Advances in X-ray Analysis, 2002. **45**: p. 172-181.
99. Mehmel, M., *21 Über die Struktur des Apatits. I.* Zeitschrift für Kristallographie-Crystalline Materials, 1930. **75**(1): p. 323-331.
100. Uskoković, V., *The role of hydroxyl channel in defining selected physicochemical peculiarities exhibited by hydroxyapatite.* RSC Advances, 2015. **5**(46): p. 36614-36633.
101. Iafisco, M. and J.M. Delgado-López, *Apatite: Synthesis, Structural Characterization, and Biomedical Applications*. 2014: Nova Science Publishers, Incorporated.
102. Al-Kattan, A., et al., *Biomimetic nanocrystalline apatites: Emerging perspectives in cancer diagnosis and treatment.* International Journal of Pharmaceutics, 2012. **423**(1): p. 26-36.
103. Degli Esposti, L., et al., *Calcium phosphate-based nanosystems for advanced targeted nanomedicine.* Drug development and industrial pharmacy, 2018: p. 1-16.
104. Degli Esposti, L., A. Tampieri, and M. Iafisco, *Nanostructured calcium phosphates in theranostic nanomedicine*, in *Nanotechnologies in Preventive and Regenerative Medicine*, V. Uskoković, Editor. 2017, Elsevier.
105. Epple, M., et al., *Application of calcium phosphate nanoparticles in biomedicine.* Journal of Materials Chemistry, 2010. **20**(1): p. 18-23.
106. Betts, F. and A.S. Posner, *An X-ray radial distribution study of amorphous calcium phosphate.* Materials Research Bulletin, 1974. **9**(3): p. 353-360.
107. Posner, A.S., F. Betts, and N.C. Blumenthal, *Formation and structure of synthetic and bone hydroxyapatites.* Progress in Crystal Growth and Characterization, 1980. **3**(1): p. 49-64.
108. Combes, C. and C. Rey, *Amorphous calcium phosphates: Synthesis, properties and uses in biomaterials.* Acta biomaterialia, 2010. **6**(9): p. 3362-3378.
109. Dorozhkin, S.V., *Calcium orthophosphates (CaPO4): occurrence and properties.* Progress in Biomaterials, 2016. **5**(1): p. 9-70.

110. Posner, A.S. and F. Betts, *Synthetic amorphous calcium phosphate and its relation to bone mineral structure.* Accounts of Chemical Research, 1975. **8**(8): p. 273-281.
111. Boskey, A.L. and A.S. Posner, *Conversion of amorphous calcium phosphate to microcrystalline hydroxyapatite. A pH-dependent, solution-mediated, solid-solid conversion.* The Journal of Physical Chemistry, 1973. **77**(19): p. 2313-2317.
112. Hannig, M. and C. Hannig, *Nanomaterials in preventive dentistry.* Nat Nano, 2010. **5**(8): p. 565-569.
113. Zhao, J., et al., *First detection, characterization, and application of amorphous calcium phosphate in dentistry.* Journal of Dental Sciences, 2012. **7**(4): p. 316-323.
114. Robinson, C., et al., *Subunit Structures in Hydroxyapatite Crystal Development in Enamel: Implications for Amelogenesis Imperfecta.* Connective Tissue Research, 2003. **44**(1): p. 65-71.
115. Luginina, M., et al., *First successful stabilization of consolidated amorphous calcium phosphate (ACP) by cold sintering: toward highly-resorbable reactive bioceramics.* Journal of Materials Chemistry B, 2020.
116. Dorozhkin, S.V., *Amorphous calcium (ortho)phosphates.* Acta biomaterialia, 2010. **6**(12): p. 4457-4475.
117. Cochrane, N.J., et al., *New Approaches to Enhanced Remineralization of Tooth Enamel.* Journal of Dental Research, 2010. **89**(11): p. 1187-1197.
118. Li, J., et al., *Long-term remineralizing effect of casein phosphopeptide-amorphous calcium phosphate (CPP-ACP) on early caries lesions in vivo: A systematic review.* Journal of Dentistry, 2014. **42**(7): p. 769-777.
119. Rahiotis, C. and G. Vougiouklakis, *Effect of a CPP-ACP agent on the demineralization and remineralization of dentine in vitro.* Journal of Dentistry, 2007. **35**(8): p. 695-698.
120. Poggio, C., et al., *Analysis of dentin/enamel remineralization by a CPP-ACP paste: AFM and SEM study.* Scanning, 2013. **35**(6): p. 366-374.
121. Jha, L., et al., *Preparation and characterization of fluoride-substituted apatites.* Journal of Materials Science: Materials in Medicine, 1997. **8**(4): p. 185-191.
122. Chen, Y. and X. Miao, *Thermal and chemical stability of fluorohydroxyapatite ceramics with different fluorine contents.* Biomaterials, 2005. **26**(11): p. 1205-1210.
123. Rodrıguez-Lorenzo, L., J. Hart, and K. Gross, *Influence of fluorine in the synthesis of apatites. Synthesis of solid solutions of hydroxy-fluorapatite.* Biomaterials, 2003. **24**(21): p. 3777-3785.
124. Young, R. and J. Elliott, *Atomic-scale bases for several properties of apatites.* Archives of Oral Biology, 1966. **11**(7): p. 699-707.
125. Aoba, T., *The effect of fluoride on apatite structure and growth.* Critical Reviews in Oral Biology & Medicine, 1997. **8**(2): p. 136-153.
126. Lynch, R., R. Navada, and R. Walia, *Low-levels of fluoride in plaque and saliva and their effects on the demineralisation and remineralisation of enamel; role of fluoride toothpastes.* International dental journal, 2004. **54**(S5): p. 304-309.
127. ten Cate, J.M., *Contemporary perspective on the use of fluoride products in caries prevention.* Br Dent J, 2013. **214**(4): p. 161-167.
128. Harrison, J., et al., *Sintered hydroxyfluorapatites—IV: the effect of fluoride substitutions upon colonisation of hydroxyapatites by mouse embryonic stem cells.* Biomaterials, 2004. **25**(20): p. 4977-4986.
129. Bertoni, E., et al., *Nanocrystals of magnesium and fluoride substituted hydroxyapatite.* Journal of Inorganic Biochemistry, 1998. **72**(1-2): p. 29-35.
130. Qu, H. and M. Wei, *The effect of fluoride contents in fluoridated hydroxyapatite on osteoblast behavior.* Acta biomaterialia, 2006. **2**(1): p. 113-119.

131. Wiegand, A., W. Buchalla, and T. Attin, *Review on fluoride-releasing restorative materials—fluoride release and uptake characteristics, antibacterial activity and influence on caries formation.* Dental Materials, 2007. **23**(3): p. 343-362.
132. Ten Cate, J. and J. Featherstone, *Mechanistic aspects of the interactions between fluoride and dental enamel.* Critical Reviews in Oral Biology & Medicine, 1991. **2**(3): p. 283-296.
133. Marquis, R.E., *Antimicrobial actions of fluoride for oral bacteria.* Canadian journal of microbiology, 1995. **41**(11): p. 955-964.
134. Hui, J. and X. Wang, *Luminescent, Colloidal, F-Substituted, Hydroxyapatite Nanocrystals.* Chemistry–A European Journal, 2011. **17**(25): p. 6926-6930.
135. Sun, R., et al., *Controlled synthesis and enhanced luminescence of europium-doped fluorine-substituted hydroxyapatite nanoparticles.* CrystEngComm, 2013. **15**(17): p. 3442-3447.
136. Brown, W.E., L.W. Schroeder, and J.S. Ferris, *Interlayering of crystalline octacalcium phosphate and hydroxylapatite.* Journal of Physical Chemistry, 1979. **83**(11): p. 1385-1388.
137. Brown, W.E., *Crystal growth of bone mineral.* Clinical Orthopaedics and Related Research®, 1966. **44**: p. 205-220.
138. Suzuki, O., *Octacalcium phosphate: osteoconductivity and crystal chemistry.* Acta Biomaterialia, 2010. **6**(9): p. 3379-3387.
139. Suzuki, O., et al., *Bone formation enhanced by implanted octacalcium phosphate involving conversion into Ca-deficient hydroxyapatite.* Biomaterials, 2006. **27**(13): p. 2671-2681.
140. Grzelczak, M., et al., *Directed self-assembly of nanoparticles.* ACS nano, 2010. **4**(7): p. 3591-3605.
141. Gómez-Morales, J., et al., *Amino acidic control of calcium phosphate precipitation by using the vapor diffusion method in microdroplets.* Crystal Growth & Design, 2011. **11**(11): p. 4802-4809.
142. Wang, A., et al., *Size-controlled synthesis of hydroxyapatite nanorods in the presence of organic modifiers.* Materials Letters, 2007. **61**(10): p. 2084-2088.

Chapter 2. Materials and experimental methods

2.1 Materials

In this Ph.D. research, the following reagents were used:

Acetic acid (CH_3COOH; ≥99.7% pure), calcium chloride dihydrate ($CaCl_2 \cdot 2H_2O$, ≥99.0% pure), Dulbecco's phosphate buffered saline solution (modified without $CaCl_2$ and $MgCl_2$), fetal bovine serum (FBS research grade), 4-(2-hydroxyethyl)-1-piperazineethanesulfonic acid (HEPES) ($C_8H_{18}N_2O_4S$, ≥99.0% pure), hydrochloric acid (HCl, 37% pure), lactic acid ($C_3H_6O_3$ ≥90.0% pure), magnesium chloride dihydrate ($MgCl_2 \cdot 2H_2O$, ≥99.0% pure), nitric acid (HNO_3; 65% pure), orthophosphoric acid (H_3PO_4 85wt. % in H_2O), glutaric acid ($C_5H_8O_4$ ≥99.0% pure (named thereafter Glr)), potassium chloride (KCl ≥99.5% pure), potassium hydroxycitrate tribasic monohydrate ($K_3(C_6H_5O_8) \cdot H_2O$, ≥95.0% pure (named thereafter K_3(CitOH)), potassium thiocyanate (KSCN ≥98.0% pure), sodium carbonate monohydrate ($Na_2CO_3 \cdot 2H_2O$, ≥99.0% pure), sodium carbonate monobasic ($NaHCO_3$, ≥99.7% pure), sodium citrate tribasic dihydrate ($Na_3(C_6H_5O_7) \cdot 2H_2O$, ≥99.0% pure (named thereafter Na_3(Cit)), sodium hydroxide (NaOH, ≥98.0% pure), sodium fluoride (NaF, ≥99.0% pure), sodium phosphate dibasic dihydrate ($Na_2HPO_4 \cdot 2H_2O$, ≥99.0% pure), strontium chloride dihydrate ($SrCl_2 \cdot 2H_2O$, ≥99.0% pure), were purchased from Sigma Aldrich (St. Luis, MO, USA) and used without further purification.

Sulfo-cyanine 7 amine fluorophore ($C_{43}H_{58}N_4O_7S_2$, 95% pure, hereafter named Cy7) was purchased from Lumiprobe GmbH (Hannover, Germany) and used without further purification.

Custom peptides were purchased from GeneScript and used without further purification. Peptides are: scramble hemagglutinin peptide (peptide HA, YPYDVPDYA), therapeutic mimetic peptide (peptide MP, DQRPDREAPRS) and arginin modified cell internalizing therapeutic mimetic peptide (peptide R7W-MP, RRRRRRRDQRPDREAPRS).

Commercial fluorhydroxyapatite (FHA) was purchased from Kalichem S.r.l. (Rezzato, BS, Italy).

All the solutions were prepared with ultrapure water (18.2 MΩ × cm, 25 °C, arium© pro, Sartorius).

2.2 Analytical methods

Several analytical techniques reported in this Ph.D. research are the same of a thesis previously published [1]. Sample preparation and data acquisition will be reported in this Chapter.

2.2.1 X-ray diffraction

Powder X-ray diffraction

Powder X-ray Diffraction (PXRD) was used as a non-destructive analytical technique for phase identification of crystalline or amorphous materials. The PXRD patterns of the samples were recorded on a D8 Advance diffractometer (Bruker, Karlsruhe, Germany) equipped with a Lynx-eye position sensitive detector using Cu Kα radiation (λ = 1.54178 Å) generated at 40 kV and 40 mA as X-ray source. Spectra were recorded in the 2θ range from 10 to 60° with a step size (2θ) of 0.02 and a counting time of 0.5 s.

Rietveld refinement

Rietveld refinement was used to determine crystal domains dimension, unit cell parameters and phase composition of polycrystalline samples. For Rietveld refinement experiments the PXRD patterns of the samples were recorded on a D8 Advance diffractometer (Bruker, Karlsruhe, Germany) equipped with a Lynx-eye position sensitive detector using Cu Kα radiation (λ = 1.54178 Å) generated at 40 kV and 40 mA. Spectra were recorded in the 2θ range from 10 to 80° with a step size (2θ) of 0.02 and a counting time of 1s. Unit cell indexing was performed with the software TOPAS5 [2].

Unit cell axes were obtained by Rietveld refinement considering a single-phase system, using tabulated atomic coordinates [3, 4]. Symmetrized spherical harmonics were used to cope, phenomenologically, with anisotropic peak broadening effects due to the anisotropic crystal shape. The PXRD patterns background was calculated as 11-th order Chebychev function.

The average size of crystal domains along the apatite axis directions ($D_{[002]}$) and ($D_{[310]}$) were calculated as full-profile peak broadening evaluation with the software TOPAS5, using fundamental parameters peak function. The PXRD patterns background was calculated as 11-th order Chebychev function. Instrumental peak broadening was evaluated by collecting a standard LaB_6 sample before the analysis.

2.2.2 Thermogravimetric analysis

Thermogravimetric analysis (TGA) was used to quantify volatile components of the samples such as water, organic molecules, and carbonate ions. The TGA analyses were performed using a STA 449C Jupiter (Netzsch GmbH, Selb, Germany) apparatus. About 10 mg of sample was weighted in an alumina crucible and heated from room temperature to 1200 °C under air flow with a heating rate of 10 °C/min.

2.2.3 Electron microscopy

Scanning electron microscopy

Scanning electron microscopy (SEM) was used to assess the micro-morphology of the samples using secondary electrons imaging. In addition, energy dispersive spectroscopy (EDS) integrated in SEM was used to perform semiquantitative elemental analysis. SEM micrographs and EDS spectra were collected with a field-emission microscope (FESEM, mod. ΣIGMA, ZEISS NTS Gmbh, Oberkochen, Germany) coupled to an energy-dispersive X-ray microanalyzer (mod. INCA Energy 300, Oxford Instruments, Abingdon-on-Thames, UK). Operating voltage was set at 10 keV. EDS spectra were collected in spot modality in at least four different regions of the sample. Samples were fixed on aluminum stubs using a carbon tape or a carbon glue.

Transmission electron microscopy

Transmission electron microscopy (TEM) was use to study the morphology of nanoparticulate samples with bright field imaging. In addition, selected area electron diffraction (SAED) modality was used to study the crystallinity of single nanoparticles. TEM micrographs and SAED patterns of the samples were collected with a Tecnai F20 microscope (Fei Corp., Hillsboro, OR, USA) equipped with a Schottky emitter operating at 120 keV. The dry powder samples were ultrasonically dispersed in ultrapure water and then a few droplets of the slurry were deposited on 200 mesh copper TEM grids covered with thin amorphous carbon films and incubated for several minutes. After that, the excess of water was manually blotted and dried.

2.2.4 Vibrational spectroscopy

Fourier transform infra-red spectroscopy

Fourier transform infra-red (FT-IR) spectrometry was used to characterize the vibrational structure of the samples, to assess the presence of functional groups, and to study variations in local order. For spectroscopic characterization the FT-IR analyses were carried out on a Nicolet iS5 spectrometer (Thermo Fisher Scientific Inc., Waltham, MA, USA) with a resolution of 2 cm^{-1} by accumulation of 32 scans covering the 4000 to 400 cm^{-1} range, using a diamond ATR accessory model iD7.

For vibrational peak deconvolution the FT-IR analyses were carried out with a resolution of 2 cm^{-1} by accumulation of 64 scans covering the 4000 to 400 cm^{-1} spectral range with the same instrument in transmission mode using the KBr pellet method. In detail, during preparation about 1 mg of the sample was ground finely with 100 mg of anhydrous KBr to remove scattering effects from large crystals. This powder mixture was then pressed at 8000 psi into 7 mm diameter disc to form a translucent pellet through which the beam of the spectrometer can pass through. A pure KBr disk was used as a blank. Curve fitting, peak deconvolution, and quantification of integral areas using Gaussian and/or Lorentzian functions were done using MagicPlot software (Magic Plot Systems LLC).

Raman spectroscopy

Raman spectrometry was also used to characterize the vibrational structure of the samples, to assess the presence of functional groups, and to study variations in local order. Raman spectra were collected under backscattering geometry with a LabRAM-HR spectrometer (Jobin-Yvon, Horiba, Japan). The excitation line was provided by a diode laser emitting at a wavelength of 532 nm and a Peltier cooled charge-couple device (CCD) (1064x256 pixels) was used as detector. A diffraction grating of 600T grooves/mm was used. The final spectrum resulted by the average of 3 acquisitions (acquisition time = 250 s). Curve fitting, using Gaussian functions, and quantification of integral areas were done using MagicPlot software (Magic Plot Systems LLC).

2.2.5 Dynamic Light Scattering

Dynamic Light Scattering

Dynamic light scattering (DLS) was used to determine hydrodynamic diameter and polydispersity index of nanoparticulate samples. Nanoparticles size was measured with a Zetasizer Nano analyzer (Malvern, UK). DLS measurements were performed with backscatter detection (λ = 630 nm; θ = 173°) using as working parameters hydroxyapatite refractive index (1.63) for the nanoparticles, and water refractive index (1.33) and viscosity (0.887 cP) for the solvent. Nanoparticles concentration and solvent are reported in each chapter. The results were reported as Z-average of hydrodynamic diameters and relative polydispersity indexes of three measurements of at least 10 runs for 10 s at 25°C.

Electrophoretic mobility

Electrophoretic mobility measurement was used to determine surface charge of nanoparticulate samples, expressed in term of ζ-potential. ζ-potential measurements through electrophoretic mobility were performed on Zetasizer Nano analyzer (Malvern, UK). The measurements were carried out with a using disposable folded capillary cells (DTS1061; Malvern, UK) at 25°C and were performed with backscatter detection (λ = 630 nm; θ = 173°) using as working parameters hydroxyapatite refractive index (1.63) for the nanoparticles, and water refractive index (1.33) and viscosity (0.887 cP) for the solvent. Nanoparticles concentration and solvent are reported in each chapter. Three separate measurements (100 runs each) were collected in each case.

2.2.6 Specific surface area measurement and porosimetry

Specific surface area (SSA) of the powdered samples was measured through N_2 gas adsorption modeled by the Brunauer–Emmett–Teller (BET) method [5]. BET N_2 gas adsorption method was employed using a Surfer instrument (Thermo Fisher Scientific Inc., Waltham, MA, USA). Before the measurement, the crystalline samples were pre-treated at 100°C for 3 hours under vacuum, while the amorphous samples were pre-treated at 40°C for 15 hours under vacuum.

Pore size distribution of the samples was measured through mercury intrusion porosimetry (MIP). The pore size distribution in the range 0.0070–100 µm was analyzed by Pascal 140 and 240 porosimeters (Thermo Fisher Scientific Inc., Waltham, MA, USA) with a mercury surface tension of 0.48 N/m and a contact angle of 140°.

2.2.7 Chemical composition analyses

Inductive coupled plasma optical emission spectroscopy

Inductively coupled plasma optical emission spectroscopy (ICP-OES) was used to determine elemental composition of the samples. Quantification of Ca, P, Mg, and Sr was carried out by ICP-OES spectrometer Agilent 5100 ICP-OES (Agilent Technologies, Santa Clara, CA, USA). Samples were prepared by dissolving 10 mg of sample powder in 50 mL of 1 wt. % HNO_3 solution. Standard solutions of investigated atoms were used for creating a concentration/emission calibration curve in the concentration range 1 – 100 ppm, and were obtained by dilution of certified 1000 ppm standards (Sigma Aldrich, St. Luis, MO, USA).

Fluoride ion selective electrode

Fluoride ion selective electrode (ISE) was used to quantify fluoride content in the samples. Quantification of F was performed with a fluoride ion selective electrode (Intellical™ ISEF121, Hach Lange, Loveland, CO, USA). Samples were prepared as reported in paragraph 2.8.1. Standard fluoride solutions were used for creating a concentration/potential calibration curve in the concentration range 1 – 100 ppm, and were made from anhydrous NaF. Measurements were conducted in total ionic strength adjustment buffer solution provided by instrument manufacturer.

2.3 Bibliography

1. Campodoni, E., *Design and development of bio-hybrid multifunctional materials for regenerative medicine*. 2019, Università degli studi di Parma.
2. Coelho, A., *Topas Academic V5.* Coelho Software, 2012.
3. Roche, K.J. and K.T. Stanton, *Measurement of fluoride substitution in precipitated fluorhydroxyapatite nanoparticles.* Journal of Fluorine Chemistry, 2014. **161**: p. 102-109.
4. Hughes, J.M., M. Cameron, and K.D. Crowley, *Structural variations in natural F, OH, and Cl apatites.* American Mineralogist, 1989. **74**(7-8): p. 870-876.
5. Brunauer, S., P.H. Emmett, and E. Teller, *Adsorption of gases in multimolecular layers.* Journal of the American Chemical Society, 1938. **60**(2): p. 309-319.

Chapter 3. Calcium phosphate nanoparticles for drug delivery

As already stated in the introduction, calcium phosphate nanoparticles have several intrinsic advantages that make them an excellent material for drug delivery. First, CaP NPs are totally biocompatible up to high administration doses, are non-immunogenic, and get degraded in the body into non-toxic byproducts – calcium and phosphate ions [1]. Second, CaP NPs can bind and deliver a wide range of drugs, from chemotherapeutic agents, antimicrobics, nucleic acids, peptides, and many others [2, 3]. Third, the preparation of CaP NPs is usually a simple and cheap process that respects the principles of green chemistry, and it can be easily scaled up at industrial level. Last, but not least, CaP NPs possess a pH-dependent solubility that makes these nanoparticles naturally stimuli-responsive, since drug release can be associated to nanoparticles dissolution triggered by a decrease of pH.

An additional property of CaP NPs for drug delivery is that some therapeutic agents can be encapsulated within the nanoparticle, thus protecting the payload from degradation in the biological environment. This feature is particularly relevant for therapeutic biomolecules such as nucleotides or peptides. Indeed, for these biomolecules the *in vivo* delivery, stabilization, efficacy of overexpression and cell targeting have resulted so far to be inadequate because can be easily degraded by the organism before reaching their active site, thus making therapeutic biomolecules ineffective. So for these therapeutic biomolecules the use of CaP NPs as drug carrier is particularly favored, since the protective action of CaP NPs is well-known [4-6].

The most important characteristic of CaP NPs is that all the above-mentioned features can be tailored for the desired application by changing nanoparticles physicochemical properties like their morphology, size, stability, surface properties, and chemical composition. This feature is necessary for a successful application of the functional by design approach.

Part of the content of this chapter has been published in Science Translational Medicine 2018, 10(424), eaan6205 as "*Miragoli M., Ceriotti P., Iafisco M., Vacchiano M., Salvarani N., Alogna A., Carullo P., Ramirez-Rodríguez G.B., Patrício T., Degli Esposti L., Rossi F., Ravanetti F., Pinelli S., Alinovi R., Erreni M., Rossi S., Condorelli G., Post H., Tampieri A. and Catalucci D. Inhalation of peptide-loaded nanoparticles improves heart failure*".

In this chapter will be reported the research work on the functional by design preparation of biomimetic calcium phosphate nanoparticles for drug delivery. The aim of the works was to produce drug-loaded CaP NPs that possess the most suitable properties for delivering efficiently a therapeutic payload to the chosen target organ. Specifically, the research work reported in subchapter 3.1 was focused on the use of peptides as therapeutic agents for treating cardiovascular diseases, CaP NPs both as carriers and as protective agents, and inhalation as administration route.

3.1 Drug delivery to the hearth – inhalable calcium phosphate nanoparticles

3.1.1 Introduction

The nanomedicine is at the forefront of innovation for modern health care and represents a promising approach for efficient delivery of therapeutics [7-9]. In line with this, a collection of first-generation nanoproducts for clinical use have recently been approved by the U.S. Food and Drug Administration, and other liposomal and polymer drug conjugate nanosystems are under clinical and preclinical development [10-13]. However, despite remarkable advances in the use of nanoparticles in the cancer field, very few preclinical tests have been reported for nanomedicine applied to the treatment of cardiovascular diseases (CVDs) [14-16] that, claiming 17,5 million lives a year and accounting for an estimated 31% of all deaths globally, stand as the leading cause of death worldwide [17]. The identification of innovative therapeutic nanoformulations, use of alternative administration routes, or a combination of both may help to overcome the limitations associated with current pharmacological treatments for CVDs and lead to more specific and efficient therapies.

Drug administration for the treatment of myocardial disease currently includes either oral or needle-based routes [18]. However, enteral resorption is unreliable during acute or chronic gastrointestinal congestion, whereas injection, either intravenous, subcutaneous, or intramuscular, is associated with patient discomfort and malcompliance, rendering these administrations suboptimal for chronic treatment. Moreover, home or ambulatory care is frequently required for injection procedures. In literature there is no study has addressed the possibility of using nanoparticles that can treat cardiac conditions when inhaled. Although inhalation delivery is a common procedure for the treatment of respiratory problems, no pharmacological therapies are currently adopting an inhalation approach for the delivery of therapeutics via nanoparticles to the heart. Furthermore, despite an increasing interest in peptide therapeutics in pharmaceutical research and development, no effective, noninvasive, peptide-based treatment of cardiac dysfunction has been successfully developed so far, leaving the parental route (injection) the only currently available option [19, 20].

In this subchapter is shown that inhalation therapy is effective for delivering nanoparticle-based therapeutic peptide to the diseased heart. The approach was based on biocompatible and biodegradable negatively charged CaP NPs that, via a biomineralization-inspired strategy, were produced with a diameter ranging from 20 to 50 nm and were able to deliver bioactive molecules

to cardiac cells [21]. Without promoting toxicity or interfering with any functional properties of cardiomyocytes, CaP NPs were shown *in vitro* to successfully cross the cardiomyocyte cellular membrane and release bioactive molecules (microRNAs) inside the cell [21]. Thus it was sought to assess whether the cardiac targeting of CaP NPs could be applied for the delivery of therapeutic peptides via the respiratory tree through inhalation (Figure 3.1). The rationale for the use of this unconventional administration route for targeting of the heart is based on the concepts that (i) during respiration the oxygenated blood moves from the pulmonary circulation first to the heart via the pulmonary vein and (ii) combustion-derived nanoparticles and ultrafine particulates inhaled through polluted air were recently shown [22, 23] to be present in the heart and causally associated with cardiac arrhythmia and dysfunction, suggesting that inhaled nanoparticles are deposited in the heart. Furthermore, CaP NPs can protect peptides from immediate enzymatic degradation and provide cellular permeability via the membrane internalization [21, 24]. CaP NPs can be produced with a negative surface charge, which is more compatible with the intrinsic charge of well-polarized excitable cells (i.e., cardiomyocytes) and facilitates the formation of life-compatible nanopores and cellular internalization of NPs [21].

Thus, it was predicted that inhaled small-sized CaP NPs would be able to cross the alveolar-capillary barrier in the lung and rapidly translocate to the myocardium for effective intracellular release of therapeutic peptides.

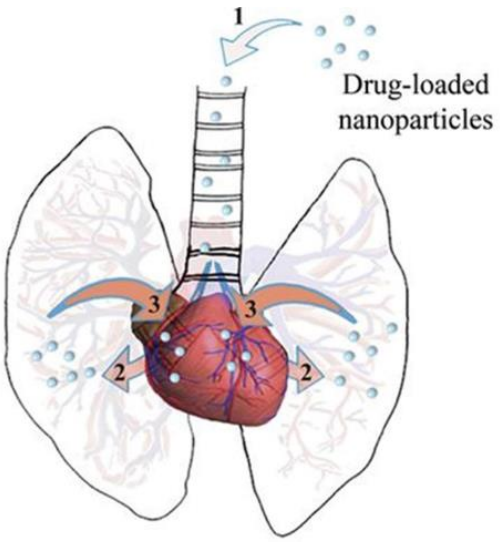

Figure 3.1. Schematic representation of CaP NPs heart targeting via the inhalation route. 1, nanoparticle inhalation; 2, nanoparticle deposition in lungs and translocation through the air-blood pulmonary barrier; 3, heart targeting and drug release into the heart.

3.1.2 Sample preparation and characterization

Sample preparation

CaP NPs were generated according to the work of Di Mauro *et al.* [21] through a biomineralization-inspired strategy consisting of mixing (1:1, v/v; 20 mL total) two aqueous solutions of (i) $CaCl_2$ (100 mM) + Na_3Cit (400 mM) and (ii) Na_2HPO_4 (120 mM). pH was adjusted to 8.5 by adding 0.1 M NaOH. The mixed solution was kept in a water bath at 37°C for 5 min. For conjugation with the fluorophore, Cy7 (125 µg/mL) was added, whereas for drug conjugation, peptides (scramble hemagglutinin peptide or therapeutic mimetic peptide, 500 µg/mL) were added. To remove unreacted reagents, the CaP NPs suspension was dialyzed for 6 hours across a cellulose dialysis membrane with a cutoff of 3500 Da and immersed in 400 mL of Milli-Q water followed by multiple water exchanges. The suspension was recovered and stored at 4°C until further use. The final concentration of CaP NPs suspensions was 600 µg/mL in all cases. The final concentrations of Cy7 and peptides within the CaP suspension were 75 and 150 µg/mL, respectively. Surface decoration of CaP NPs with Cy7 was also tested by adding an aqueous solution of Cy7 to the CaP suspension (final concentration of 15 µg/mL similar to the amount effectively encapsulated). The suspension was maintained overnight under shaking at 37°C. After that, the unadsorbed fluorophore was removed by extensive washings by centrifugation.

Nanoparticles characterizations

The concentration of CaP NPs after dialysis was evaluated by freeze-drying the sample suspensions (five aliquots of 1 mL) and weighing the solid content. CaP NPs were evaluated by TEM, DLS, and electrophoretic mobility. DLS and electrophoretic mobility measurements were carried out suspending CaP NPs in 10 mM HEPES buffer at pH 7,4.

The stability of CaP, CaP-MP, and CaP-HA stored in aqueous solution (at the native concentration of 600 µg/mL) at 4°C starting immediately after dialysis was evaluated by DLS and electrophoretic mobility as a function of time (up to 8 days). The stability of the unloaded CaP suspension 2 days after dialysis enriched with 10% (v/v) of FBS was also evaluated for up to 7 days at room temperature by DLS and electrophoretic mobility.

The degradation of CaP NPs and CaP-peptides at different pH values was evaluated by mixing 5 mg of freeze-dried nanoparticles with 10 mL of 0,1 M HEPES buffer solution (pH 7,4) or 10 mL of 0,1 M acetate buffer solution (pH 5,5). At scheduled times for up to 24 hours, 1 mL of the supernatant (that was well separated from the solid phase by 15 min of centrifugation at 5000

RPM) was removed for Ca^{2+} quantification and replaced with fresh buffer. Calcium content was determined by ICP-OES.

To evaluate peptide loading, the DC Protein Assay (Bio-Rad, Hercules, CA, USA) was adopted according to the manufacturer's instructions. Quantification of both the pre- and post-dialysis preparations was performed from both pellet (CaP-MP) and supernatant (CaP-free MP) fractions obtained by centrifugation (14 min at 20,000 g) of CaP-MPs. Before the peptide quantification assay, both pellet and supernatant fractions were subjected to an acidic treatment (0.05 M HCl for 4 hours) to completely dissolve CaP-MPs and facilitate the total release and effective quantification of total MP.

The amount of Cy7 loaded on CaP NPs was measured using an ultraviolet-visible (UV-Vis) spectrophotometer (NanoDrop One, Thermo Fisher Scientific Inc., Waltham, MA, USA) (λ = 750 nm; ε_{cy7} = 240,600 $M \cdot cm^{-1}$). The concentration of Cy7 was calculated as the difference between the concentration of the initial solution and that of the supernatant after sample centrifugation at 5000 RPM for 15 min. The release of Cy7 from CaP-Cy7 was tested against an infinite sink in dialysis by transferring the particles into 3500-Da molecular weight cutoff cellulose membrane dialysis tubes and dialyzing against water for 24 hours with multiple water exchanges. At scheduled times, 10 µL of the supernatant (that was well separated from the solid phase by 15 min of centrifugation at 5000 RPM) was analyzed for fluorophore quantification using a UV-Vis spectrophotometer. The release of Cy7 from CaP-Cy7 was also tested in aqueous solution (at the native concentration of 600 µg/mL) enriched with 10% (v/v) of FBS. At scheduled times, ranging from 1 min to 24 hours, 10 µL of the supernatant (that was well separated from the solid phase by 15 min of centrifugation at 5000 RPM) was analyzed for fluorophore quantification using a UV-Vis spectrophotometer.

Animal experiments

The animal experiments illustrated in this sub-chapter of this Ph.D thesis were carried out in collaboration with the Humanitas Clinical and Research Center, Rozzano, Milan, Italy (Dr. Paola Ceriotti, Dr. Marco Vacchiano, Dr. Nicolò Salvarani, Dr. Pierluigi Carullo, Dr. Michele Miragoli, and Dr. Daniele Catalucci), and Berlin Charité Institute of Health, Berlin, Germany (Dr. Alessio Alogna and Dr. Heiner Post).

Study design

The overall hypothesis is to target the diseased heart via inhaled nanoparticles carrying therapeutic peptides. Here, we designed a study to (i) synthesize a proper CaP-based MP carriers, (ii) test the effectiveness of CaP inhalation in small (mice), medium (rats), and large (pigs) animals, and (iii) treat a typical diabetes-induced cardiomyopathy via inhalation of CaP-MPs. In the setting for functional, histological, and molecular evaluations and cardiac activity monitoring, the number of animals per each individual group was minimized to 6 to 11 mice, 11 rats, and 9 pigs. For the therapeutic application, the sample size of diabetes-induced heart failure model was determined on the basis of previous experience [25] and taking into account the mortality rate. The study, which included 10 mice per individual group, was blinded and randomized. To ensure comparable degrees of cardiac dysfunction, noninvasive approaches such as echocardiography or electrocardiogram (ECG) were assessed at each experimental time point. To ensure that neither the nanocarrier nor therapeutic peptide alone was responsible for the improved cardiac phenotype, we included mice that inhaled CaP-HA and MP, respectively. The large animal experiments were designed to achieve a proof of concept of the feasibility of our nanocarrier-mediated approach using a small number of animals (nine in total). The statistical analysis is therefore primarily descriptive in nature. The first series of animals was aimed at testing inhaled CaPs' ability to enrich the heart at a dose derived from previous experiments in rodents. After collecting evidence of heart enrichment via Western blotting, a separate set of animals was used to investigate the hemodynamic and electrophysiological effect of the carrier per se. Numbers were determined by the investigator according to previous experimental experience. All experimental procedures were approved by the Institutional Animal Care and Use Committee (permit no. 920/2015-PR, 746/2017-PR, 59/2012, and G0063/16) and conducted in accordance with the guidelines of the national councils where experiments were performed.

Mice. All experiments were performed on 10-week-old C57B6J male mice, CD1 male mice, and CD1-Foxn1 nude mice. All animals were obtained from the Charles River Laboratories. Therapeutic treatment of mice was performed as follows: Type 1 diabetes was induced in adult C57B6/J male mice by intraperitoneal injection of streptozotocin (STZ) (50 mg/kg per day) for five consecutive days as previously described [25]. Seven days after the last STZ injection, whole blood was obtained from the mouse tail vein and glucose levels were measured using the Accu-Chek Aviva blood glucose monitoring system (Roche). Mice were fasted for 8 hours before blood collection. At 3 weeks after STZ treatment, mice were considered diabetic and used for the study only if glucose > 250 mg/dl and fractional shortening < 35% (29 of 36 STZ-treated mice were considered suitable for the study). STZ diabetic mice were randomly divided into three separate groups, and

50 µl of solution (CaP-MP, 0.5 mg/kg per day; CaP-HA, 0.5 mg/kg per day; MP, 0.5 mg/kg per day) was administered by inhalation via intratracheal nebulization for 10 consecutive days, as indicated.

Rats. The study population consisted of 11 male Wistar rats bred in the animal facility at the University of Parma, aged 12 to 14 weeks and weighing 300 to 350 g. Briefly, animals were anesthetized by intraperitoneal injection with a mixture of ketamine chloride (40 mg/kg) (Imalgene, Merial) and medetomidine hydrochloride (0.15 mg/kg) (Domitor, Pfizer Italia S.r.l.).

Landrace pigs. A total of nine healthy animals were anesthetized as previously described [26]. Briefly, after administration of propofol (1 mg/kg), the animals were intubated and anesthesia was continued with 1 to 1.5% isoflurane, fentanyl (20 µg/kg per hour), and pancuronium (0.2 µg/kg per hour). The animals were ventilated (Cato, Dräger Medical) with an FiO_2 of 0.5, an inspiratory:espiratory ratio of 1:1.5, a positive end-expiratory pressure of 5 mmHg, and a tidal volume of 10 mL/kg. If necessary, the respiratory rate was adjusted to maintain an end-tidal carbon dioxide partial pressure between 35 and 40 mmHg. Sheath accesses of the left internal carotid artery and jugular vein were surgically prepared. Heart rate and arterial blood pressure were continuously monitored. A balanced crystalloid infusion (Sterofundin ISO, B. Braun Melsungen AG) was administered at a fixed rate of 10 mL/kg per hour throughout the protocol. A body temperature of 37.5° to 38.5°C was maintained by either surface cooling or a warming blanket.

Nanoparticles administration

Mice. CD1 mice were divided into four different groups of six mice, and 100 µL of CaP-Cy7 was administered by gavage, intraperitoneal, and intravenous injection (Cap-IP) as well as by intratracheal nebulization. For the intratracheal treatment, MicroSprayer Aerosolizer (model IA-1C) and FMJ-250 High Pressure Syringe (Penn-Century) were used. Mice were anesthetized with 3% isoflurane to allow nebulization. For each administration method, 11 mice administered with an aqueous Cy7 solution were used as controls. At the end of the experimentation, mice were sacrificed and tissues were collected.

Rats. Administration was performed via a 16-gauge catheter connected to a rodent ventilator (Rodent ventilator UB 7025, Ugo Basile) for artificial respiration. One dose (20 µL/100 g of body weight) of solution (CaP, 3 mg/kg, or saline) was administered via the catheter. After CaP administration, animals were woken up with a single intraperitoneal injection of atipamezole hydrochloride (0.15 mg/kg) (Antisedan, Pfizer) and left conscious for 4 hours before

electrophysiological *in vivo* experiments were performed. Before exposing the heart, precordial ECGs (three unipolar and three bipolar leads) were recorded to screen for possible anoxic effects on cardiac electrical activity due to the tracheal instillation.

Landrace pigs. A left lateral thoracotomy was performed, and the left ventricle was exposed in a pericardial cradle. After stabilization for 30 min, two transmural LV free wall biopsies were taken from the beating heart. Next, a 10-mL solution containing CaP-HA (corresponding to an HA concentration of 150 µg/mL) was nebulized over 30 min with the Aeroneb Professional Nebulizer System (Aeroneb Pro, Aerogen Ltd.), connected with an adult T-piece into the inspiratory limb of the breathing hoses. At 30, 60, 180, and 300 min after the beginning of inhalation, further biopsies were taken. All biopsies were rinsed carefully in saline, immediately frozen in liquid nitrogen, and stored at −80°C. Finally, the animals were sacrificed by a bolus injection of 100 mM potassium chloride, and samples were collected.

Echocardiography

A Vevo 2100 high-resolution *in vivo* imaging system (VisualSonics Fujifilm) with a MS550S probe "high frame" scan head was used for echocardiographic analysis. Mice were anesthetized with 1.0% isoflurane and imaged in M-mode as previously described [25].

Invasive hemodynamics in landrace pigs

A separate group of pigs (n = 9, 88 ± 4 kg) was acutely instrumented closed-chest under fluoroscopic guidance with a pulmonary artery flotation catheter [Continuous Cardiac Output (CCO) connected to Vigilance II, Edwards Lifesciences], an LV conductance catheter (5F, 12 electrodes, 7-mm spacing; MPVS Ultra, Millar Instruments), and a valvuloplasty catheter (24 mL; Osypka) in the descending aorta as previously described [26]. A three-lead surface ECG was recorded throughout the whole experiment and used for offline analysis. Offline analysis included measurements of PQ intervals during spontaneous heart rates, QRS duration, and QT duration. After stabilization for 30 min, steady-state hemodynamics was acquired over three respiratory cycles. Pressure-volume relationships were generated by briefly inflating the intra-aortic balloon catheter three times. Next, a 10-mL solution containing CaP-HA (10 mg/mL) (HA, 150 µg/mL) was nebulized over 30 min with the Aeroneb Professional Nebulizer System as described above. Measurements were then repeated after 300 min. Pressure-volume data and time intervals were analyzed offline by CircLab software (custom-made by P. Steendjik). The conductance catheter measurements were calibrated by hypertonic saline solution (three boluses of 3 mL at 10%), and cardiac output was continuously derived from the pulmonary artery flotation catheter.

3.1.3 Results and discussion

Characterization of CaP NPs

CaP NPs were composed by round-shaped nanoparticles, ca. 50nm in diameter (fig 3.2A), and had an amorphous nature, as evinced by the lack of diffraction spots in SAED pattern (fig 3.2A), the presence of only one broad band centered at ca. 32 ° 2θ in XRD diffractogram (fig 3.2B), and by the presence of broad, unresolved bands in the FT-IR spectrum (fig 3.2C). Furthermore, FT-IR spectra evinced the presence of citrate ions on CaP NPs after washing process, as denoted by the presence of one intense band at ca. 1600 cm^{-1}, that was associated to citrate -COO^- stretching.

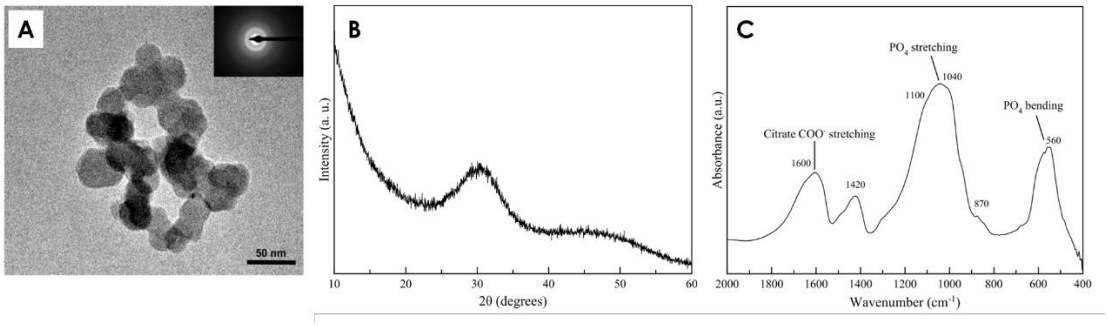

Figure 3.2. (A) TEM micrograph (inset: SAED pattern), (B) XRD diffractogram, and (C) FT-IR spectrum of CaP NPs.

Before *in vivo* administration, CaP NPs were subjected to a set of *in vitro* evaluation procedures. First, long-term stability in aqueous suspension was assessed by measurement of CaP NPs surface charge and Z-average as a function of time as well as CaP NPs interaction with proteins. No changes were found in the surface charge, which remained stable (−32 ± 3 mV) for the whole time of investigation, whereas the initial Z-average value of about 125 nm was found to decrease to about 80 nm after 2 days of storage at 4°C (fig. 3.3A). Thereafter, Z-average value remained stable with only minor variations (±10 nm) for up to 8 days, which was the time limit for the investigation. The apparent decrease of size after 2 days of storage was attributed to nanoparticles disaggregation and stabilization that occurred when purification by dialysis was terminated. To evaluate the potential interaction of proteins with CaP NPs, nanoparticles were analyzed in aqueous suspension enriched with 10% (v/v) FBS (fig. 3.3B). Z-average decreased from about 80 nm (in pure water) to about 32 nm, indicating that serum proteins interacting with the nanoparticles increased the dispersion of CaP NPs. Thereafter, a gradual increase in Z-average was

registered, reaching a value of about 280 nm after 7 days. At this later time point, an increment of the ζ-potential from −30 to −10 mV corroborated the expected surface interaction of CaP NPs with proteins. Together, these data show that no substantial size alterations occur within the first hours, suggesting that an *in vivo* administration featuring a fast targeting of the heart might not face any alteration of CaP NPs properties.

In a second step, near-infrared fluorophore-loaded CaP NPs (CaP–Cy7) were generated for *in vivo* biodistribution analyses, and the effective encapsulation of the fluorophore in the CaP NPs as well as the stability of CaP-Cy7 were demonstrated (fig. 3.3C). To determine the effective incorporation of Cy7 into CaP NPs, comparable amounts of Cy7 were either encapsulated into (CaP-Cy7) or adsorbed after synthesis to CaP NPs, and the amount of CaP-associated Cy7 was measured, revealing an amount of 1,40 ± 0,13% (w/w) encapsulated CaP-Cy7 versus 0,85 ± 0,08% (w/w) CaP adsorbed after synthesis. The analysis of the surface charge of CaP-Cy7 at pH 7,4 revealed the presence of a single population with surface charge of about −20 mV, whereas CaP NPs with the fluorophore adsorbed on their surface showed a double population with surface charge of about −34 and −6 mV attributed to naked CaP NPs and fluorophore-coated CaP NPs (fig. 3.3C). These data support the conclusion that, when included during the synthesis of nanoparticles, Cy7 is effectively encapsulated within the CaP NPs and not attached to the surface. In addition, CaP-Cy7 did not show any release of fluorophore (limit of detection of 1 µg/mL) against an infinite sink in dialysis as well as in aqueous suspension enriched with 10% (v/v) FBS. Similar results were obtained for naked CaP NPs and CaP-MP (see below).

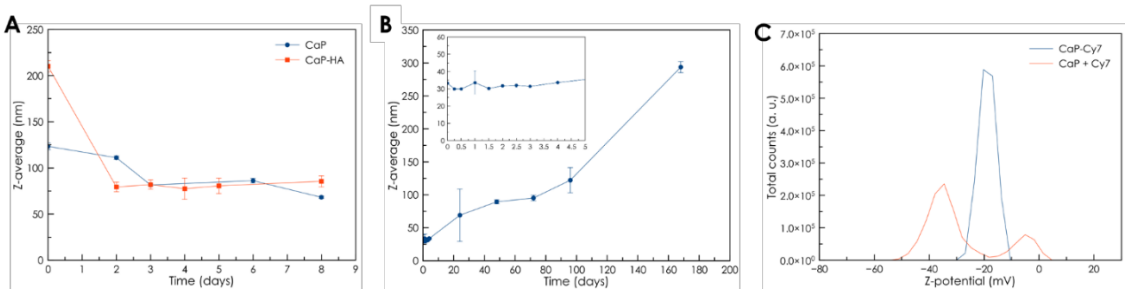

Figure 3.3. (A) Mean particles size as a function of time of pristine CaP and CaP-HA in water (native concentration, 600 µg/mL). Data points for CaP-MP were similar to those for CaP-HA and for the sake of clarity have not been included in the graph. Results are expressed as mean ± S.E.M (n = 6). Time 0 corresponds to nanoparticle immediately after dialysis. (B) Mean particles size as a function of time of CaP NPs in water (native concentration, 600 µg/mL) enriched with 10% (v/v) FBS. The inset shows the data acquired in the short time scale. Results are expressed as mean ± S.E.M (n = 6). Time 0 corresponds to dialyzed CaP NPs stored in water for 2 days. (C) ζ-potential values at pH 7,4 of CaP-Cy7 and CaP NPs with Cy7 adsorbed on their surface (CaP + Cy7).

Delivery of CaP NPs to the heart by inhalation

After CaP generation and characterization, we assessed the possibility of heart targeting by nanoparticle administration. CaP-Cy7 were delivered to healthy mice, and fluorescence measurements were performed to compare distinct administration routes, which, in addition to conventional ways (oral (gavage), intraperitoneal, and intravenous), included nebulization of CaP-Cy7 via the respiratory route. Whereas enteral administration (gavage) did not result in statistically significant ($P > 0.05$) targeting to the heart at 40 min after administration, parenteral administration (intraperitoneal and intravenous) and inhalation resulted in rapid delivery of CaP-Cy7 to the myocardium, with inhalation being the most efficient delivery method (Figure 3.4A and B). Notably, the time course of CaP-Cy7 myocardial accumulation was paralleled by a gradual reduction in signal from the lungs as a function of time, suggesting a continuous passage of nanoparticles across the pulmonary barrier (Figure 3.4B). Similar results were obtained via an optical *in vivo* imaging approach, which allowed us to monitor the behavior of inhaled CaP-Cy7 and their gradual accumulation in the mediastinum, the thoracic cavity containing the heart, esophagus, and trachea (Figure 3.4C). A delayed clearance of inhaled CaP-Cy7 was observed compared to Cy7 alone (Figure 3.4C), which was supported by three-dimensional fluorescence molecular tomography (FMT) imaging of the cardiopulmonary area from mice 60 min after inhalation, revealing marked localization of CaP-Cy7 in the myocardium compared to Cy7 alone (Figure 3.4D). Effective delivery of CaP-Cy7 to the myocardium was further confirmed by fluorescence analyses on explanted hearts after a low-dose (50 µL) or an high-dose (100 µL) administration (Figure 3.4E), whereas no specific cardiac targeting was found in Cy7 alone, which rapidly accumulated in the bladder after rapid and broad diffusion in the lungs and in the rest of the body. In addition, no CaP-Cy7s were found to cross the blood-brain barrier (Figure 3.4C).

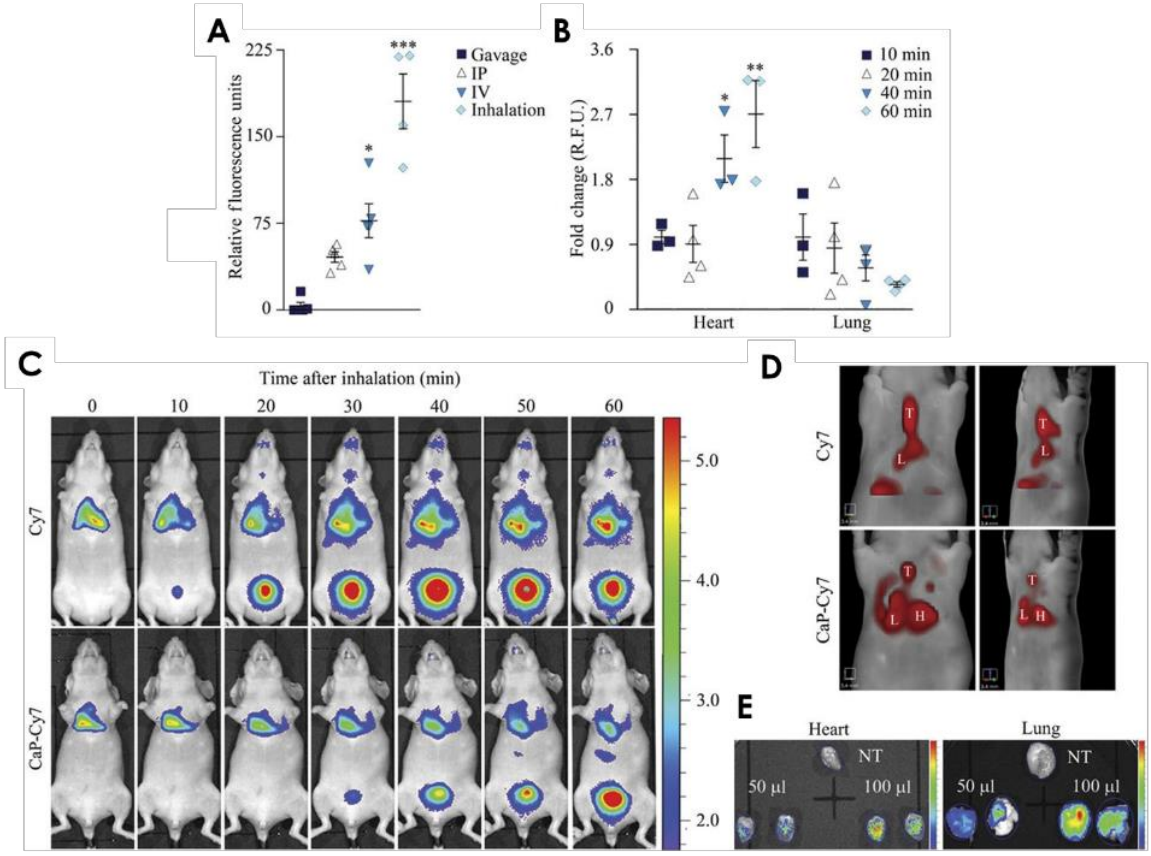

Figure 3.4. (A) Quantification of Cy7 fluorescence signals from heart tissue of mice treated with CaP-Cy7 via gavage, intraperitoneal (ip), intravenous (iv), and inhalation administration. Data are means ± SEM. *P < 0.05 and ***P < 0.001 compared to gavage [one-way analysis of variance (ANOVA) test] (n = 5). (B) Time-course quantification of Cy7 fluorescence signals from heart and lung tissue of mice treated with CaP-Cy7 via inhalation administration. Data are means ± SEM. *P < 0.05 and **P < 0.01 compared to the 10-min time point (two-way ANOVA test) (n = 5). R.F.U., relative fluorescence units. (C) Whole-body optical *in vivo* imaging to evaluate the distribution of CaP-Cy7 and Cy7 in CD1 nude mice at different time points after inhalation. Data are representative of at least six independent experiments. Values are expressed as radiance efficiency (×109). (D) 3D FMT imaging of mice as presented in (C) and analyzed 60 min after CaP-Cy7 and Cy7 administration. T, trachea; H, heart; L, lung. (E) Fluorescence imaging of explanted hearts from perfused mice analyzed 60 min after inhalation of 50 and 100 µl of CaP-Cy7. NT, heart from non-treated mouse. Values are expressed as radiance efficiency. Scale values: heart, 1.04 × 107 (maximum) to 3.56 × 106 (minimum); lung, 7.78 × 107 (maximum) to 6.17 × 106.9 (minimum) (n = 4).

Notably, in contrast to the toxic outcome associated with inhalation of ultrafine particulates from polluted air and other inorganic nanoparticles such as TiO_2, SiO_2, and Co_3O_4 nanoparticles [27-30], pulmonary CaP NPs administration via single or multiple once-a-day administration protocols did not affect cardiac function as measured by echocardiography. In rats, no alterations in cardiac excitability and refractoriness were detected as shown by the absence of arrhythmogenic events evaluated by *in vivo* epicardial multiple lead recordings. Furthermore, no immunological effects were observed, as indicated by no detectable changes in RNA expression of CD11, interleukin-1 (IL-1), tumor necrosis factor (TNF), IL-6, IL-4, and IL-5. In agreement with previous works on

biomimetic CaP NPs [21], this evidence supports the concept that biomimetic CaP NPs, closely resembling the inorganic phase of bone and teeth [31], are recognized by the body as close to endogenous material, thus being biocompatible and well tolerated *in vivo*.

Efficacy of CaP NPs to load therapeutic peptides

On the basis of the demonstration that CaP NPs inhalation allows nanoparticles to cross the pulmonary barrier and reach the intracellular compartment within the heart, the next objective was to explore the use of peptide-loaded CaP NPs for cardiac treatment *in vivo*. Catalucci *et al.* has recently demonstrated the therapeutic effect of a cell-penetrating mimetic peptide (arginine modified mimetic peptide, R7W-MP) that, by targeting the $Ca_V\beta 2$ cytosolic subunit of the L-type calcium channel (LTCC), improves cardiac contractility in pathological heart conditions associated with alterations of LTCC levels and function (diabetic cardiomyopathy) via restoration of LTCC density at the plasma membrane [25]. Here, it was envisioned to test the therapeutic use of CaP NPs for peptide delivery for the treatment of a cardiac condition via inhalation of CaPs loaded with R7W-free MP (CaP-MP). Because of the absence of the cell-internalizing R7W sequence on the MP, its efficiency in rescuing cardiac contractility would require the CaP NPs to mediate its crossing of the pulmonary barrier and subsequent myocardial cell internalization.

In the previous study of Di Mauro *et al.* [21], CaP NPs were functionalized with different quantities of microRNA, revealing a slight increase in nanoparticles size as a function of microRNA amount, whereas comparable values to those of microRNA-free CaP NPs were obtained for the surface charge and morphology. Here it was performed a similar evaluation and characterized the effect of MP and hemagglutinin (HA) scramble peptides, on size and surface of loaded CaP NPs. Notably, because the approach is based on a universal nature-inspired synthetic strategy, we found that the incorporation mechanism for peptides into CaP NPs was similar to the one previously observed for microRNAs. This mechanism consists of a first step of interaction in which, within a basic reaction environment (pH 8.5), the Ca^{2+} and/or PO_4^{3-} ions interact via a strong electrostatic interaction with the chemical groups (carboxylate, amine, and sulfonic groups) of the analyzed biomolecules. Whereas, in the case of Cy7, mainly sulfonic and amine groups are likely to be involved in the interaction, the negative charge of MP and HA peptides, which at the pH of the reaction have a calculated isoelectric point of 7,06 [32], generally interacts with Ca^{2+} ions. Afterward, the reaction of PO_4^{3-} with Ca^{2+} ions or vice versa triggers the nucleation of particles

and their growth, resulting in the mineralization of biomolecules (creation of a matrix of mineral phase surrounding the biomolecule-rich nucleus). During this process, citrate stabilizes the nanoparticles and modulates their growth through its binding on the surface at the early stage of crystallization, as previously reported [21].

In line with the previous results obtained with microRNA [21], immediately after dialysis, higher Z-average, but similar surface charge, was obtained for functionalized CaP NPs compared to peptide-free CaP NPs. CaP-MP and CaP-HA showed comparable values of surface charges (−31 ± 2 mV and −32 ± 1 mV), respectively, indicating that their surface is homogenously covered with citrate. Z-averages for the functionalized CaP-MP and CaP-HA were 210 ± 6 nm and 220 ± 6 nm, respectively, where the effective interaction of peptides with CaP NPs might be responsible for the slight difference in size with respect to peptide-free CaP NPs (125 nm). Also in this case, the Z-average of CaP-HA and CaP-MP immediately after dialysis decreased as a function of time, passing from about 200 to 90 nm after 2 days (Figure 3.3A). This value remained stable with small variation (±10 nm) for up to 8 days, which was the time limit for the investigation. Consistently, also in this case, the surface charge of the CaP-peptides (−31 ± 3 mV) did not change as a function of time. TEM micrographs of CaP-MP and CaP-HA (Figure 3.5) collected immediately after dialysis showed round-shaped particles of about 20 to 50 nm in diameter. The discrepancy in particle size between TEM micrographs and DLS Z-average is due to the fact that the two techniques are not comparable, since with the former the inorganic core is measured and in the second the hydrodynamic diameter of particle and solvation shell is measured. The SAED patterns collected from the same CaP NPs (Figure 3.5) demonstrated their amorphous nature due to the presence of diffuse rings rather than spots. In addition, EDS spectra (Figure 3.5) revealed that both CaP-MP and CaP-HA are mainly composed of calcium and phosphate. All these features are comparable with our previously prepared CaP NPs [21], and therefore it can be assumed that the functionalized CaP NPs synthesized in this work have similar behavior toward cardiomyocytes and cardiac tissue.

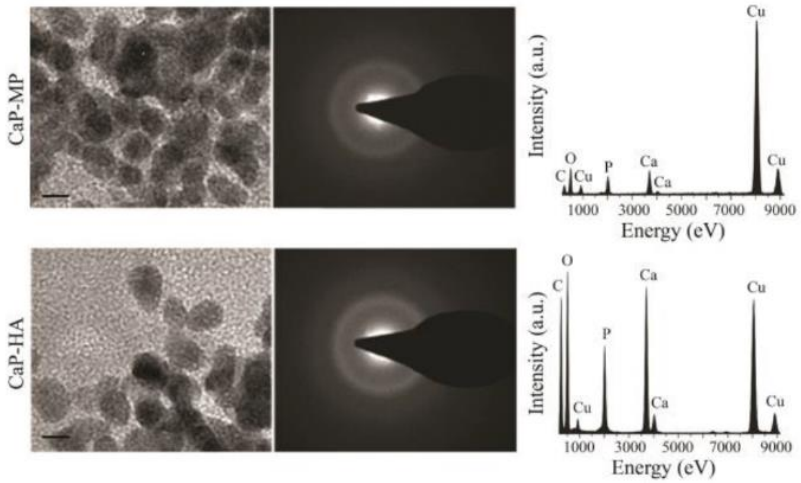

Figure 3.5. TEM micrographs (left), SAED patterns (middle), and EDS analysis (right) of CaP-MP (upper panel) and CaP-HA (lower panel). The Cu signal is due to the sample holder. Scale bar = 50 nm.

To evaluate peptide loading, the total MP in CaP-MP preparations was quantified. To distinguish the amount of CaP-loaded MP from the possible CaP-free MP present in the preparations, peptide quantification was performed from both pellet (CaP-MP) and supernatant (CaP-free MP) fractions obtained by centrifugation. Finally, acidic treatment was performed to completely dissolve CaP-MPs from both fractions, thereby facilitating the total release and effective quantification of total MP. The same approach was used for both the pre- and post-dialysis preparations, and data were compared to the theoretical maximum loading. MP loading from the pellet fraction (corresponding to the CaP-loaded MP) was comparable to the theoretical value, leading to the conclusion that CaP NPs provides high loading capacity, keeping the amount of unloaded peptide (CaP-free MP) at a minimum.

To evaluate MP stability within nanoparticles, peptide quantification was performed on CaP-MP aliquots stored at different amounts of time at room temperature using the approach described previously. As shown in Figure 3.6A, no reduction in MP loading was found until 10 hours of storage at room temperature, whereas a slight decrease was observed at 24 hours of storage, supporting the conclusion that CaP-MP stably maintain their payload in an encapsulated state. Thereafter, after a time-dependent response to CaP NPs dissolution under acidic conditions, we evaluated release kinetics of encapsulated peptide from nanoparticles. As shown in Figure 3.6B, a gradual release of MP from CaP-MP was obtained, showing an inverse relationship between the reduction in the pellet fraction (CaP-loaded MP) and an increase in the supernatant fraction (CaP-free MP). These data are in line with results from inductively coupled plasma optical emission spectrometry (ICP-OES) analyses (Figure 3.6C) that, by measuring the cumulating Ca^{2+} ion release

under physiological (pH 7,4) and slightly acidic (pH 5,5) conditions, provide degradation rate of CaP NPs and peptide-loaded CaP NPs as a function of time. Degradation and consequently peptide release are triggered by a drop in pH. Together, these data provide the evidence that CaP NPs have high loading capacity and keeping the amount of unloaded peptide (CaP-free MP) at a minimum.

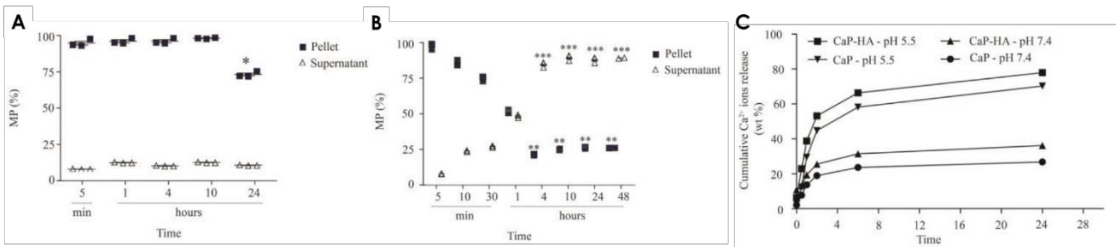

Figure 3.6. (A) Stability of CaP-MP loading. Time-dependent release profile of MP from CaP-MP preparations. Data are expressed as average percentage over time. *P < 0.05 vs. the initial time point of analysis. Results are expressed as mean ± SEM (n = 6) (two-way ANOVA test). (B) MP release from CaP-MP. Time-dependent release profile of MP from acidic dissolution of CaP-MP preparations. Data are expressed as average percentage over time. **P < 0.01, ***P < 0.001 vs. the initial time point of analysis. Results are expressed as mean ± SEM (n = 6), (two-way ANOVA test). (C) Cumulative release of Ca^{2+} ions (wt%) from CaP NPs and CaP-HA at pH 7,4 and pH 5,5 as a function of time. Data points for CaP-MP were similar to those for CaP-HA and for the sake of clarity have not been included on the graph. Results are expressed as mean ± SEM (n = 6).

Efficacy of inhaled CaP NPs loaded with a therapeutic MP to improve myocardial contraction

To test the therapeutic use of CaP-MP for the treatment of a cardiac condition, a mouse model of streptozotocin (STZ)–induced diabetic cardiomyopathy was treated via inhalation of CaP NPs loaded with R7W-free therapeutic peptide. To verify the ability of CaP NPs to mediate cardiomyocyte internalization [21], stimulated emission depletion (STED) 3D z-stack microscopy of isolated adult cardiomyocytes from mice subjected to inhalation of MP-rhodamine–loaded CaP NPs was performed. MP-rhodamine–loaded CaP NPs have the same size and surface charge of CaP-MP, and STED 3D z-stack microscopy showed effective targeting of MP to cardiomyocytes, accounting for 124 ± 52 fluorescent signals (corresponding to the internalized MP-rhodamine–loaded CaP NPs) per single cell (Figure 3.7).

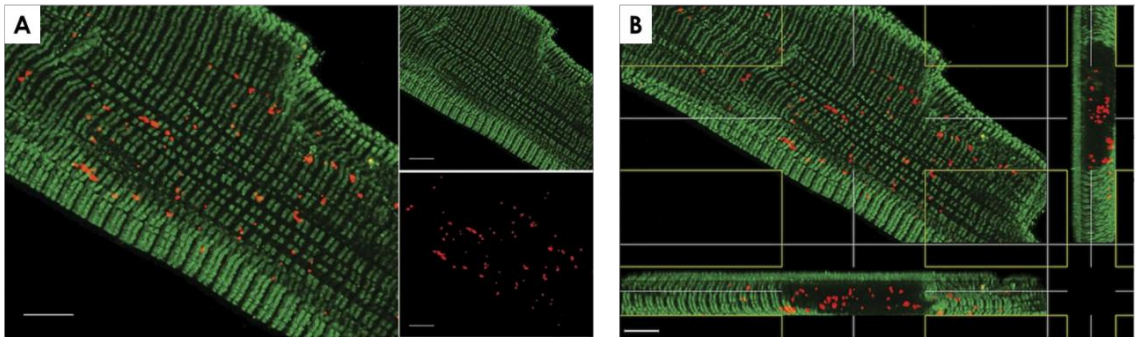

Figure 3.7. (A) STED microscopy on an isolated cardiomyocyte from mice treated with MP-rhodamine–loaded CaP NPs. Green, LTCC; red, MP-rhodamine. Representative of 10 different acquisitions. Original magnification, ×100; scale bars, 5 µm. (B) Orthogonal view of isolated cardiomyocyte in (A). Original magnification, ×100; scale bars, 5 µm.

In agreement with this, CaP-MP inhalation treatment of diabetic mice (Figure 3.8A) led to a complete recovery of cardiac function as shown by echocardiographic assessment of left ventricular (LV) function (Figure 3.8B and C). Improvement of molecular and cellular defects associated with diabetic cardiomyopathy was achieved as a result of the direct targeting of MP to LTCC [25], including restoration of LTCC protein levels (Figure 3.8D), recovery of LTCC currents (Figure 3.8E), and LTCC-related contractile properties (Figure 3.8F) as determined in isolated cardiomyocytes from CaP-MP–treated mice.

In contrast, as expected, no therapeutic effects were obtained by administration of CaP-HA or unloaded (free) MP (Figure 3.8, B to F). In addition, no induction of oxidative stress was observed by thiobarbituric acid–reactive substance detection test. Together, these data provide evidence that inhalation of MP-loaded CaPs is an effective approach for delivery of therapeutic peptides to the heart (Figure 3.8G) and demonstrate the benefit of CaP-MP inhalation in recovering LTCC-associated cardiac dysfunctions.

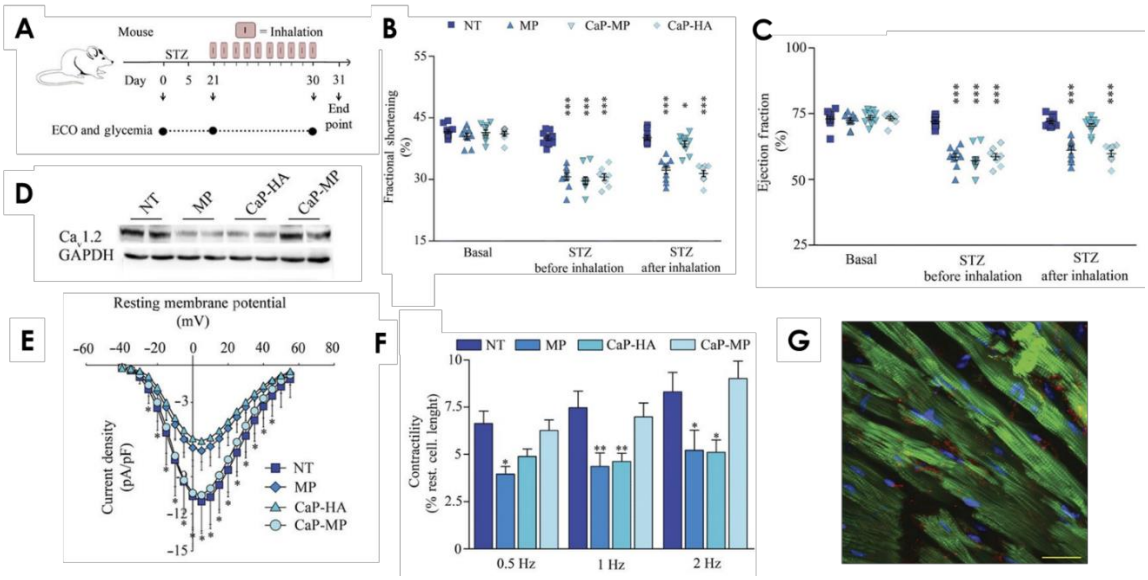

Figure 3.8. (A) Design of the study. ECO, echocardiography. (B) LV fractional shortening and (C) ejection fraction (indices of cardiac contractile function) as determined by echocardiographic analysis on STZ-treated mice treated as indicated. Data are means ± SEM. ***P < 0.001 compared to NT mice (two-way ANOVA test) (n = 10). (D) Western blot analysis for the LTCC pore unit (Cavα1.2) on adult cardiomyocytes isolated from treated mice. GAPDH, glyceraldehyde-3-phosphate dehydrogenase. (E) Average peak of LTCC current density as a function of voltage command measured in adult cardiomyocytes isolated from treated mice. All values are means ± SD for n cells. *P < 0.02 for NT compared to MP and CaP-HA mice (n = 16 to 21). (F) Contractility of adult cardiomyocytes isolated from treated mice. Data are means ± SEM. *P < 0.05 and **P < 0.01 compared to NT mice (two-way ANOVA test) (n = 20). (G) Z-stack confocal laser scanning microscopy images showing HA peptide in myocardial tissue from mouse treated by CaP-HA inhalation. Immunofluorescence staining for HA (red), LTCC (green), and cell nuclei [4',6-diamidino-2-phenylindole (DAPI); blue]. Scale bar, 20 µm (n = 3).

Effectiveness of peptide-loaded CaP formulation for targeted administration to the heart in a porcine model

Finally, to advance toward clinical research in humans and generate the first proof of concept in large animals, feasibility of cardiac targeting via our nanoparticle-based inhalation approach was assessed by nebulization of CaP-HA in anesthetized healthy landrace pigs (Figure 3.9A). It was chosen to use healthy animals and a non-therapeutic peptide for keeping the system as simple as possible, in order to prove that CaP NPs can target the cardiac district and deliver a payload also in large animals. Similar to our results in mice, no changes in heart rate, mean arterial blood pressure, cardiac output (9.8 ± 0.8 versus 9.9 ± 0.8 L min^{-1}), or systemic and pulmonary vascular resistance were observed 5 hours after a single inhalation of CaP-HA (Figure 3.9B). LV function, as assessed by hemodynamic measurements of pressure-time–derived parameters (LV maximum pressure, maximum and minimum LV d*P*/d*t*) and pressure-volume analyses (end-diastolic and

end-systolic pressure-volume relationships), did not change (Figure 3.9C). No arrhythmia occurred, and surface electrocardiography–derived PQ (133 ± 6 versus 135 ± 5 ms), QT intervals (349 ± 12 versus 345 ± 19 ms), and QRS duration (56 ± 5 versus 51 ± 5 ms) remained constant. Finally, respiratory function (end-tidal carbon dioxide partial pressure and arterial oxygen saturation) remained stable at constant mechanical respiration. In a separate group of open-chest pigs, LV free wall biopsies from the beating heart were taken at baseline and sequentially after treatment. Three hundred minutes after inhalation, a marked HA signal was detected in the myocardium, providing evidence for effective delivery of CaP-HA to the heart. These data were supported by Western blot (Figure 3.9D) and confocal microscopy (Figure 3.9E) analyses of cardiac tissue. Together, these data confirm the efficiency of CaP NPs inhalation approach for intramyocardial delivery of compounds in a large animal.

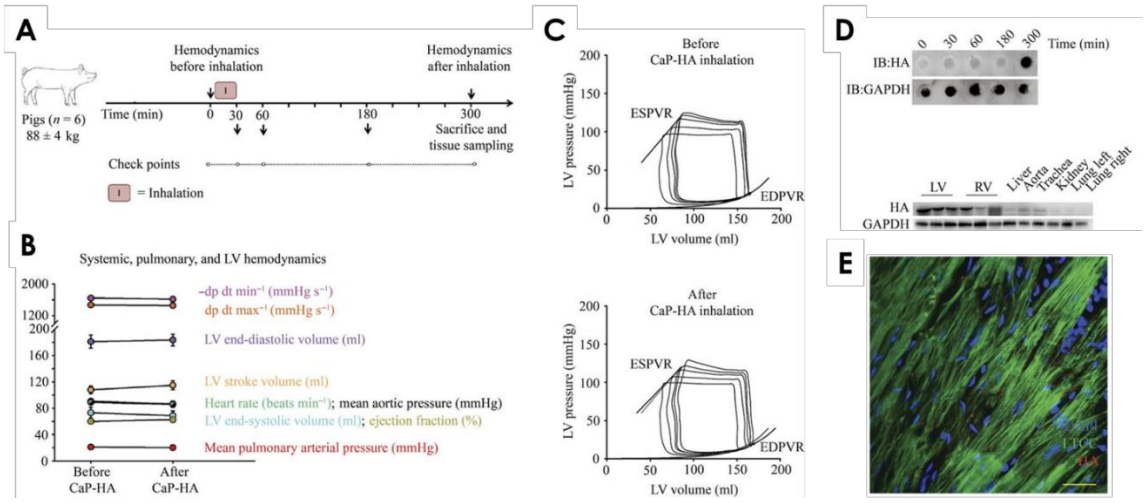

Figure 3.9. (A) Design of the study. (B) Systemic, pulmonary, and LV hemodynamics (n = 6; data are means ± SEM). Steady-state data before and after CaP inhalation were compared by one-way ANOVA for repeated measurements. Pressure-volume relationships were compared by analysis of covariance. Post hoc testing was performed by Tukey's test. $P < 0.05$ was considered significant. (C) Original registrations from one representative animal of LV pressure-volume loops before (pre, top) and after (post, bottom) CaP-HA inhalation. All registrations were recorded at spontaneous heart rate. ESPVR, end-systolic pressure-volume relationship; EDPVR, end-diastolic pressure-volume relationship. (D) Kinetics of inhaled CaP-HA cardiac targeting as examined by dot blot analysis from biopsies obtained at the indicated times after inhalation. IB, immunoblotting. (E) Western blot analysis for HA on tissues of treated pigs. (F) Z-stack confocal laser scanning microscopy images showing HA peptide in myocardial tissue from pigs treated by CaP-HA inhalation. Immunofluorescence staining for HA (red), LTCC (green), and cell nuclei (DAPI; blue). Scale bar, 20 µm (n = 6).

3.1.4 Conclusions

Here it is provided the proof of concept for an innovative and unconventional nanotechnological inhalation approach for cardiac delivery of peptides for the treatment of pathological heart conditions. Inhalation per se has long been established for the treatment of pulmonary diseases [33, 34], but its use for targeting of the heart and management of cardiac failing conditions has not previously been explored. It was demonstrated that inhalation of recently developed bioresorbable and negatively charged CaP NPs [21] allows for effective targeting to and treatment of the heart, resulting in higher, faster, and more selective cardiac accumulation of CaP NPs compared to other delivery routes, such as gavage, intraperitoneal, or intravenous. The delivery of drugs through CaP NPs-facilitated inhalation is thus likely to reduce the amount of required therapeutic compound, which, together with more cardiac-specific delivery, may minimize side effects compared to systemic delivery. Reduced first-pass metabolism may explain the more efficient delivery of CaP NPs to the heart by inhalation.

3.1.5 Future outcomes

The work presented in this sub-chapter identifies an inhalation-based approach for targeting the heart and may open up new avenues of investigation and potential uses of nanomaterials for the treatment of CVDs with therapeutic peptides. Inhalation therapy is easily administered and free from any physical or emotional burden associated with injection or other minimally invasive procedures, thus facilitating patient compliance, convenience, and home-based chronic treatment. A broader use of CaP NPs for carrying other drug/diagnostic compounds with different release kinetics (therapeutic polypharmacy) or even with different tissue targeting can be envisaged.

Although the feasibility for a novel therapeutic application is envisaged, it must be acknowledged that some limitations are still present. For instance, pathological conditions affecting the lungs such as chronic obstructive pulmonary disease might affect CaP NPs persistence and their translocation toward the pulmonary bloodstream, thereby limiting the efficiency of the targeted administration to the heart. In addition, the mechanistic events by which CaP NPs interact with and cross through the pulmonary barrier are still unknown and further efforts to understand these processes are necessary. Therefore, chronic administration and pharmacokinetic studies will be required to investigate the safety of this new delivery approach.

These necessary studies have prompted the creation of the EU H2020 RIA-funded project, called "CUPIDO – Cardiac Ultraefficient nanoParticles for Inhalation of Drug prOducts" (GA No. 720834), whose aim is to elucidate the fate of inhalable CaP NPs from the lung to the hearth and to develop a formulation to be tested in preclinical level.

3.2 Bibliography

1. Epple, M., *Review of potential health risks associated with nanoscopic calcium phosphate.* Acta biomaterialia, 2018. **77**: p. 1-14.
2. Iafisco, M., et al., *Cell surface receptor targeted biomimetic apatite nanocrystals for cancer therapy.* Small, 2013. **9**(22): p. 3834-3844.
3. Iafisco, M., et al., *Conjugation of hydroxyapatite nanocrystals with human immunoglobulin G for nanomedical applications.* Colloids and Surfaces B: Biointerfaces, 2012. **90**(0): p. 1-7.
4. Iafisco, M. and D. Catalucci, *Nano-apatites with designed chemistry and crystallinity for bone regeneration and nanomedical applications.* Bio-inspired regenerative medicine: materials, processes, and clinical applications. Singapore: Pan Stanford Publishing, 2016: p. 47-83.
5. Epple, M., et al., *Application of calcium phosphate nanoparticles in biomedicine.* Journal of Materials Chemistry, 2010. **20**(1): p. 18-23.
6. Mostaghaci, B., B. Loretz, and C.M. Lehr, *Calcium Phosphate System for Gene Delivery: Historical Background and Emerging Opportunities.* Current Pharmaceutical Design, 2016. **22**(11): p. 1529-1533.
7. Davis, M.E., et al., *Evidence of RNAi in humans from systemically administered siRNA via targeted nanoparticles.* Nature, 2010. **464**(7291): p. 1067.
8. Kim, B.Y., J.T. Rutka, and W.C. Chan, *Nanomedicine.* New England Journal of Medicine, 2010. **363**(25): p. 2434-2443.
9. Giardiello, M., et al., *Accelerated oral nanomedicine discovery from miniaturized screening to clinical production exemplified by paediatric HIV nanotherapies.* Nature communications, 2016. **7**: p. 13184.
10. Blanco, E., H. Shen, and M. Ferrari, *Principles of nanoparticle design for overcoming biological barriers to drug delivery.* Nature biotechnology, 2015. **33**(9): p. 941.
11. Zhao, Y., et al., *Augmenting drug–carrier compatibility improves tumour nanotherapy efficacy.* Nature communications, 2016. **7**: p. 11221.
12. Kuai, R., et al., *Designer vaccine nanodiscs for personalized cancer immunotherapy.* Nature materials, 2017. **16**(4): p. 489.
13. Weissig, V., T.K. Pettinger, and N. Murdock, *Nanopharmaceuticals (part 1): products on the market.* International Journal of Nanomedicine, 2014. **9**: p. 4357.
14. Ho, Y.T., B. Poinard, and J.C.Y. Kah, *Nanoparticle drug delivery systems and their use in cardiac tissue therapy.* Nanomedicine, 2016. **11**(6): p. 693-714.
15. Evans, C.W., K.S. Iyer, and L.C. Hool, *The potential for nanotechnology to improve delivery of therapy to the acute ischemic heart.* Nanomedicine, 2016. **11**(7): p. 817-832.
16. S Behera, S., K. Pramanik, and M. K Nayak, *Recent advancement in the treatment of cardiovascular diseases: Conventional therapy to nanotechnology.* Current Pharmaceutical Design, 2015. **21**(30): p. 4479-4497.

17. Mendis, S., S. Davis, and B. Norrving, *Organizational update: the world health organization global status report on noncommunicable diseases 2014; one more landmark step in the combat against stroke and vascular disease.* Stroke, 2015. **46**(5): p. e121-e122.
18. Suarez, S., A. Almutairi, and K. Christman, *Micro-and nanoparticles for treating cardiovascular disease.* Biomaterials science, 2015. **3**(4): p. 564-580.
19. Fosgerau, K. and T. Hoffmann, *Peptide therapeutics: current status and future directions.* Drug discovery today, 2015. **20**(1): p. 122-128.
20. Uhlig, T., et al., *The emergence of peptides in the pharmaceutical business: From exploration to exploitation.* EuPA Open Proteomics, 2014. **4**: p. 58-69.
21. Di Mauro, V., et al., *Bioinspired negatively charged calcium phosphate nanocarriers for cardiac delivery of MicroRNAs.* Nanomedicine, 2016. **11**(8): p. 891-906.
22. Savi, M., et al., *Titanium dioxide nanoparticles promote arrhythmias via a direct interaction with rat cardiac tissue.* Particle and fibre toxicology, 2014. **11**(1): p. 63.
23. Mills, N.L., et al., *Adverse cardiovascular effects of air pollution.* Nature Reviews Cardiology, 2009. **6**(1): p. 36.
24. Miragoli, M., et al., *Functional interaction between charged nanoparticles and cardiac tissue: a new paradigm for cardiac arrhythmia?* Nanomedicine, 2013. **8**(5): p. 725-737.
25. Rusconi, F., et al., *Peptidomimetic targeting of Cavβ2 overcomes dysregulation of the L-type calcium channel density and recovers cardiac function.* Circulation, 2016. **134**(7): p. 534-546.
26. Alogna, A., et al., *Inotropic effects of experimental hyperthermia and hypothermia on left ventricular function in pigs—Comparison with dobutamine.* Critical care medicine, 2016. **44**(3): p. e158-e167.
27. Bakand, S., A. Hayes, and F. Dechsakulthorn, *Nanoparticles: a review of particle toxicology following inhalation exposure.* Inhalation toxicology, 2012. **24**(2): p. 125-135.
28. De Jong, W.H. and P.J. Borm, *Drug delivery and nanoparticles: applications and hazards.* International Journal of Nanomedicine, 2008. **3**(2): p. 133.
29. Roberts, J.R., et al., *Pulmonary and cardiovascular responses of rats to inhalation of silver nanoparticles.* Journal of Toxicology and Environmental Health, Part A, 2013. **76**(11): p. 651-668.
30. Petrick, L., et al., *Silicon dioxide nanoparticles increase macrophage atherogenicity: stimulation of cellular cytotoxicity, oxidative stress, and triglycerides accumulation.* Environmental toxicology, 2016. **31**(6): p. 713-723.
31. Lin, K., C. Wu, and J. Chang, *Advances in synthesis of calcium phosphate crystals with controlled size and shape.* Acta biomaterialia, 2014. **10**(10): p. 4071-4102.
32. Kozlowski, L.P., *IPC–isoelectric point calculator.* Biology direct, 2016. **11**(1): p. 55.
33. Irngartinger, M., et al., *Pulmonary delivery of therapeutic peptides via dry powder inhalation: effects of micronisation and manufacturing.* European Journal of Pharmaceutics and Biopharmaceutics, 2004. **58**(1): p. 7-14.
34. Patton, J.S., C.S. Fishburn, and J.G. Weers, *The lungs as a portal of entry for systemic drug delivery.* Proceedings of the American Thoracic Society, 2004. **1**(4): p. 338-344.

Chapter 4. Calcium phosphate nanoparticles for dental remineralization

Despite the remarkable advances in oral care technology, demineralization of dental hard tissues (enamel and dentin) is still a growing issue and the main responsible for dental caries and dentin hypersensitivity [1]. It is caused by a low pH environment which, in turn, is the consequence of the intake of acidic food or drinks, the presence of gastroesophageal reflux disease (GERD) and/or the acidogenic activity of a pathogenic oral biofilm [2]. When the pH of the saliva drops below 5.5 HA, representing 95 wt% and 75 wt% of enamel and dentinal tissue respectively, starts to dissolve [3, 4].

Demineralization is a reversible process if the damaged tissues are exposed to oral environment that favors remineralization. For example, the enamel cavities caused by demineralization processes are naturally remineralized by the epitaxial growth of residual crystals acting as nucleation sites, while saliva provides a supersaturated Ca^{2+} and PO_4^{3-} ions environment respect to HA [1, 5]. However, remineralization of enamel by saliva is seldom completely achieved, especially when there is an imbalance in duration and extent of demineralization/remineralization phases [1].
Therefore, to efficiently hinder demineralization and boost remineralization, it is required the use of an external source of Ca^{2+} and PO_4^{3-} ions to increase the supersaturation of HA and induce the mineral precipitation and to likely close the crystal lesions and voids [5]. It can be also achieved with the use of materials chemically similar to those present in the dental tissue which could promote the natural repair of the damaged tissues [2].

Various form of biomimetic calcium phosphates mimicking the mineral phase of bone and tooth such as HA, FHA, and ACP have been proposed for dental hard tissue remineralization [3-7]. These agents can be added to restorative materials or directly applied on the tooth surface [5]. It has been demonstrated that CaP NPs are more efficient for remineralization therapies in comparison to their macro-sized counterparts due to their biomimetism, higher surface area and reactivity as well as better ability to adhere and penetrate into the enamel and dentinal lesions [8, 9].

Part of the content of this chapter has been published in Scientific reports 2018, 8(1), 17016 as "*Iafisco, M., Degli Esposti, L., Ramírez-Rodríguez, G. B., Carella, F., Gómez-Morales, J., Ionescu, A. C., Brambilla, E., Tampieri, A., Delgado-López, J. M. Fluoride-doped amorphous calcium phosphate nanoparticles as a promising biomimetic material for dental remineralization*".

In this chapter will be reported the research work on the functional by design development of biomimetic CaP NPs for dental remineralization. The aim of the works was to produce CaP NPs that are able to provide a highly supersaturated local environment on the teeth and stimulate hard tissues remineralization, focusing on the use of amorphous CaP NPs for this purpose. In detail, subchapter 4.1 will focus on the development of biomimetic ACP nanoparticles and fluoride-doped ACP (FACP) nanoparticles for enamel remineralization and dentin desensibilization. Subchapter 4.2 will focus on the development of magnesium and strontium doped FACP nanoparticles with the aim of superior performance in enamel restoration.

4.1 Amorphous calcium phosphate nanoparticles for dental remineralization

4.1.1 Introduction

Among CaP NPs, ACP nanoparticles are particularly appealing in dentistry due to their ability to release a significant amount of Ca^{2+} and PO_4^{3-} ions, as compared with other crystalline CaP phases. ACP is a mineral phase with a short- and medium- range order, and its basic structural unit, as proposed by Betts and Posner, is a roughly spherical cluster of ions having an average diameter of 0.95 nm consistent with the chemical composition $Ca_9(PO_4)_6$ [10, 11]. It is an unstable material that rapidly transforms into the more thermodynamically stable CaP phases (i.e., HA or OCP) in solution or in dry state by reacting with atmospheric water [12]. ACP is a precursor (transient) phase of biogenic HA of bone and tooth [6, 9, 13, 14]. Indeed, it was demonstrated by Robinson *et al.* that the formation of enamel occurs through the deposition of spherical ACP nanoparticles into chains, being subsequently transformed into HA [15].

Thanks to its excellent bioactivity, high cell adhesion, tailorable biodegradation and good osteoconductivity ACP is not only studied for dental applications but it is currently employed to manufacture several biomaterials for bone repair [16, 17]. It is used, for example, in the preparation of coatings on metallic prostheses, self-setting injectable cements and hybrid composites when mixed with polymers [14, 16, 17].

Since ACP can readily convert to crystalline phases, its use and handling is difficult. Therefore, several additives and ions were studied to stabilize ACP, including casein phosphopeptides (CPP) [18], carboxymethyl chitosan (CMC) [19, 20], polyethylene glycol [21], polyaspartic acid [22], adenosine triphosphate (ATP) [23], magnesium ions [24], and poly(ethylene glycol)-block-polylactide (PEG-PLA) [25]. To our knowledge, most of these materials are not available on the market due to difficulties in the scale up process, and to costs and concerns on the biocompatibility of the stabilizing agents. Only CPP-stabilized ACP (CPP-ACP) is actually marketed for enamel remineralization in a formulation that is directly applied on tooth surface (i.e. tooth mousse), having a good level of literature evidence for this use (systematic reviews) [2, 26]. Additionally, CPP-ACP is employed as an effective dentin desensitizer, where its action is to fill and occlude dentinal tubules [27, 28]. The hypersensitivity deriving from open dentinal tubules is indeed one of the worst

consequences of exposed dentinal demineralization [28]. However, CPP is a milk-derived protein and it cannot be used by patients having intolerance to milk [29].

Fluoride is the most employed prophylactic agent to reduce and prevent enamel demineralization, remaining so far as the most effective agent for caries prevention [30]. It is considered to act by two different mechanisms [31, 32]: i) replacing of the hydroxyl groups of the new formed HA, resulting in FHA, which is less soluble and thus more resistant to low pH values than HA [32]; ii) inhibiting the metabolic and physiological pathways of microorganisms in the cariogenic biofilm that produce organic acids to demineralize dental tissue [32]. In addition to that, an inverse relationship can be found between the concentration of Ca^{2+} in oral biofilms and dental caries risk, therefore several Ca^{2+}-containing compounds were introduced in oral care products and dental materials to promote remineralization [33]. These compounds have exhibited a relevant effect on oral biofilms, especially depending on the composition and surface characteristics of the material itself [9, 34].

The aim of this work was the preparation of new forms of biomimetic ACP nanoparticles, using citrate and carbonate ions, which being important components of enamel and dentin, enhance their similarity with biogenic mineral phase of tooth. These particles can play a dual role in preventive dentistry: i) occlusion of the dentinal tubules due to their nano-dimensions and ii) delivery Ca^{2+}, PO_4^{3-} directly on hard tissue surfaces, generating a local supersaturation that triggers the remineralization of dental hard tissues. Moreover, we have explored the possibility of incorporating fluoride ions in the ACP nanoparticles (FACP) without affecting their amorphous nature in order to generate materials with potentially enhanced anti-caries and remineralizing properties. Indeed, the topical delivery of fluoride mediated by ACP nanoparticles directly in the dental cavities/lesions, could enhance its efficacy and reduce side effects. Actually, the overconsumption of fluoride through fluoridated water/foods and supplements may lead to dental or skeletal fluorosis [35].

4.1.2 Sample preparation and characterization

Sample preparation

ACP nanoparticles were synthesized by abrupt mixing of two solutions (1:1 v/v, 200 mL total) consisting of (i) 100 mM calcium chloride + 400 mM Na_3Cit and (ii) 120 mM sodium hydrogen phosphate + 200 mM sodium carbonate. The pH of the mixture was adjusted to 8.5 with concentrated HCl. When the precipitation occurs (approximately 30 seconds after mixing), the nanoparticles were washed with ultrapure water by centrifugation (5000 RPM, 15 min, 4 °C) three times and then freeze-dried overnight at -50 °C under a vacuum of 3 mbar. Since the initial Cit/Ca molar ratio is 4, the samples is nominated ACP-4. FACP-4 samples were prepared similarly to ACP-4, but with the addition of NaF 5 mM (low) or 50 mM (high) to solution (ii) (referred to as FACP-l4 and FACP-h4, respectively). Samples of ACP and FACP were also prepared by decreasing the initial Cit/Ca molar ratio to 2 and 1 (referred to as ACP-2, FACP-h2 and ACP-1, FACP-h1, respectively).

Physical-chemical characterizations

Samples were characterized by PXRD, TEM, chemical composition analyses, FT-IR and Raman spectroscopy, SSA, porosity and TGA. Interpretation of the four TGA weight losses were attributed to adsorbed water (from room temperature to 150 °C), structural water (from 150 to 350 °C), citrate (from 350 to 700 °C) and carbonate (from 700 to 1000 °C).

Ion release in acidic artificial saliva

200 mg of ACP or FHA dry powder was dispersed into 10 mL of artificial saliva prepared as modified Tani-Zucchi solution [36, 37] containing KCl 20 mM, KSCN 5.3 mM, Na_2HPO_4 1.4 mM, $NaHCO_3$ 15 mM, and lactic acid 10 mM. The suspension was maintained at 37 °C under shaking. At scheduled times (30 minutes, 1 hour, 2 hours) the suspension was centrifuged at 5000 RPM for 15 min, and 8 mL of the supernatant was removed for Ca^{2+} and F^- quantification by ICP-OES and fluoride selective ISE, respectively. After that, samples were rinsed with 8 mL of fresh artificial saliva and the suspension was again put under shacking at 37 °C until the next time point.

ACP crystallization time evaluation

Time-dependent Raman spectra of ACP-to-HA conversion were collected on ACP and FACP samples in contact with water. ACP or FACP aqueous suspensions were drop-cast between a glass slide and a glass slip that were carefully sealed with vacuum grease in order to prevent evaporation during the spectra collection. Spectra were collected as described in Raman spectroscopy paragraph of Chapter 2.

***In vitro* remineralization and dentinal tubules occlusion test**

The *in vitro* remineralization and dentinal tubules occlusion test illustrated in this sub-chapter of Ph.D thesis were carried out in collaboration with the Oral Microbiology Laboratory of Galeazzi Orthopedic Institute, Department of Biomedical, Surgical and Dental sciences, University of Milan (Dr. Andrei C. Ionescu and Dr. Eugenio Brambilla). Five sound human molar teeth extracted for clinical reasons were sectioned horizontally under water cooling in order to expose both enamel and dentin, and subsequently four regions were delimited in each sample with a bur-made cross incision. After that, specimens were polished and the enamel and the dentin were etched with concentrated H_3PO_4 (37 wt. %) for 30 seconds, followed by extensive rinsing with ultrapure water. *In vitro* experiments were performed treating the sample regions with a 50 wt% aqueous slurry of ACP or FACP powders for 24h, in a 100% humidity atmosphere. Afterwards, the samples were washed for 1 min under running tap water and dried. Samples regions were treated with ACP-4, FACP-h4, ACP-1 and FACP-h1; one part of each specimen was not treated and acted as control.

Specimens were then subjected to critical point drying (Critical-Point Dryer, EMS 850, Hatfield, PA, USA), mounted on stubs with conductive tape, sputter coated (JEOL FFC-1100, Tokyo, Japan), and observed with SEM (Jeol JSM 840A, Tokyo, Japan) at 15 KV acceleration voltage.

4.1.3 Results and discussion

Characterization of ACP and FACP

The main goal of the research was to produce ACP nanoparticles that (i) are stable as amorphous material at room for a long storage time and (ii) to remineralize the dental hard tissues.

Regarding the first objective, TEM micrographs of all ACP and FACP samples (Figure 4.1A-B) show that the products were composed by round shaped nanoparticles, with sizes ranging between 20 and 50 nm, thus confirming their nanostructured nature. All the samples were amorphous, as evinced by the diffuse broad rings of the TEM SAED patterns and the broad, unresolved band centered at about 30° (2θ) in the XRD pattern (Figure 4.1C). These data confirm the lack of long-range periodicity in the materials and thus excludes the presence of any crystalline phases. The stability of ACP and FACP to remain amorphous when stored at room temperature as dry powder up to eighteen months has been evaluated by reanalyzing their XRD pattern at several time points. At all the time points the XRD diffractograms remained unchanged, establishing that the amorphous nature was preserved during this period of time (Figure 4.1D). This long-term stability in dry state is ascribed to the presence of citrate ions, which has been previously proposed to play an important role in stabilizing the amorphous precursor of biogenic HA [38-40]. On the other hand, it is well reported in literature that unstabilized ACP converts spontaneously into a crystalline phase in a matter of hours [17].

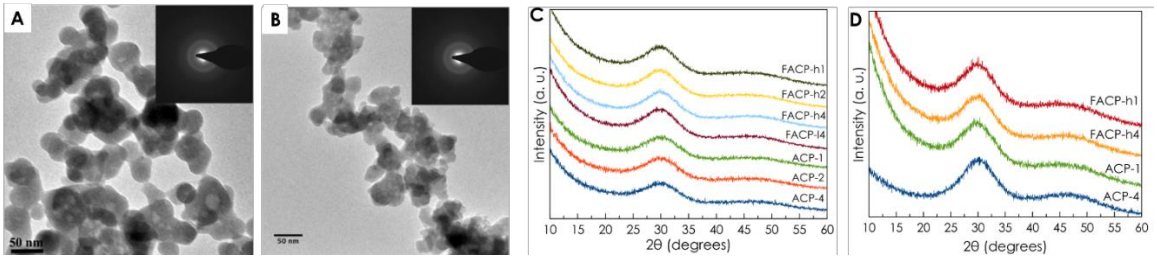

Figure 4.1 (A) TEM micrograph of ACP-4. Inset: SAED pattern. (B) TEM micrograph of FACP-h4. Inset: SAED pattern. (C) PXRD pattern of the samples. (D) PXRD of selected ACP and FACP samples after 18 month of storage.

This result was even more remarkable for FACP samples (Figure 4.1D), since it is well reported that fluoride ion favors the formation of the more thermodynamically stable FHA and thus could prevent the formation of an amorphous phase [41]. Indeed, to the best of our knowledge, the synthesis of stable fluoride-doped ACP has not been reported so far. The data allow us to conclude that with our synthesis procedure adding F^- ions to the reactant solution did not cause the precipitation of fluoride salts or other crystalline CaP phases, as otherwise previously reported in the absence of citrate [16, 41].

The FT-IR spectra of the samples displays broad, unresolved bands characteristic of ACP (Figure 4.2A). In particular, the absorption bands at ca. 560 and 1050 cm^{-1} are associated to the bending and stretching modes of phosphate groups, respectively. The bands at ca. 870 cm^{-1} and in the range 1400–1500 cm^{-1} are attributed to the carbonate ions included in the amorphous material, while the band at ca. 1600 cm^{-1} can be assigned the stretching of $-COO^-$ of citrate (superimposed to water bending band at 1640 cm^{-1}), confirming the presence of this molecule onto ACP even after extensive washing. The presence of structural water in ACP and FACP samples was denoted by the presence broad bands at 1640 cm^{-1} and in the 3000 – 3600 cm^{-1} range (not shown), as well as by TGA weight losses at low temperature.

Chemical composition and specific surface area (SSA_{BET}) of ACP and FACP samples, obtained by the means of ICP-OES, TGA, and fluorine-selective ISE are reported in table 4.1. All ACP samples have similar chemical composition, and in FACP samples is confirmed the incorporation of F^- into the ACP nanoparticles. The amount of incorporated fluorine increases linearly with the initial F^- precursor concentration, being ten times higher in FACP-h4 with respect to FACP-l4. Fluorine incorporation leads to an increase of the calcium content, and thus a higher Ca/P ratio, which is likely a consequence of the neutralization of the negative density charge of fluoride ions. Indeed, the increase in Ca/P ratio was observed only a relatively high content of F^- is incorporated (FACP-h4), but not when the F content is low (FACP-l4). Our data does not give any indication on the location of F^- ions in FACP structure, that could be incorporated in the short- and medium-range order of ACP (thus forming an “outer ionic layer” of Posner’s cluster) of by taking part of ultrasmall crystalline fluorapatite nanoclusters. On this topic further works on local order (e.g. fluorine solid state NMR, pair distribution function studies) are needed. TGA losses confirm the presence of carbonate and citrate ions in ACP and FACP, with content that is constant for all the samples (Figure 4.2B). The value of SSA_{BET} was in line with the nano-dimensions detected by TEM but remarkably higher than that of other type of ACP nanoparticles previously described [42, 43].

While the morphological, structural and compositional features as well as long-term stability in dry state are practically independent of the initial Cit/Ca ratio, the SSA_{BET} is the only value clearly affected. The trend is that SSA_{BET} increases when Cit/Ca ratio decreases. The SSA_{BET} value of ACP-1 is notably high (328 $m^2 g^{-1}$) and, to the best of our knowledge, such high value has never been reported for CaP based materials. Since (F)ACP-1/2/4 samples are similar in size and morphology, this increase in SSA_{BET} could be due to differences in porosity. Mercury intrusion porosity analyses on ACP-4 and ACP-1 revealed that the latter has a higher porosity (92.52% vs 84.19%) (Figure 4.2C). The pore size distribution shows that both samples possess macro- and mesopores of about 35 µm and 55 nm in diameter for ACP-4 and of about 20 µm and 20 nm for ACP-1. Moreover, the mesopores of ACP-1 constitute a higher percentage of the total porosity compared to ACP-4. These differences in porosity could explain the increase in SSA_{BET} observed for ACP-1.

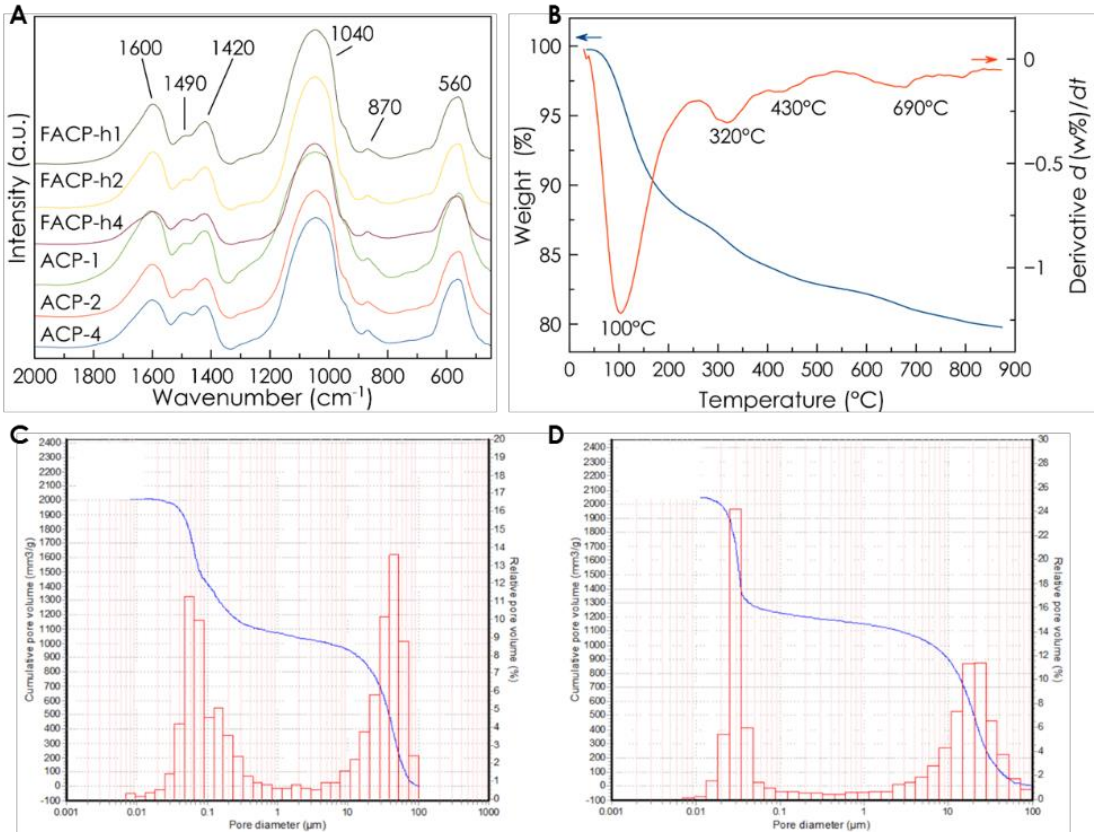

Figure 4.2. (A) FTIR spectra of the samples. (B) TGA curve and DTG curve for ACP-4 sample. (C) Pore size distribution histogram for ACP-4. (D) Pore size distribution histogram for ACP-1.

Table 4.1. Chemical composition and specific surface area (SSA_{BET}) of the powder samples

Sample	Ca (wt%)[a]	P (wt%)[a]	Ca/P (mol)[a]	F (wt%)[b]	Citrate (wt%)[c]	Carbonate (wt%)[c]	SSA(m^2 g^{-1})[d]
ACP-4	29.9±0.7	13.6±0.3	1.70±0.02	-	1.9±0.2	3.7±0.4	200±20
FACP-l4	31.6±0.7	14.4±0.3	1.70±0.01	0.10±0.01	2.2±0.2	3.2±0.3	255±26
FACP-h4	31.4±0.4	13.6±0.2	1.78±0.01	1.00±0.10	1.5±0.2	3.8±0.4	213±21
ACP-2	29.1±1.0	13.2±0.3	1.70±0.02	-	2.2±0.2	3.8±0.4	287±29
FACP-h2	32.1±0.5	13.1±0.2	1.89±0.01	1.10±0.10	2.0±0.2	3.4±0.3	328±33
ACP-1	28.0±0.6	12.7±0.2	1.70±0.04	-	1.8±0.2	3.2±0.3	309±31
FACP-h1	31.9±0.8	13.1±0.3	1.88±0.01	1.30±0.10	2.4±0.2	3.1±0.3	293±29

[a]Quantified by ICP-OES; [b]Quantified by fluoride ion electrode; [c]Quantified by TGA; [d]Calculated from BET adsorption.

(F)ACP crystallization and ion release capability

Regarding the application of ACP for teeth remineralization agent it must be taken into account that ACP-based remineralization is based on two principles: (i) gradual release of Ca^{2+} and PO_4^{3-} ions generating a local supersaturation that triggers the remineralization of hard tissues and (ii) attachment to the surface of the hard tissues, being then transformed to HA. Therefore, we have evaluated in vitro the capabilities of the ACP and F-ACP samples in inducing both effects.

Raman spectra of dry ACP-2 and FACP-h2 are shown in Figure 4.3A. They exhibit the characteristics Raman peaks of phosphate vibrations of ACP along with the υ_1CO (carbonate) and δCOO (citrate) vibrational modes [38]. Concretely, the main peak, due to the ν_1PO_4 vibration, appears at ca. 952 cm^{-1}, in agreement with the amorphous nature of the nanoparticles. On the contrary, this peak appears at ca. 958 cm^{-1} for nanocrystalline HA [38] and 962 cm^{-1} for nanocrystalline FHA [44]. Therefore, the blue-shift from 952 to 958/960 can be used to monitor the conversion from (F)ACP to (F)HA in aqueous media [38].

Time-dependent *in situ* Raman spectra (ν_1 PO_4 region) of ACP-2 and FACP-2 in water are shown in Figure 4.3B and 4.3C, respectively. A peak upshift from 950 cm^{-1} to ca. 958 cm^{-1} (HA) and 960 cm^{-1} (FHA) is clearly visible, indicating the existence of a gradual transformation from (F)ACP to (F)HA, respectively. The normalized ratio of the corresponding ν_1PO_4 Raman band of (F)HA and ACP (i.e., A_{960}/A_{950}) was used to study the extent of the conversion (Figure 4.3D). As expected, we found that F-doping resulted in a much faster (F)ACP-(F)HA conversion. The FACP-h2 sample was

transformed into FHA after 18 hours, while the ACP-2 sample required around 32 hours to be completely transformed into HA (Figure 4.3D). The conversion kinetic of ACP-4 was previously reported [38]. The comparison of ACP-4 and ACP-2 turns out that increasing the citrate concentration ends up in a slower conversion, since ACP-4 is transformed after 54 hours.

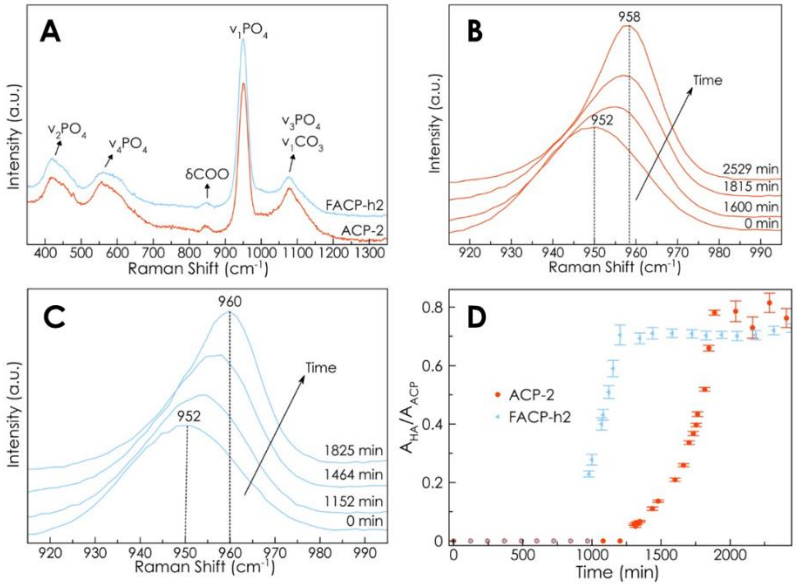

Figure 4.3. (A) Raman spectra of ACP-2 (red) and FACP-h2 (blue). *In situ* time-dependent Raman spectra (ν_1PO_4 vibrations) collected during the transformation of (B) ACP-2 and (C) FACP-h2 to HA and FHA, respectively, in water. (D) Time-dependent intensity ratio of the ν_1PO_4 peak of ACP-2/ FACP-h2 (952 cm^{-1}) and HA/FHA (959 cm^{-1}).

The ions (Ca^{2+} and F^-) release has been evaluated in vitro in acidified artificial saliva, an organic-free solution that mimics the composition of human saliva after eating (Figure 4.4). (F)ACP samples show a gradual and progressive release of Ca^{2+} and F^- ions. Comparatively, the Ca^{2+} and F^- release from a sample of crystalline FHA – a material that is commonly used as tooth treatment products – is negligible under the same conditions, which confirms the high efficiency of (F)ACP for the gradual release of Ca^{2+} and F^- ions. The samples prepared with a lower Cit/Ca ratio provided higher ion release rates probably due to their higher SSA. In fact, all the samples with similar surface area (i.e. ACP-2, ACP-1, FACP-h2 and FACP-h1) present comparable Ca^{2+} and F^- release kinetic.

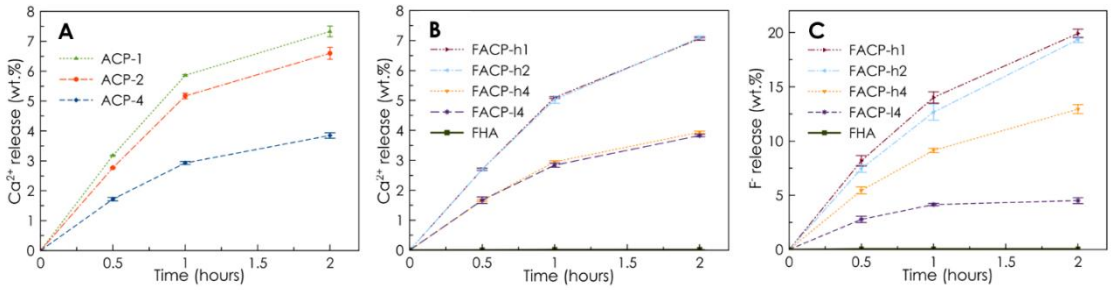

Figure 4.4. Cumulative Ca^{2+} ions release from (A) ACP samples and (B) FACP samples. (C) Cumulative F^- ions release from F-ACP samples. The cumulative release of Ca and F from crystalline FHA is also shown in (B) and (C), respectively.

In vitro remineralization effect of (F)ACP

Since (F)ACP samples have proven to possess the feasibility of remineralize enamel, we have tested in vitro the effect of ACP-4/1 and FACP-h4/1 samples as remineralization materials, evaluating their potential application for dentinal tubules occlusion and enamel remineralization. Samples of human enamel and dentin were etched with H_3PO_4 simulating an early enamel/dentine lesion, and subsequently treated with concentrated slurries of ACP and FACP for 24h.

ACP and FACP samples showed good behavior on occluding dentinal tubules, as seen in Figure 4.5. Specifically, ACP samples displayed a better activity providing a higher degree of occlusion than FACP (Figure 4.5B-E). According to *in situ* Raman observations, ACP is still stable after 24 hours in water, while FACP has been completely converted into FHA. The higher stability of ACP in water could explain its better activity in occluding the tubules. The faster transformation occurring in the FACP sample could marginally hinder the penetration in the tubules at 24h. This is especially evident in the dentin treated with FACP-h1 (Figure 4.5E-J) which showed the poorest occluding effect and the highest presence of crystalline micro-particles. It must be highlighted, nevertheless, that all samples showed a relevant occluding effect.

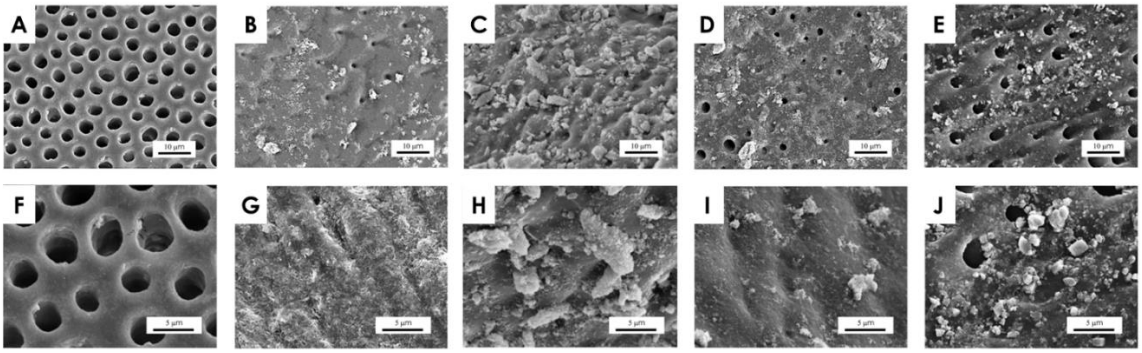

Figure 4.5. SEM micrographs of (A, F) demineralized dentin and demineralized dentin treated with (B, G) ACP-4, (C, H) FACP-h4, (D, I) ACP-1, and (E, J) FACP-h1 at two different magnifications.

Regarding the enamel remineralization effect, some nano- or microcrystals of HA growing onto the ordered microcrystals of enamel prisms are clearly visible (Figure 4.6). The newly deposited crystals are less ordered than the native ones, but it is remarkable that they form a layer of enamel-like crystals, mimicking those of the biological sample which acts as substrate. In this sense, the remaining microstructures of the dental tissue may have acted as a remineralization guide possibly meaning that remineralization of damaged tissues may achieve better performances if residual microstructures of the tissue are not altered. This implies that ACP and FACP are suitable for enamel remineralization, and interestingly it also means that the compounds showed biomimetic activity, since they were able to restore enamel in its native structure. This is a notable advantage over other materials that only act as fillers of demineralized regions without any regeneration effect [13]. It is worth mentioning that the interprismatic regions seems to be restored and less hollowed with the ACP samples (Figure 4.6B, D) probably ACP displayed a remineralization and regenerative effect similar to what has been observed at lower magnification on dentine. This effect is particularly interesting since the interprismatic regions, being less crystalline, are the ones more subjected to acidic erosion [45, 46]. On the other hand, FACP samples showed an enhanced remineralization effect on prismatic enamel (Figure 4.6C, E). It may be argued that the quickly formed FHA crystals tend to adhere and grow on highly crystalline prismatic regions. Further studies may investigate the effect of this remineralizing technology when associated with a scaffold technology that may mediate ions release over an extended amount of time. Moreover, future analysis on the effect of F ions delivered by ACP compared to free F ions on the resistance of enamel to low pH will be carried out.

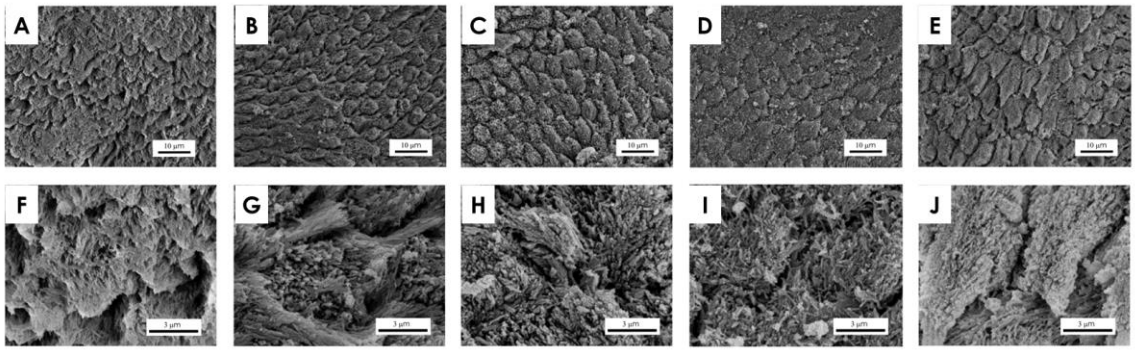

Figure 4.6. SEM micrographs of (A, F) demineralized enamel and demineralized enamel treated with (B, G) ACP-4, (C, H) FACP-h4, (D, I) ACP-1, and (E, J) FACP-h1 at two different magnifications

4.1.4 Conclusion

Innovative biomimetic ACP and FACP nanoparticles (with tunable F^- contents), acting as promising dentin desensitizer and remineralizing agent in preventive dentistry have been produced using a straightforward and scalable synthetic route. The presence of citrate makes them stable in dry state at least up to one year. Reducing the Cit/Ca molar ratio of the reactants from 4 to 2 (or 1), the specific surface area significantly increases, leading to particles with faster Ca^{2+} and F^- release kinetics and conversion into HA. Significantly, the presence of fluoride did not induce any significant change in the chemical-physical features of ACP, apart from the more rapid conversion in the crystalline phase when immersed in aqueous solution. As proof of concepts, the efficacy of the ACP and FACP samples for enamel remineralization and occlusion of dentinal tubules has been tested *in vitro*. All the samples showed good ability to partly occlude the tubules after 24 h of contact with acid-etched dentin samples. ACP samples displayed a faster activity compared to FACP due to their slower conversion kinetic to HA revealing an optimal agent in the case of severe dentinal hypersensitivity. ACP and FACP are able to remineralize enamel showing biomimetic activity, since they were able to restore enamel in its native structure mimicking the process of biomineralization. In particular, FACP samples showed a faster remineralization effect compared to ACP on prismatic enamel thus being suitable for patients exhibiting severe enamel demineralization. Overall, these results indicate the employment of fluoride and citrate allow to tune specific properties of the final material for the management of specific needs of the patient.

4.1.5 Future outcomes

The data reported therein have given the prove that (F)ACP is potentially an excellent material for dental remineralization, and open the doors to future clinical studies that will allow to better validate the therapeutic value of ACP and FACP. The next steps that will be made in the future are to validate the properties of the material (i) as toothpaste formulation, and (ii) to validate it *in vivo*.

4.2 Multi-ion doped amorphous calcium phosphate nanoparticles

4.2.1 Introduction

It has been proved that biogenic HA is non-stoichiometric and is doped with several foreign ions, i.e. CO_3^{2-}, Na^+, Mg^{2+}, Cl^-, K^+, F^-, and Sr^{2+}. The amount of these foreign ions in biological HA is highly variable and depends on several factors, e.g. the nature of the mineralized tissue, age, diet, and environmental factors [47-49]. This variability in composition is due to the highly flexible crystal structure of HA, that can accommodate ions of several sizes through substitution mechanism with Ca^{2+}, PO_4^{3-} and OH^- ions while still maintaining its intrinsic structure. The research on doping of synthetic apatites has proved that ionic doping can impart HA peculiar functionalities (such as luminescence, magnetism, hyperthermia), or can activate specific processes improving the materials performances when in contact with the biological environment (osteointegration, osteoinduction, anti-bacterial) [50, 51].

Regarding synthetic CaPs targeted to remineralize dental enamel, the three most interesting doping ions are F^-, Mg^{2+}, and Sr^{2+}. Fluoride doping has already been discussed in section 4.1.1 and it is the most known and used ionic dopant in the dental field.

Strontium is believed to be another ion with remineralizing properties. Epidemiological studies have suggested a cariostatic effect of Sr since it was observed an inverse correlation between the content of Sr^{2+} in drinkable waters and caries incidence [52]. More recent works have proven that Sr^{2+} ions have a synergistic remineralizing effect when used in combination with F^- ions [53, 54]. However, the reason of this synergy is still not clear. It has been proposed the HA doped with Sr^{2+}, F^- and CO_3^{2-} ions is more crystalline than HA and thus is more resistant to acidic degradation [55]. Apart from remineralizing properties, Sr-substituted HA has been proved to be an antibacterial nanomaterial [56, 57], even if also in this case the reason of antibacterial effect has not been elucidated yet. At the same time some works claim that Sr-substituted HA has higher cell viability than pure HA [58].

Magnesium is an ion that occurs naturally in human enamel and dentin, whose concentration varies with tooth depth [59]. Mg-doped HA, however, is more soluble than HA due to the destabilizing effect of magnesium ion that distorts the HA crystal lattice and decreases HA crystallinity [59-61]. Therefore, the Mg-rich regions of teeth are more prone to acidic degradation and Mg is easily lost from dental tissue [59, 62]. For this reason there is the need provide a local supply of Mg^{2+} ions to the dental surface in order to restore the natural magnesium content.

Therefore, the aim of this work was the improvement of the properties of biomimetic FACP nanoparticles described in subchapter 4.1 by doping with Mg^{2+} and Sr^{2+} ions. We have explored the possibility of incorporating magnesium and strontium ions singularly (referred as doping) and simultaneously (referred as co-doping) in FACP nanoparticles (Mg,Sr-FACP). The objective was to obtain a product with the same remineralizing properties of FACP that possess the ability to restore the depleted Mg of biological enamel and exerting the beneficial remineralizing and antibacterial effects of Sr.

4.2.2 Sample preparation and characterization

Mg,Sr-FACP-4 nanoparticles were synthesized as reported for FACP-h4 nanoparticles in paragraph 4.1.2, but with the addition of $MgCl_2$ or $SrCl_2$ in solution (i). In detail, magnesium doping was achieved by using $MgCl_2$ 10 mM, 20 mM or 40 mM to achieve a theoretical doping of 1 wt.%, 2 wt.%, or 5 wt.%, (referred as 1Mg-FACP-4, 2Mg-FACP-4, and 5Mg-FACP-4 respectively). Strontium doping was achieved by using $SrCl_2$ 0,5 mM, 2,6 mM or 5 mM to achieve the same theoretical doping (referred as 1Sr-FACP-4, 2Sr-FACP-4, and 5Sr-FACP-4 respectively). Co-doping was made by using both $MgCl_2$ and $SrCl_2$ at the same time at the concentration stated above (referred as (1,2,5)MgSr-FACP-4).

Samples of Mg,Sr-FACP were also prepared by decreasing the initial Cit/Ca molar ratio to 2 and 1 while keeping the Mg or Sr doping level to maximum (referred as 5Mg-FACP-2, 5Sr-FACP-2, 5MgSr-FACP-2, 5Mg-FACP-1, 5Sr-FACP-1, and 5MgSr-FACP-1 respectively).

Physical-chemical characterizations

Samples were characterized as reported in paragraph 4.1.2. Furthermore, the ion release in acidic artificial saliva was performed as reported in paragraph 4.1.2.

4.2.3 Results and discussion

Characterization of Mg,Sr-FACP-4 at different doping levels

The main goal of the research was to add the biologically relevant Mg and Sr ions into FACP without altering FACP remineralization properties. The PXRD and FT-IR spectra of the doped and co-doped samples with Cit/Ca ratio of 4 (Figure 4.7) confirm that all the products have an amorphous nature independently from doping level, as evinced by the presence of only a broad band at about 30° 2θ in the PXRD pattern and broad, unresolved bands in the IR spectra.

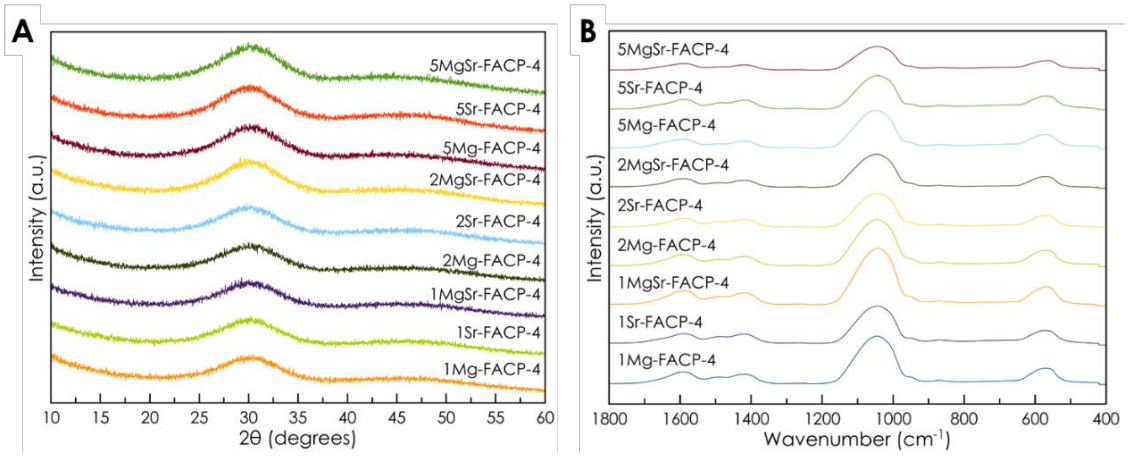

Figure 4.7. (A) PXRD patterns of the Mg,Sr-FACP-4 samples. (B) FTIR spectra of the Mg,Sr-FACP-4 samples.

Chemical composition of MgSr-FACP-4 samples, obtained by the means of ICP-OES, TGA, and fluorine-selective ISE are reported in table 4.2. Successful Mg and Sr doping and co-doping into the FACP nanoparticles is confirmed, with a doping level close to the theoretical values (1, 2, 5 wt.%). The incorporation of Mg or Sr in FACP-4 was based on a substitution mechanism with calcium ions, since incrementing the dopant concentration decreased Ca^{2+} content without altering PO_4^{3-} content. This was also proved by the (Ca+Mg+Sr)/P ratios of the samples that are identical to the Ca/P ratio of undoped FACP and did not change with doping or co-doping. Mg and Sr doping increased almost linearly with the concentration of the ion in the precursor solution. The maximum doping achieved is approx. 4 wt.% and was not influenced by co-doping. The F^- content of Sr-FACP-4 samples was identical to FACP-4, while in Mg-FACP-4 and MgSr-FACP-4 the presence of magnesium induced an increased fluoride content. TGA losses confirm the presence of carbonate and citrate ions also in Mg,Sr-FACP-4 with a similar content to FACP-4.

Table 4.2. Chemical composition of the Mg,Sr-FACP-4 powder samples

Sample	Ca (wt%)[a]	P (wt%)[a]	Mg (wt%)[a]	Sr (wt%)[a]	F (wt%)[b]	(Ca+Mg+Sr)/P (mol)[a]	Citrate (wt%)[c]	Carbonate (wt%)[c]
1Sr-FACP-4	32.8 ± 0.9	14.2 ± 0.5	-	0.50 ± 0.02	1.72 ± 0.02	1.80 ± 0.01	1.6 ± 0.2	4.6 ± 0.5
2Sr-FACP-4	31.2 ± 0.2	13.7 ± 0.1	-	2.35 ± 0.01	1.70 ± 0.07	1.82 ± 0.01	1.4 ± 0.1	4.6 ± 0.5
5Sr-FACP-4	28.4 ± 0.3	12.7 ± 0.1	-	4.13 ± 0.03	1.65 ± 0.05	1.84 ± 0.01	1.5 ± 0.2	5.0 ± 0.5
1Mg-FACP-4	32.1 ± 0.8	14.5 ± 0.3	1.46 ± 0.03	-	2.14 ± 0.03	1.83 ± 0.01	1.5 ± 0.2	4.3 ± 0.4
2Mg-FACP-4	31.0 ± 0.3	14.7 ± 0.2	2.39 ± 0.02	-	2.23 ± 0.03	1.83 ± 0.01	1.6 ± 0.2	4.4 ± 0.4
5Mg-FACP-4	26.1 ± 0.2	13.2 ± 0.2	3.60 ± 0.03	-	3.08 ± 0.04	1.88 ± 0.01	1.7 ± 0.2	3.7 ± 0.4
1MgSr-FACP-4	31.5 ± 0.5	14.4 ± 0.2	1.42 ± 0.02	0.56 ± 0.01	2.09 ± 0.02	1.83 ± 0.01	1.5 ± 0.1	4.5 ± 0.5
2MgSr-FACP-4	29.4 ± 0.5	14.4 ± 0.2	2.27 ± 0.04	2.27 ± 0.04	2.15 ± 0.03	1.83 ± 0.01	1.8 ± 0.2	4.3 ± 0.4
5MgSr-FACP-4	23.2 ±0.2	12.6 ± 0.2	3.48 ± 0.03	3.77 ± 0.05	2.73 ± 0.04	1.89 ± 0.01	3.2 ± 0.2	3.5 ± 0.4

[a]Quantified by ICP-OES; [b]Quantified by fluoride ion electrode; [c]Quantified by TGA.

In order to confirm that Mg,Sr-FACP-4 possess the same properties of FACP-4 as material for dental remineralization it was evaluated ionic (Ca^{2+}, Mg^{2+}, and Sr^{2+}) release in acidified artificial saliva (Figure 4.8). Mg,Sr-FACP-4 samples show a gradual and progressive release of Ca^{2+} ions comparable to FACP-4, independently from the doping level. Mg^{2+} ions were released twice faster than Ca^{2+} ions while Sr^{2+} followed a release kinetic similar to calcium ions. However, Sr^{2+} release kinetic seems to be influenced by co-doping, where the co-doped samples released strontium more slowly. The different release rates of Mg^{2+} and Sr^{2+} ions in Mg,Sr-FACP-4 samples could be due to different stabilities of these ions in FACP matrix, but further studies are needed to explain these trends.

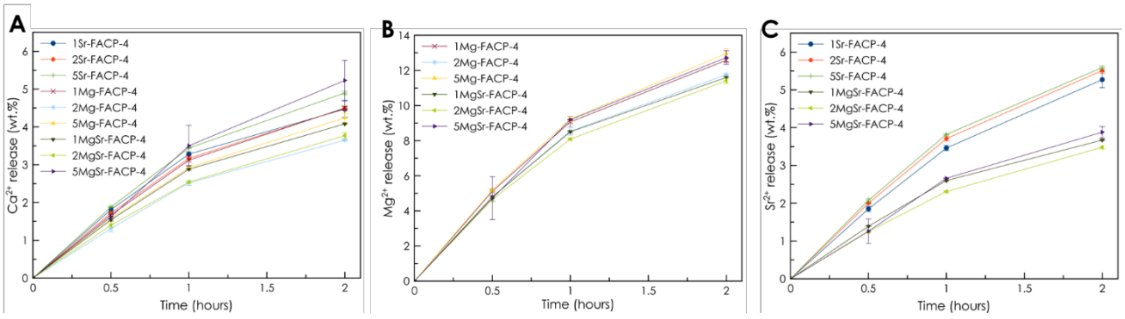

Figure 4.8. (A) Cumulative Ca^{2+} ions release from Mg,Sr-FACP-4 samples. (B) Cumulative Mg^{2+} ions release from Mg,Sr-FACP-4 samples. (C) Cumulative Sr^{2+} ions release from Mg,Sr-FACP-4 samples.

Characterization of Mg,Sr-FACP at different Cit/Ca ratio

After confirming the successful doping with Mg and Sr ions in FACP-4, the Cit/Ca ratio was changed to 2 and 1 while keeping Mg and Sr concentration at the highest level. Chemical composition and specific surface area of 5Mg,Sr-FACP-(2,1) samples, obtained by the means of ICP-OES, TGA, BET, and fluorine-selective ISE are reported in Table 4.3. As already observed for FACP, the Cit/Ca ratio did not influence the chemical composition nor Mg and Sr doping. The values of SSA_{BET} of 5Mg,Sr-FACP nanoparticles were comparable with FACP nanoparticles previously described, in the range of 240 – 350 m^2/g, and were higher when the Cit/Ca ratio was 1. On the other hand, Mg and Sr doping did not influence the specific surface area of the samples.

Table 4.3. Chemical composition and specific surface area (SSA_{BET}) of the 5Mg,Sr-FACP powder samples

Sample	Ca (wt%)[a]	P (wt%)[a]	Mg (wt%)[a]	Sr (wt%)[a]	(Ca+Mg+Sr)/P (mol)[a]	F (wt%)[b]	Citrate (wt%)[c]	Carbonate (wt%)[c]	SSA($m^2 g^{-1}$)[d]
5Sr-FACP-4	28.4 ± 0.3	12.7 ± 0.1	-	4.1 ± 0.03	1.84 ± 0.01	1.65 ± 0.05	1.5 ± 0.2	5.0 ± 0.5	-
5Sr-FACP-2	30.0 ± 0.9	13.4 ± 0.4	-	3.6 ± 0.1	1.83 ± 0.01	2.23 ± 0.06	8.50[e]		238 ± 24
5Sr-FACP-1	29.4 ± 0.1	12.9 ± 0.1	-	3.8 ± 0.1	1.86 ± 0.02	2.47 ± 0.08	7.22[e]		352 ± 35
5Mg-FACP-4	26.1 ± 0.2	13.2 ± 0.2	3.60 ± 0.03	-	1.88 ± 0.01	3.08 ± 0.04	1.7 ± 0.2	3.7 ± 0.4	-
5Mg-FACP-2	27.3 ± 0.4	14.2 ± 0.2	3.65 ± 0.05	-	1.82 ± 0.01	3.43 ± 0.08	3.0 ± 0.3	4.3 ± 0.4	289 ± 30
5Mg,F-ACP-1	26.1 ± 0.2	13.2 ± 0.2	3.60 ± 0.03	-	1.88 ± 0.01	3.08 ± 0.04	3.0 ± 0.3	3.6 ± 0.4	304 ± 30
5MgSr-FACP-4	23.2 ± 0.2	12.6 ± 0.2	3.48 ± 0.03	3.8 ± 0.1	1.89 ± 0.01	2.73 ± 0.04	2.0 ± 0.2	3.9 ± 0.4	-
5MgSr-FACP-2	25.3 ± 0.3	13.2 ± 0.2	3.06 ± 0.04	3.6 ± 0.1	1.86 ± 0.03	4.07 ± 0.08	2.8 ± 0.3	4.5 ± 0.5	223 ± 22
5MgSr-FACP-1	23.2 ±0.2	12.6 ± 0.2	3.48 ± 0.03	3.8 ± 0.1	1.89 ± 0.01	2.73 ± 0.04	3.2 ± 0.2	3.5 ± 0.4	318 ± 32

[a]Quantified by ICP-OES; [b]Quantified by fluoride ion electrode; [c]Quantified by TGA; [d]Calculated from BET adsorption. [E]In case of 5Sr-FACP-2 and 5Sr-FACP-1 the citrate and carbonate weight losses were superimposed and cannot be deconvoluted.

The influence of the Cit/Ca ratio on Mg,Sr-FACP has been evaluated on ionic (Ca^{2+} and F^-) release in acidified artificial saliva (Figure 4.9). 5Mg,Sr-FACP-(4, 2, 1) samples show a gradual and progressive release of Ca^{2+}, Mg^{2+}, Sr^{2+} and F^- ions comparable to FACP-(4, 2, 1), where the highest release was achieved when the Cit/Ca ratio was 2 or 1. This further confirms that Mg and Sr doping does not alter the release kinetics and that the Cit/Ca ratio continues to act as a control parameter of material properties also in Mg,Sr-FACP samples.

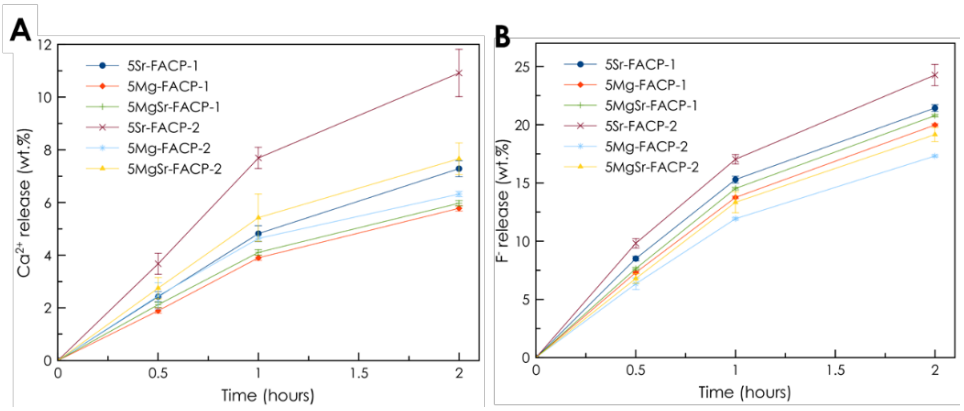

Figure 4.9. (A) Cumulative Ca^{2+} ions release from 5Mg,Sr-FACP-2/1 samples. (B) Cumulative F^- ions release from 5Mg,Sr-FACP-2/1 samples.

4.2.4 Conclusion

Biologically relevant magnesium and strontium ions were successfully introduced in FACP nanoparticles. The obtained Mg doped-, Sr doped-, or Mg,Sr co-doped- FACP nanoparticles incorporated the doping ions within the amorphous structure without forming secondary phases up to 4 wt.% of each doping ion. On the basis of our data even higher doping ratios could be achieved, but a doping level ≈5 wt.% was considered sufficient to impart the desired features. The doping mechanism is based on Ca^{2+} substitution with Mg^{2+}/Sr^{2+}, as evinced by chemical composition. The ionic doping did not change significantly the nature of the materials or their chemical composition. The doping did not alter the physicochemical properties of Mg,Sr-FACP, that were identical to FACP as proved by SSA_{BET} values and by release rates in artificial saliva. The only exception was Sr release rate that was slightly lower in the case of co-doped samples, and Mg release rate that was higher than other cations release rates. This latter phenomenon could be explained as a low stability of Mg^{2+} ions in the ACP structure, similarly to HA, that leads to an accelerated depletion of this ion.

In summary, the data have proven that Mg,Sr-FACP is similar to FACP in terms of physicochemical properties. Also in Mg,Sr-FACP citrate regulates surface area and ion release kinetics. The results suggest that MgSr-FACP has the potentiality to be an excellent remineralization material as FACP, but it could have the additional beneficial effects of the synergistic remineralization of Sr and F, the antibacterial effect of Sr and can restore depleted Mg in enamel. All these features will be evaluated *in vitro* and *in vivo* in future works.

4.3 Bibliography

1. Neel, E.A.A., et al., *Demineralization–remineralization dynamics in teeth and bone.* International Journal of Nanomedicine, 2016. 11: p. 4743-4763.
2. Cochrane, N.J., et al., *New Approaches to Enhanced Remineralization of Tooth Enamel.* Journal of Dental Research, 2010. 89(11): p. 1187-1197.
3. Enax, J. and M. Epple, *Synthetic hydroxyapatite as a biomimetic oral care agent.* Oral Health and Preventive Dentistry, 2018. 16(1): p. 7-19.
4. Roveri, N., et al., *Surface Enamel Remineralization: Biomimetic Apatite Nanocrystals and Fluoride Ions Different Effects.* Journal of Nanomaterials, 2009.
5. Zhang, X., X. Deng, and Y. Wu, *Remineralizing Nanomaterials for Minimally Invasive Dentistry*, in *Nanotechnology in Endodontics: Current and Potential Clinical Applications*, A. Kishen, Editor. 2015, Springer International Publishing: Cham. p. 173-193.
6. Zhao, J., et al., *Amorphous calcium phosphate and its application in dentistry.* Chemistry Central Journal, 2011. 5(1): p. 1-7.
7. Ruan, Q. and J. Moradian-Oldak, *Amelogenin and enamel biomimetics.* Journal of Materials Chemistry B, 2015. 3(16): p. 3112-3129.
8. Li, L., et al., *Repair of enamel by using hydroxyapatite nanoparticles as the building blocks.* Journal of Materials Chemistry, 2008. 18(34): p. 4079-4084.
9. Melo, M.A.S., et al., *Nanotechnology-based restorative materials for dental caries management.* Trends in Biotechnology, 2013. 31(8): p. 459-467.
10. Betts, F. and A.S. Posner, *An X-ray radial distribution study of amorphous calcium phosphate.* Materials Research Bulletin, 1974. 9(3): p. 353-360.
11. Posner, A.S., F. Betts, and N.C. Blumenthal, *Formation and structure of synthetic and bone hydroxyapatites.* Progress in Crystal Growth and Characterization, 1980. 3(1): p. 49-64.
12. Boskey, A.L. and A.S. Posner, *Conversion of amorphous calcium phosphate to microcrystalline hydroxyapatite. A pH-dependent, solution-mediated, solid-solid conversion.* The Journal of Physical Chemistry, 1973. 77(19): p. 2313-2317.
13. Hannig, M. and C. Hannig, *Nanomaterials in preventive dentistry.* Nat Nano, 2010. 5(8): p. 565-569.
14. Zhao, J., et al., *First detection, characterization, and application of amorphous calcium phosphate in dentistry.* Journal of Dental Sciences, 2012. 7(4): p. 316-323.
15. Robinson, C., et al., *Subunit Structures in Hydroxyapatite Crystal Development in Enamel: Implications for Amelogenesis Imperfecta.* Connective Tissue Research, 2003. 44(1): p. 65-71.
16. Combes, C. and C. Rey, *Amorphous calcium phosphates: Synthesis, properties and uses in biomaterials.* Acta Biomaterialia, 2010. 6(9): p. 3362-3378.
17. Dorozhkin, S.V., *Amorphous calcium (ortho)phosphates.* Acta Biomaterialia, 2010. 6(12): p. 4457-4475.
18. Reynolds, E.C., *Anticariogenic complexes of amorphous calcium phosphate stabilized by casein phosphopeptides: a review.* Special Care in Dentistry, 1998. 18(1): p. 8-16.
19. Wang, H., et al., *Oriented and Ordered Biomimetic Remineralization of the Surface of Demineralized Dental Enamel Using HAP@ACP Nanoparticles Guided by Glycine.* Scientific Reports, 2017. 7: p. 40701.
20. Xiao, Z., et al., *Rapid biomimetic remineralization of the demineralized enamel surface using nano-particles of amorphous calcium phosphate guided by chimaeric peptides.* Dental Materials, 2017. 33(11): p. 1217-1228.
21. Li, Y. and W. Weng, *In vitro synthesis and characterization of amorphous calcium phosphates with various Ca/P atomic ratios.* Journal of Materials Science: Materials in Medicine, 2007. 18(12): p. 2303-2308.

22. Wu, Z., et al., *Self-Etch Adhesive as a Carrier for ACP Nanoprecursors to Deliver Biomimetic Remineralization.* Acs Applied Materials & Interfaces, 2017. 9(21): p. 17710-17717.
23. Qi, C., et al., *Highly Stable Amorphous Calcium Phosphate Porous Nanospheres: Microwave-Assisted Rapid Synthesis Using ATP as Phosphorus Source and Stabilizer, and Their Application in Anticancer Drug Delivery.* Chemistry – A European Journal, 2013. 19(3): p. 981-987.
24. Yang, X., et al., *Influence of magnesium ions and amino acids on the nucleation and growth of hydroxyapatite.* CrystEngComm, 2011. 13(4): p. 1153-1158.
25. Tang, Q.-L., et al., *Porous nanocomposites of PEG-PLA/calcium phosphate: room-temperature synthesis and its application in drug delivery.* Dalton Transactions, 2010. 39(18): p. 4435-4439.
26. Li, J., et al., *Long-term remineralizing effect of casein phosphopeptide-amorphous calcium phosphate (CPP-ACP) on early caries lesions in vivo: A systematic review.* Journal of Dentistry, 2014. 42(7): p. 769-777.
27. Rahiotis, C. and G. Vougiouklakis, *Effect of a CPP-ACP agent on the demineralization and remineralization of dentine in vitro.* Journal of Dentistry, 2007. 35(8): p. 695-698.
28. Poggio, C., et al., *Analysis of dentin/enamel remineralization by a CPP-ACP paste: AFM and SEM study.* Scanning, 2013. 35(6): p. 366-374.
29. Farooq, I., et al., *A review of novel dental caries preventive material: Casein phosphopeptide–amorphous calcium phosphate (CPP–ACP) complex.* King Saud University Journal of Dental Sciences, 2013. 4(2): p. 47-51.
30. Zero, D.T., *Dentifrices, mouthwashes, and remineralization/caries arrestment strategies.* BMC Oral Health, 2006. 6(1): p. 1-13.
31. Lynch, R., R. Navada, and R. Walia, *Low-levels of fluoride in plaque and saliva and their effects on the demineralisation and remineralisation of enamel; role of fluoride toothpastes.* International dental journal, 2004. 54(S5): p. 304-309.
32. ten Cate, J.M., *Contemporary perspective on the use of fluoride products in caries prevention.* Br Dent J, 2013. 214(4): p. 161-167.
33. M, L.R.J. and C.J. M, *The anti-caries efficacy of calcium carbonate-based fluoride toothpastes.* International dental journal, 2005. 55(S3): p. 175-178.
34. Ionescu, A.C., et al., *Streptococcus mutans adherence and biofilm formation on experimental composites containing dicalcium phosphate dihydrate nanoparticles.* Journal of Materials Science: Materials in Medicine, 2017. 28(7): p. 108.
35. Everett, E.T., *Fluoride's Effects on the Formation of Teeth and Bones, and the Influence of Genetics.* Journal of Dental Research, 2011. 90(5): p. 552-560.
36. Angelini, E., et al., *Low-noble metal alloys: in vitro corrosion evaluation.* Journal of Materials Science: Materials in Medicine, 1993. 4(2): p. 142-149.
37. Duffó, G. and E.Q. Castillo, *Development of an artificial saliva solution for studying the corrosion behavior of dental alloys.* Corrosion, 2004. 60(6): p. 594-602.
38. Chatzipanagis, K., et al., *Crystallization of citrate-stabilized amorphous calcium phosphate to nanocrystalline apatite: a surface-mediated transformation.* CrystEngComm, 2016. 18(18): p. 3170-3173.
39. Iafisco, M., et al., *The growth mechanism of apatite nanocrystals assisted by citrate: relevance to bone biomineralization.* CrystEngComm, 2015. 17(3): p. 507-511.
40. Chen, Y., et al., *Stabilizing amorphous calcium phosphate phase by citrate adsorption.* CrystEngComm, 2013.
41. Dorozhkin, S.V., *Calcium orthophosphates (CaPO4): occurrence and properties.* Progress in Biomaterials, 2016. 5(1): p. 9-70.

42. Vecstaudza, J. and J. Locs, *Novel preparation route of stable amorphous calcium phosphate nanoparticles with high specific surface area.* Journal of Alloys and Compounds, 2017. 700: p. 215-222.
43. Xu, H.H.K., et al., *Nanocomposite containing amorphous calcium phosphate nanoparticles for caries inhibition.* Dental Materials, 2011. 27(8): p. 762-769.
44. Chen, J., et al., *Effects of fluorine on the structure of fluorohydroxyapatite: a study by XRD, solid-state NMR and Raman spectroscopy.* Journal of Materials Chemistry B, 2015. 3(1): p. 34-38.
45. Arends, J., et al., *Rate and mechanism of enamel demineralization in situ.* Caries research, 1992. 26(1): p. 18-21.
46. Øgaard, B., G. Rølla, and J. Arends, *Orthodontic appliances and enamel demineralization: Part 1. Lesion development.* American Journal of Orthodontics and Dentofacial Orthopedics, 1988. 94(1): p. 68-73.
47. Elliott, J.C., *Calcium phosphate biominerals.* Reviews in Mineralogy and Geochemistry, 2002. 48(1): p. 427-453.
48. Wopenka, B. and J.D. Pasteris, *A mineralogical perspective on the apatite in bone.* Materials Science and engineering: C, 2005. 25(2): p. 131-143.
49. Gross, K.A. and C.C. Berndt, *Biomedical application of apatites.* Reviews in Mineralogy and Geochemistry, 2002. 48(1): p. 631-672.
50. Šupová, M., *Substituted hydroxyapatites for biomedical applications: A review.* Ceramics International, 2015. 41(8): p. 9203-9231.
51. Boanini, E., M. Gazzano, and A. Bigi, *Ionic substitutions in calcium phosphates synthesized at low temperature.* Acta biomaterialia, 2010. 6(6): p. 1882-1894.
52. Curzon, M. and F. Losee, *Strontium content of enamel and dental caries.* Caries research, 1977. 11(6): p. 321-326.
53. Lippert, F., *The effects of fluoride, strontium, theobromine and their combinations on caries lesion rehardening and fluoridation.* Archives of Oral Biology, 2017. 80: p. 217-221.
54. Thuy, T.T., et al., *Effect of strontium in combination with fluoride on enamel remineralisation in vitro.* Archives of Oral Biology, 2008. 53(11): p. 1017-1022.
55. Featherstone, J., et al., *Acid reactivity of carbonated apatites with strontium and fluoride substitutions.* Journal of Dental Research, 1983. 62(10): p. 1049-1053.
56. Ravi, N.D., R. Balu, and T. Sampath Kumar, *Strontium-substituted calcium deficient hydroxyapatite nanoparticles: Synthesis, characterization, and antibacterial properties.* Journal of the American Ceramic Society, 2012. 95(9): p. 2700-2708.
57. Lin, Y., et al., *Synthesis, characterization and antibacterial property of strontium half and totally substituted hydroxyapatite nanoparticles.* Journal of Wuhan University of Technology-Mater. Sci. Ed., 2008. 23(4): p. 475-479.
58. Krishnan, V., A. Bhatia, and H. Varma, *Development, characterization and comparison of two strontium doped nano hydroxyapatite molecules for enamel repair/regeneration.* Dental Materials, 2016. 32(5): p. 646-659.
59. Legfros, R., et al., *Magnesium and carbonate in enamel and synthetic apatites.* Advances in Dental Research, 1996. 10(2): p. 225-231.
60. Spencer, P., et al., *Incorporation of magnesium into rat dental enamel and its influence on crystallization.* Archives of Oral Biology, 1989. 34(10): p. 767-771.
61. LeGeros, R.Z., et al., *Synergistic effects of magnesium and carbonate on properties of biological and synthetic apatites.* Connective Tissue Research, 1995. 33(1-3): p. 203-209.
62. Hallsworth, A., C. Robinson, and J. Weatherell, *Mineral and magnesium distribution within the approximal carious lesion of dental enamel.* Caries Res, 1972. 6(2): p. 156-68.

Chapter 5. Controlling calcium phosphate nanoparticles formation

Biogenic hydroxyapatite nanocrystals are intriguing biominerals whose formation in the organisms is still far away to be completely understood. They constitute the inorganic component of the hard tissues of vertebrates, forming an extremely strong and tough composite with collagen proteins, assembled in a complex hierarchy. HA biomineralization is a complicated process that arises on the interaction between ions, small organic molecules, collagen and non-collagenous proteins. The study of HA formation is crucial not only to understanding how living organisms form their extremely specialized mineralized structures, but also to achieve synthetic advanced materials replicating the biogenic material for application in regenerative medicine and bone tissue engineering [1].

Several synthesis methods have been set-up to generate HA nanocrystals with tailored size, morphology, surface properties, chemical composition and crystallinity [2-6]. Organic templates or additives can be employed to finely control nucleation and crystal growth [6, 7]. Commonly, these molecules influence the nucleation and crystal growth of HA by interacting with calcium or phosphate ions in the early stage of mineralization. The additives can also preferentially bind to specific crystal faces, thus inhibiting crystal growth on the respective crystallographic axes [8]. In this respect biological macromolecules, polymers, amines, amino acids, fatty acids, and carboxylates have been used to tailor the properties of biomimetic HA nanocrystals [9, 10].

Citrate was widely studied as a "bio-inspired" organic additive in HA synthesis because it is the most abundant non-macromolecular organic component of bone and constitutes up to the 5.5 wt. % of bone organic content [11]. The strong effect of citrate on HA crystallization has been studied using complementary techniques such as X-ray diffraction (XRD) and synchrotron X-ray Wide Angle total scattering (WAXTS) [12], atomic force microscopy (AFM) [12, 13], solid-state nuclear magnetic resonance (ssNMR) [11], IR and Raman spectroscopy [14], and high resolution transmission electron microscopy (HRTEM) [15]. These studies have proved that citrate plays a dual role in HA crystallization. First, citrate drives the growth of HA via an amorphous precursor, and second citrate induces a non-classical oriented aggregation of the nanocrystals [12, 14, 16, 17].

In detail, these previous works have shown that an initial precipitation of sodium citrate crystals acted as temporal templates, triggering heterogeneous nucleation of ACP with an unusual platy shape [12]. Then the ACP nanoparticles, stabilized by the adsorption of citrate ions, were progressively transformed into platy HA nanoparticles [12]. The ACP transformation occurs from the inside of the nanoparticle toward to the outside. Once the HA is formed, citrate is attached only to specific faces.

Part of the data included in this chapter will be used to prepare a paper with tentative title "*Degli Esposti, L., Adamiano, A., Tampieri, A., Ramírez-Rodríguez, G. B., Delgado-López, J. M., Sakhno, Y., Martra, G., Siliqi, D., Giannini, C., Iafisco, M. Citrate assisted synthesis of fluorine doped enamel-like hydroxyapatite nanorods"*.

It has been recently demonstrated that citrate can strongly bind only the calcium of the faces of the *a(b)*-planes (faces parallel to the *c*-axis, especially (1 0 -1 0) face), stopping further growths in these directions, controlling the thickness and width of the nanocrystals and maintain the platy morphology [11]. This interaction occurs because the spacing between Ca^{2+} ions (0,320 nm or 0,688 nm) matches with either the spacing between the centers of two neighbor -COO^- citrate groups (0,320 nm) or the distance between the two terminal carboxylates of citrate (0,688 nm). Afterward, the uniaxial alignment of crystalline subunits along the c-axis takes place [17]. This leads to an oriented aggregation of nanocrystals, where HA subunits can interact with each other by van der Waals or hydrogen bonding interactions through the (0 0 0 1) faces (head-tail attachment) since they are not covered by citrate and thus the primary subunits can be in the crystallographic register with respect to the neighboring crystals. The driving force of oriented aggregation is the reduction of the overall crystal surface energy to lower the contribution of the unsatisfied surface bond. In HA case citrate ions adsorbed on the faces of the *a(b)* plane eliminates high-energy facets forcing the interaction between the (0 0 0 1) faces. At the highest maturation time solid-state rearrangement of the subunits takes place through the growth of two (0 0 0 1) adjacent faces, acting as glue, leading to the formation of elongated crystals [17].

Therefore citrate played the distinct role of inducing the platy morphology of the amorphous precursor and controlling the thickness of the HA nanocrystals, breaking their hexagonal symmetry. A similar mechanism might occur in bone mineralization, where citrate ions might play a broader role than has been depicted to date of controlling size and morphology of biogenic HA, alone or in synergy with macromolecules. Furthermore synthetic citrate-functionalized HA nanocrystals were proven to have excellent biocompatibility and colloidal stability [14] and have been tested for drug delivery, imaging, coating of metallic prostheses, and many other applications [18-22].

In this chapter will be reported the research work aimed to elucidate the mechanisms that regulate CaP NPs formation, in order to increase the "toolbox" of methods to control CaP NPs properties for the functional by design approach. Specifically, the influence if citrate ions was the main focus on the research work reported therein for the above-mentioned reasons. In detail, subchapter 5.1 will focus on effect of fluoride ions on the crystallization of citrate-stabilized HA. Subchapter 5.2 will focus on the relationships between citrate molecular structure and the crystallization of HA nanoparticles.

5.1 Influence of fluoride ions on the formation of calcium phosphate nanoparticles

5.1.1 Introduction

HA nanocrystals doped with foreign ions have recently attracted remarkable attention, since the ionic substitution is a powerful tool to improve their performances for different applications [23]. For example, doping was widely used for HA to give an antibacterial or osteoinductive activity, or for providing special properties like luminescence or magnetism [23].

Previous works have explored the addition of foreign ions in the citrate-HA nanocrystals and have studied their effect on the chemical-physical features of the resulting materials; namely, the preparation of citrate-HA doped with carbonate ions, metallic ions and lanthanide ions has been reported [14, 20, 24, 25]. Citrate has been employed in combination with carbonate to produce HA that closely matches the chemical composition of the mineral phase of bone [14]. It was found that the presence of carbonate ions generates nanocrystals that are smaller, less crystalline and more isotropic than those prepared without carbonate. Citrate-HA has been doped with divalent metallic ions such as cobalt, manganese or nickel ions [20]. In this case it was discovered that the divalent metal ions decreased nanocrystals size while increasing their aspect ratio in comparison to undoped citrate-HA. Europium ions were also incorporated in citrate-HA [25]. In this latter case, the presence of this lanthanide ion significantly modified the HA precipitation, inhibiting the crystallization and changing the stoichiometry of the material. It was proved that Eu-doped citrate-HA nanocrystals possess a strong luminescence and a long lifetime; it was also shown that the presence of citrate in these nanocrystals improved Eu fluorescence, quantum yield, and fluorescence lifetime in comparison to Eu-doped HA nanocrystals without citrate [24].

As mentioned in Chapter 4, fluoride is one of the most interesting anions for dental application, since it reduces enamel demineralization and inhibits the microorganisms in the cariogenic biofilm [26]. Fluoride-doped HA (FHA, $Ca_{10}(PO_4)_6(F)_x(OH)_{2-x}$, $0 < x \leq 2$) has recently been studied for osteoporosis treatment, as antibacterial biomaterial, for dental enamel protection and remineralization, and for improving the luminescence of the rare earth-doped HA [27-30]. Previous studies have demonstrated that fluoride doping influences the HA crystallinity, size of the crystalline domains, and morphology [23, 31, 32]. However, to the best of our knowledge there are no reports on FHA nanocrystals prepared in presence of citrate ions.

Considering the high interest that FHA has gained as advanced functional material and the control that we could get on the HA crystallization using citrate, the main aim of the work reported in this subchapter is the preparation of citrate-FHA nanoparticles and the investigation of their crystal structural evolution as a function of precipitation time. Herein, citrate-HA nanocrystals were prepared in presence of fluoride ions employing a thermal-decomplexing batch reaction developed by Delgado-López *et al.* [14]. The physical–chemical, morphological and crystallographic properties of the citrate-FHA nanocrystals at several maturation times have been thoroughly characterized by using conventional analytical techniques as well as synchrotron facilities and the effect of fluoride ions has been particularly highlighted.

5.1.2 Sample preparation and characterization

Sample preparation

Dry powder HA was synthesized as reported in the work of Delgado-López *et al.* [14]. Namely, two solutions (1:1 v/v, 200 mL total) of (i) 100 mM $CaCl_2$ + 400 mM Na_3(Cit) and (ii) 120 mM Na_2HPO_4 were mixed at room temperature. Afterward the mixture was thermostated at 80 °C under agitation in a water bath for three maturation times – that is to say 5 minutes, 30 minutes, and 4 hours. After maturation the particles were repeatedly washed with ultrapure water by centrifugation at 7000 rpm for 10 min and then freeze-dried overnight at -50 °C under a vacuum of 3 mbar. The lyophilized powders were subsequently grinded and sieved with a 50 µm sieve in order to achieve a uniform granulometry. FHA samples were prepared similarly to HA but with the addition of 50 mM NaF in solution (ii).

Physical-chemical characterizations

Samples were characterized by PXRD, Rietveld refinement, TEM, chemical composition analyses, FT-IR and Raman spectroscopy, electrophoretic potential, and TGA. Interpretation of the four TGA weight losses were attributed to adsorbed water (from room temperature to 150 °C), structural water (from 150 to 350 °C), citrate (from 350 to 700 °C) and carbonate (from 700 to 1000 °C).

The Small Angle X-ray Scattering (SAXS) experiments were performed at the ELETTRA Sincrotrone Trieste (Trieste, Italy) synchrotron on the high brilliance Austrian SAXS beamline. For the SAXS experiment the available q-range was 0.08 to about 6 nm-1 using an incident beam energy of 8 keV. A two-dimensional (2D) scattering image was acquired

within 100 ms with a Pilatus 1 M detector (Dectris, CH). The samples were measured at room temperature in glass capillaries of 1.5 mm diameter (WJM-Glas/Müller GmbH, Berlin-Pankow, DE). As a first step, the scattering from the air and the sample holder was collected to be subtracted as background. Subsequently, the scattering of FHA and HA powder samples was collected. The data reduction was done by the freely available software of the beamlines Fit2D [33]. The two-dimensional data were circularly averaged to convert them into one-dimensional scattering curves. Nine different scattering curves were collected for each sample and consequently were averaged and background corrected.

From the experimental curves, the modeling was performed by using SasView package V4.2.2 (www.sasview.org). We estimated the averaged particle size for selected models, and as well as an estimation of the polydispersity of the samples, by using Schulz distribution [34, 35], which is the most indicated to describe particle sizes.

5.1.3 Results and discussion

Crystallographic characterization

The PXRD patterns of all the samples show the typical diffraction peaks of HA as single phase (JCPDS Card file No. 9-432) (Figure 5.1). In particular, the most characteristic reflections are: a narrow peak at 25.87° that corresponds to the crystallographic plane (002), and a broad peak centered at about 32° that is the sum of three peaks at 31.77°, 32.19°, and 32.90°, which correspond to planes (211), (112), and (300). The other main peaks that were indexed are present at 39.81°, 46.71°, 49.46°, and 53.14°, which correspond to the planes (310), (222), (213), and (004), respectively [20]. As previously reported for other nanocrystalline HAs, the diffraction peaks are broad and poorly defined, indicating the presence of nanocrystals with reduced crystal domains in all the samples [14]. The XRD patterns of FHA 5m and HA 5m show particularly broad peaks, while the spectra recorded on the samples at increasing maturation times reveal a progressive peak sharpening. The increase of peaks resolution highlights that with maturation time the nanocrystals grow in size and improve the structural order. FHA peaks are always more defined than the corresponding HA peaks in all time points, suggesting that FHA samples are more ordered and bigger than HA.

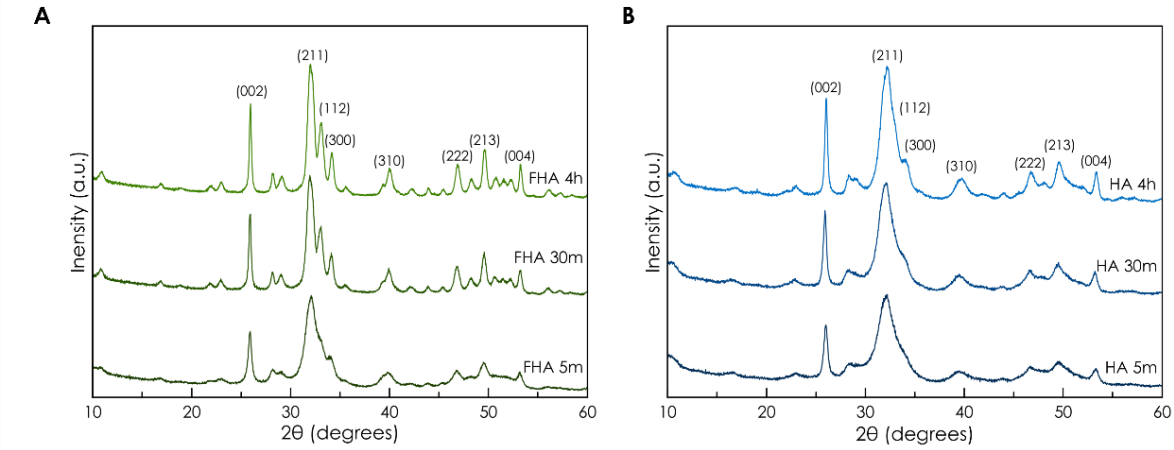

Figure 5.1. PXRD diffractograms of (A) FHA 5m, FHA 30m, and FHA 4h and (B) HA 5m, HA 30m, and HA 4h.

The evaluation of unit cell parameters extracted by Rietveld refinement of PXRD data show that the *a* unit cell parameters of FHA samples (Table 5.1) are always notably shorter than those of HA while the *c* unit cell parameters are comparable. A shortening of the *a* cell axis of ≈ 0.005 nm was reported for fluoride substitution and this was attributed to the shorter Ca-F equilibrium distance compared to the Ca-OH distance of undoped HA [36, 37]. The unit cell parameters of both materials shrinks at increasing

maturation time (Table 5.1). The unit cell parameters of HA calculated herein are close to those reported by Delgado-Lòpez *et. al.* by using synchrotron WAXS data [12].

Carbonate doping has a strong influence on HA unit cell parameters [12], however taking into account that the carbonate content is similar for FHA and HA (see data below) we can argue that this ion is not involved in the different crystallographic properties of FHA vs HA.

The dimensions of the crystal domains were estimated along the $D_{(00l)}$ and $D_{(hk0)}$ directions, that correspond to the longest and the shortest axes of the hexagonal crystal, respectively. For both samples the (002) and (310) reflections were used to calculate the $D_{(00l)}$ and $D_{(hk0)}$, respectively. The estimated crystal domain sizes are reported in Table 5.1.

The average size of crystal domains of FHA along the *c*-axis ($D_{(002)}$) and along the *a*–*b* plane ($D_{(310)}$) are both larger than the corresponding crystal domains of HA irrespective of the maturation time. However, for both materials the values of $D_{(002)}$ are higher than those of $D_{(310)}$indicating that the crystals are elongated along the *c*-axis. Interestingly, for FHA the aspect ratio estimated as $D_{(002)}/D_{(310)}$ remains constant with increasing maturation time, while in HA the aspect ratio increases over time. These data imply that FHA are bigger than HA nanocrystals in all time points and grow faster. A striking difference is that for FHA the growth is isotropic, since the aspect ratio remains constant, while for HA a preferential elongation along the *c*-axis occurs.

Table 5.1. Crystallographic parameters of FHA and HA samples

Sample	*a*-*b* cell axes*	*c* cell axis*	$D_{(002)}$*	$D_{(310)}$*	$D_{(002)}/D_{(310)}$*
	(Å)	(Å)	(nm)	(nm)	
HA – 5m	9,499	6,898	21,3±0,5	4,9±0,4	4,34
HA – 30m	9,472	6,895	26,8±0,5	6,2±0,8	4,32
HA – 4h	9,462	6,891	35,3±0,5	6,4±0,5	6,70
FHA – 5m	9,413	6,894	24,7±0,5	9,4±1,6	2,63
FHA – 30m	9,398	6,886	42,4±0,8	14,1±0,9	3,01
FHA – 4h	9,390	6,885	56,9±1,1	20,4±0,9	2,79

*Calculated by Rietveld refinement of PXRD data

Compositional analysis

The chemical composition and surface charge of the samples are reported in Table 5.2. The Ca/P ratios estimated by ICP for the FHA and HA nanocrystals do not change with maturation time. The Ca/P ratio of FHA is always higher than HA, and it is closer to the stoichiometric value (1.67). The higher structural order of FHA led to a more stoichiometric chemical composition. Fluoride content does not change with maturation time. The Ca/F ratio of FHA samples is close to the value of stoichiometric fluorapatite (Ca/F = 5 for $Ca_{10}(PO_4)_6(F)_2$). TGA analysis mainly shows four weight losses: (i) from room temperature to 200°C due to the adsorbed water, (ii) from 200°C to 400°C related to structural water, (iii) from 400 to 600°C due to the citrate, and (iv) from 600 to 1000°C corresponding to the carbonate ions [38]. The occurrence of carbonate ions is mainly due to dissolved CO_2 in the mother solution and its amount is similar in FHA and HA samples (<1 wt.%).

Interestingly, FHA has a statistically significant lower content of citrate than HA. The amount of structural water, carbonate as well as of citrate decreased with the maturation time for both FHA and HA, because of a progressive modification from non-apatitic chemical environments (non-stoichiometric, rich in water, foreign ions and molecules) to apatitic ones and a gradual dissolution of the surface hydrated layer with the time, as previously described [14]. The ζ-potential of the samples at pH 7.0 shows that FHA suspensions possess a surface charge comparable to HA, with a negative ζ-potential due to the presence of citrate ions on nanocrystals surface [18]. With increasing maturation time the ζ-potential decreased for both FHA and HA due to the decrease in the content of citrate ions, as mentioned above.

Table 5.2. Chemical composition of the samples

Sample	Ca[a] (wt%)	P[a] (wt%)	Ca/P[a] (mol)	F[b] (% wt)	Ca/F[a,b] (mol)	Citrate[c] (%wt.)	Carbonate[c] (%wt)	ζ-Potential (mV)
HA – 5m	26,39±0,16	13,23±0,23	1,54±0,02	-	-	1,97±0,20	1,1±0,10	-13.1 ± 0.4
HA – 30m	27,77±0,87	13,98±0,64	1,54±0,02	-	-	1,99±0,20	0,87±0,09	-12.4 ± 0.4
HA – 4h	28,13±0,08	14,25±0,10	1,53±0,01	-	-	1,56±0,15	0,71±0,07	-10.3 ± 0.4
FHA – 5m	28,27±0,48	13,20±0,26	1,60±0,01	3,07±0,24	4,40±0,45	1,55±0,15	1,10±0,10	-15.2 ± 0.4
FHA – 30m	29,04±0,69	14,20±0,38	1,58±0,01	3,00±0,06	4,58±0,22	1,46±0,15	0,89±0,09	-14.3 ± 0.3
FHA – 4h	29,70±0,17	14,40±0,10	1,59±0,01	2,99±0,02	4,58±0,22	1,39±0,10	0,96±0,10	-11.1 ± 0.8

[(a)]Quantified by ICP-OES; [(b)]Quantified by fluoride ion electrode; [(c)]Quantified by TGA

Spectroscopic characterization

The FTIR spectra of the samples are reported in Figure 5.2. All FHA samples displayed a main broad band at 1030 cm^{-1} with shoulders at 1046 and 1075 cm^{-1} due to the triply degenerated anti-symmetric stretching mode of the apatitic PO_4 groups (v_3PO_4). Other features emerge at 961 cm^{-1} (symmetric stretching mode of the apatitic PO_4 groups, v_1PO_4) and at 603, 576 (as a shoulder) and 565 cm^{-1} (triply degenerated bending mode of the same groups, v_4PO_4). Additionally, the spectra of HA 4h also show bands at 3567 and 631 cm^{-1} corresponding to the stretching and librational modes of the apatitic hydroxyl groups, respectively [39].

The absence of the bands associated to hydroxyl ions for FHA confirms the total substitution of the OH^- groups by F^- in the crystal lattice [37]. The presence of carbonate ions observed by TGA analysis was confirmed for both FHA and HA by the presence of B-type carbonate substitution (CO_3 occupying PO_4 sites) band at 873 cm^{-1} [40]. A shoulder of this band approx. at 880 cm^{-1} suggest the presence also of a minor amount of A-type carbonate substitution (CO_3 occupying OH sites).

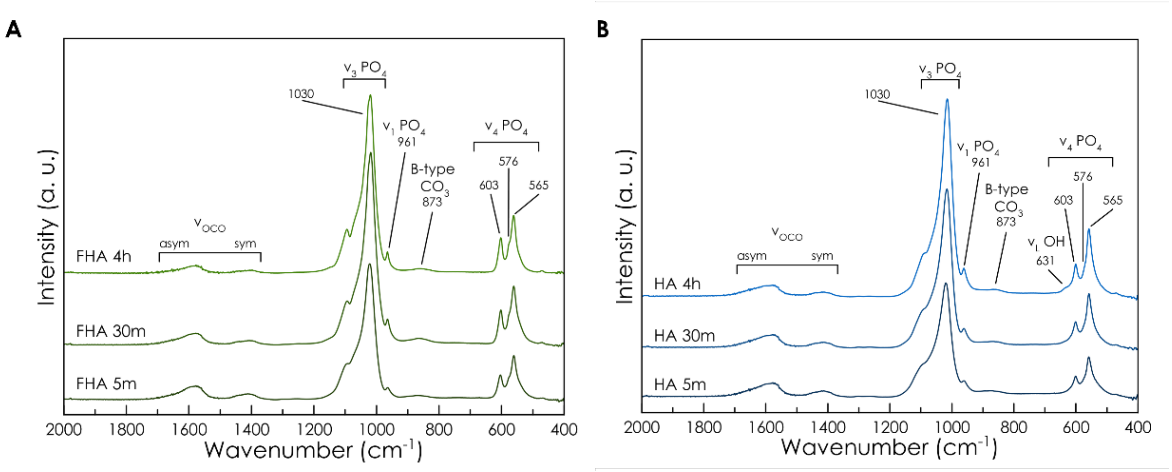

Figure 5.2. FT-IR spectra of (A) FHA 5m, FHA 30m, and FHA 4h (from dark green line to light green line) and (B) HA 5m, HA 30m, and HA 4h (from dark blue line to light blue line).

In the 1650–1350 cm^{-1} range the typical signals of carboxylate ions of citrate and carbonate as well as the signal of adsorbed water are present. The main component in 1700–1500 cm^{-1} range is attributed to the antisymmetric (hereafter named asym) stretching of OCO groups, while the symmetric (named sym) partner mode produces the pattern in the 1500 – 1350 cm^{-1} range.

Figure 5.3A represents the FTIR spectra of FHA 5m, FHA 4h, HA 5m, and HA 4h in the 1650–1350 cm^{-1} range. For both FHA and HA the $\nu_{asym}OCO$ signal at 1700–1500 cm^{-1} range was deconvoluted and fitted by using three components with the sub−bands located at 1646, 1597 and 1567 cm^{-1} (Figure 5.3B). Similarly, the $\nu_{sym}OCO$ signal at 1500–1350 cm^{-1} range was fitted by using three components with the sub−bands located at 1445, 1420 and 1400 cm^{-1}. The sub-bands at ca. 1400 and ca. 1597 cm^{-1} were assigned respectively to $\nu_{sym}OCO$ and $\nu_{asym}OCO$ signal of citrate ions coordinated to Ca^{2+} cations on the FHA/HA surface [41]. The $\nu_{sym}OCO$ sub-bands at 1445 and 1420 cm^{-1} were attributed to B-type carbonate signal, while 1567 cm^{-1} band was attributed to A-type carbonate signal. The 1646 cm^{-1} component was attributed to adsorbed water. The intensity of the bands of citrate and carbonate decrease with maturation time for both FHA and HA (Figure 5.3A). Therefore, FT-IR data are in agreement with chemical composition analyses.

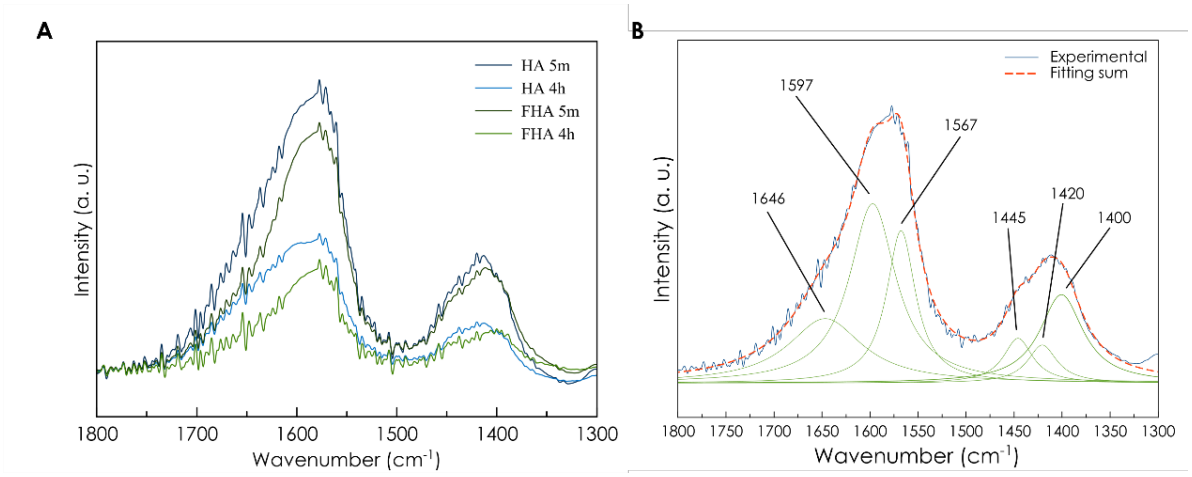

Figure 5.3. (A) FT-IR 1200-1800 range of FHA 5m, FHA 4h (dark green line and light green line) HA 5m, and HA 4h (dark blue line and light blue line). Spectra were normalized on ν_3PO_4 band intensity (B) Sub-bands deconvolution of FHA 5m FT-IR 1300-1800 range.

Figure 5.4 shows the Raman spectra of the samples. The most intense peak appears at 960 cm^{-1}, which corresponds to ν_1PO_4 mode. Other features from apatitic PO_4 group emerge at 1042 cm^{-1} (ν_3PO_4), at 586 (ν_4PO_4) and at 428 cm^{-1} (ν_2PO_4). In the spectrum of both FHA and HA nanoparticles, the B-type carbonate band appeared at 1070 cm^{-1} (ν_1CO_3) and at 1430 cm^{-1} (ν_2CO_3), confirming the data extracted from FTIR spectra [40]. Moreover, in the Raman spectrum of HA samples an intense peak at 3570 cm^{-1} can be clearly observed (Figure 5.4D), corresponding to the apatitic vOH mode. The intensity of this peak increases with maturation time. On the contrary, this band is not present in the spectrum collected for the FHA nanoparticles, further confirming that OH^- ions were completely replaced by fluoride ions. The

bands at 2930 and 845 cm^{-1} are related to the vCH_2 and the δOCO modes of citrate [42], respectively, and their relative intensity decreases with maturation time as observed in the FTIR spectra.

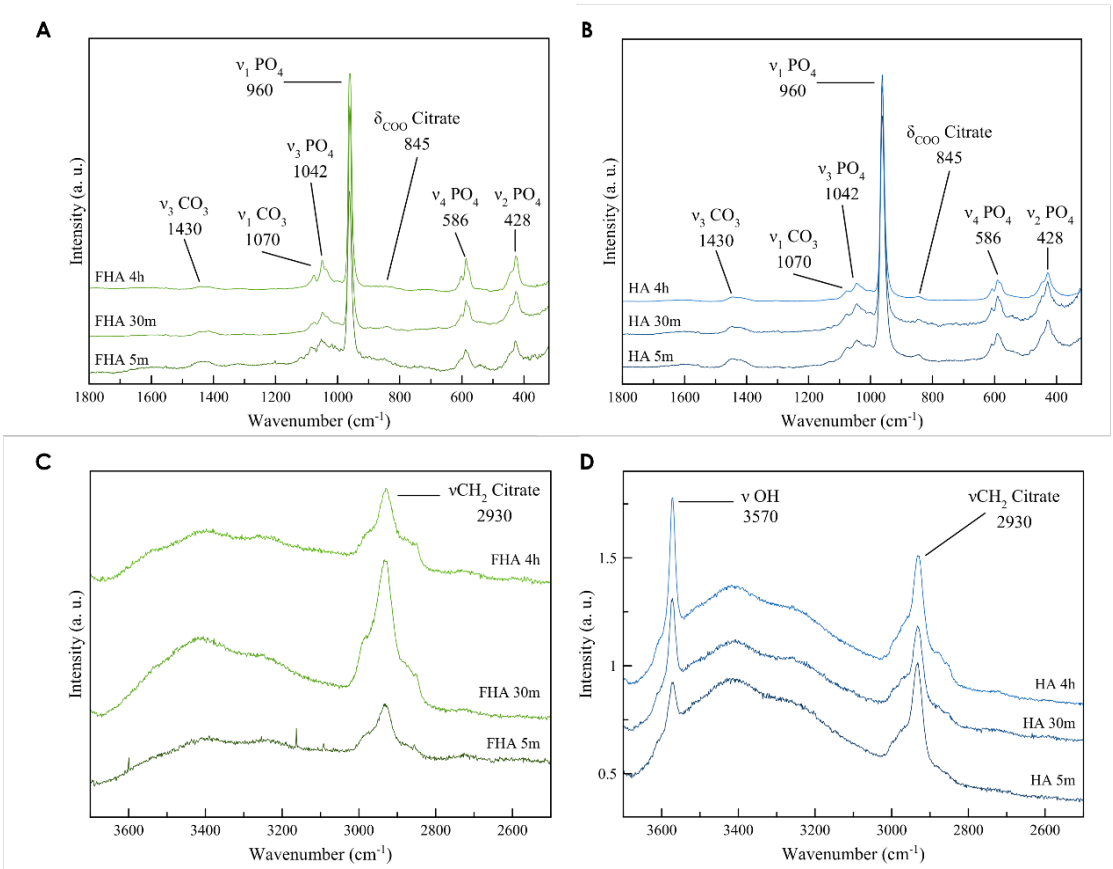

Figure 5.4. Raman spectra of (A) FHA 5m, FHA 30m, and FHA 4h (from dark green line to light green line) and (B) HA 5m, HA 30m, and HA 4h (from dark blue line to light blue line). Fig (C) and (D) show an enlarged view of the typical OH and CH stretching modes spectral region.

Morphological characterization

TEM micrographs of FHA nanocrystals are reported in Figure 5.5, while TEM micrographs of HA nanocrystals were previously reported [14, 17, 22]. After 5 minutes of maturation, FHA nanocrystals consist of irregular, very small particles with a low crystallinity degree as pointed out by the SAED patterns (insets in Figure 5.5A) that aggregate in elongated formations. FHA 30m instead is composed of elongated particles with better-defined border and with increased crystallinity, as evidenced by the SAED patterns (Figure 5.5B). Finally, TEM images of FHA 4h show highly regular crystalline nanoparticles with a rod-like morphology, having an average length of 60 ± 20 nm and an average width of 20 ± 4 nm (Figure 5.5C).

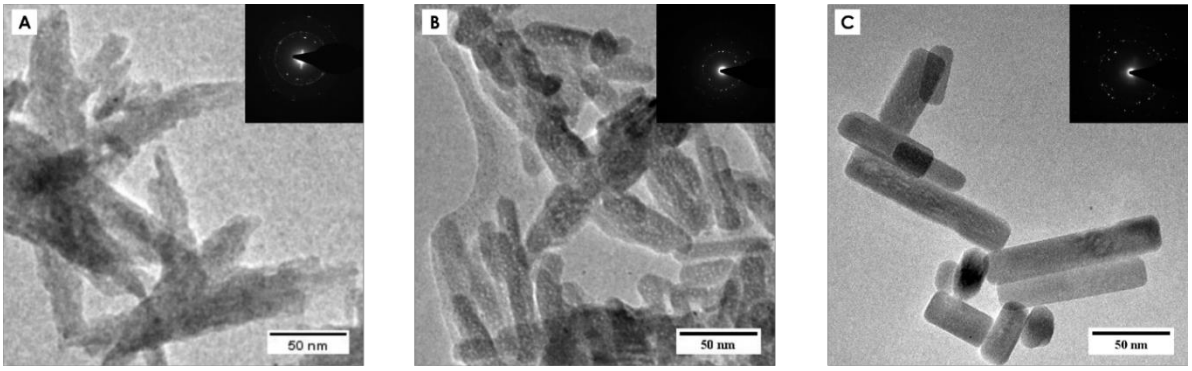

Figure 5.5. TEM micrographs of (A)FHA 5m, (B) FHA 30m and (C) FHA 4h (C). Insets show the SAED pattern collected for each sample.

The mean length (L) along the longest axis, the mean width (W) orthogonal to L, and the mean aspect ratio (R, i.e., the ratio between L and W) of single FHA nanocrystals were estimated from TEM observations and are reported in Table 5.3.

Table 5.3. Mean length (L), mean width (W), and mean aspect ratio (R) of FHA samples.

Sample	L[a]	W[a]	R[a]
	(nm)	(nm)	
FHA – 5m	39,5 ± 9,6	10,8 ± 3,5	3,7
FHA – 30m	53,7 ± 10,2	15,6 ± 2,3	3,4
FHA – 4h	76,9 ± 40,1	22,5 ± 4,6	3,4
HA – 5m[b]	98.6 ± 29.5	21.2 ± 4.6	4.7
HA – 4h[b]	84.8 ± 16.2	15.7 ± 3.8	5.6

[(a)] Measured from TEM micrographs. The mean value and the standard deviation were calculated measuring the sizes of 100 particles from different experiments. [(b)] Data from reference [14]

The L and W values of FHA gradually increase with the maturation time. In detail, Figure 5.6 represents the histograms with the width and length of FHA synthesized at different maturation times. The width of particles with the highest frequency distribution slightly increased as a function of maturation time (Figure 5.6A). Interestingly, the length of the particles with highest frequency distribution follows the

same trend, but at the same time the frequency distribution spreads over a wide range forming a lognormal distribution curve. This high spreading of length values explains the higher error associated to average L of FHA 4h.

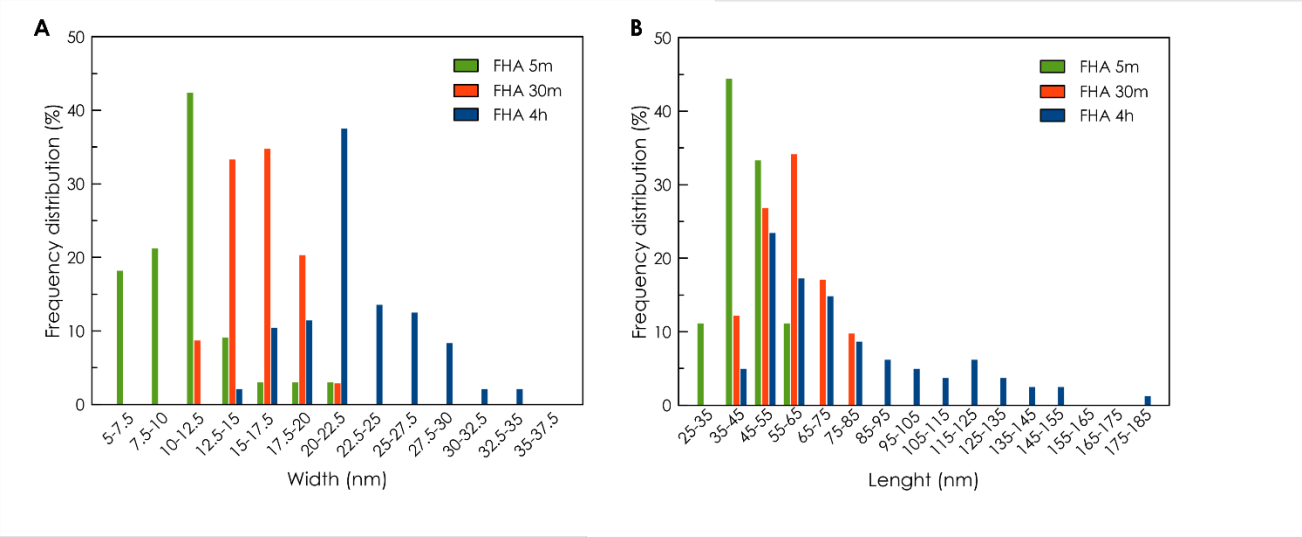

Figure 5.6. Histograms of the distributions of (A) width and (B) length of FHA 5m (green bars), FHA 30m (red bars) and FHA 4h (blue bars).

The increase over time of the average size of the nanocrystals dimensions is similar to the one observed for the crystal domains along the (002) and (310) directions calculated from PXRD patterns. Comparing the nanocrystals dimensions and the estimated crystals domains it is remarkable that the average TEM values are similar but slightly higher than the crystallite domains. The compositional data reported above and the literature suggest that FHA nanorods are probably composed of a well-ordered fluorapatitic core embedded in a ‘‘non-apatitic hydrated layer stabilized by citrate ions”, as proposed by Rey *et al.* [43, 44]. Taking into account that TEM micrographs represent the whole nanoparticles while data extracted from XRD analysis give an estimation of the size of the crystalline domains, the difference between TEM values and the crystallite domains can give an indication of the thickness of this non-apatitic layer. Following the same approach for HA samples it is observed that in this case the thickness of the non-apatitic layer is bigger, and this suggests that in comparison FHA has a thinner non-apatitic layer [14]. This indication is coherent with XRD data, that show that FHA has higher structural order than HA, and with compositional data, that indicates a smaller amount of citrate for FHA.

Representative high resolution TEM (HR-TEM) micrographs of FHA 5m and FHA 4h are reported in Figure 5.7. For FHA 5m, in a few cases, the lattice fringes spaced at ca. 0.815 nm turned up (Figure 5.7A). This lattice fringe value corresponds to the distance of the (1 0 −1 0) plane of HA (JCPDS file no. 9-432),

indicating that the crystals are elongated along the *c*-axis. For FHA 4h the 0.815 nm fringes were more clearly and frequently observed than FHA 5m sample, confirming their higher structural order. Inspections at high magnification revealed that lattice fringes due to (1 0 −1 0) planes ran uninterrupted for the whole nanocrystal. Moreover, some facets of the a(b)-planes (e.g., (0 −1 1 0) facet in Figure 5.7B) exhibited stepped surfaces indicating that they grew following a classical layer-by-layer mechanism. Also fringes with a spacing of 0.344 and 0.526 nm were observed (Fig. 5.8A-C). The former were orthogonal to the nanocrystal main axis, while the latter were tilted at 45 degrees. These two fringes correspond to (002) and (101) lattice planes of the [1 0 -1 0] crystal face. Interestingly, in a few cases lattice fringes spaced at ca. 0.344 nm with a hexagonal pattern were observed, suggesting that for these particles the *c*-axis was parallel to the electron beam during the image acquisition [45]. Therefore in these cases it was possible to observe nanocrystal width and thickness, and from these micrographs the nanorod thickness (T) was estimated, giving a W/T ratio of ≈ 1.5. The W/T ratio close to 1 suggest an almost cylindrical isotropy, confirming that FHA nanocrystals are rods.

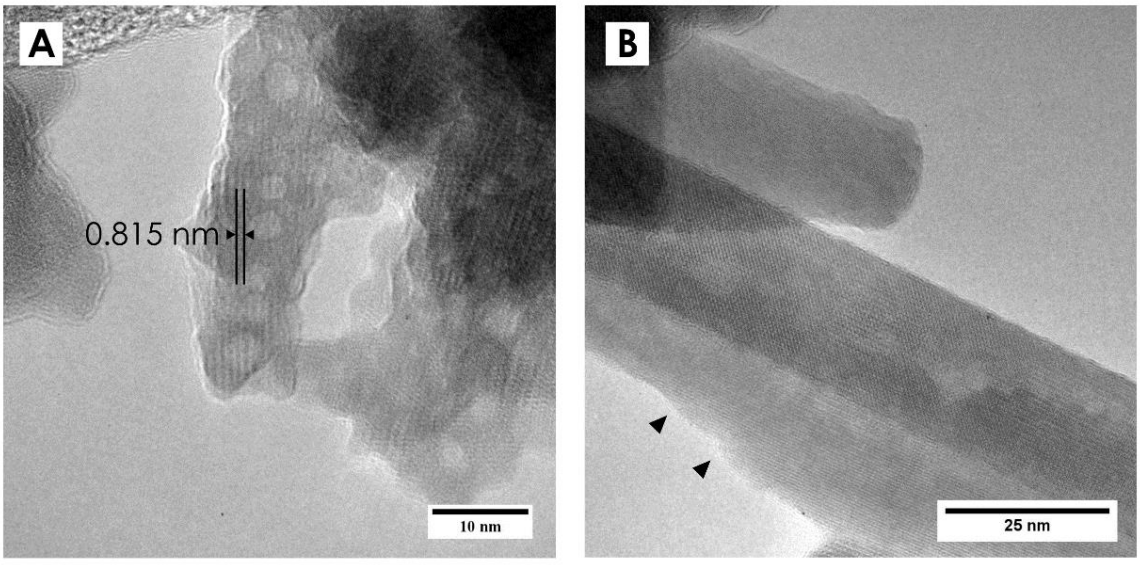

Figure 5.7. HRTEM micrographs of FHA samples. (A) 0.815 nm fringes in FHA 5m sample. (B) stepped surfaces (marked by arrows) along *a*-*b* planes in FHA 4h sample.

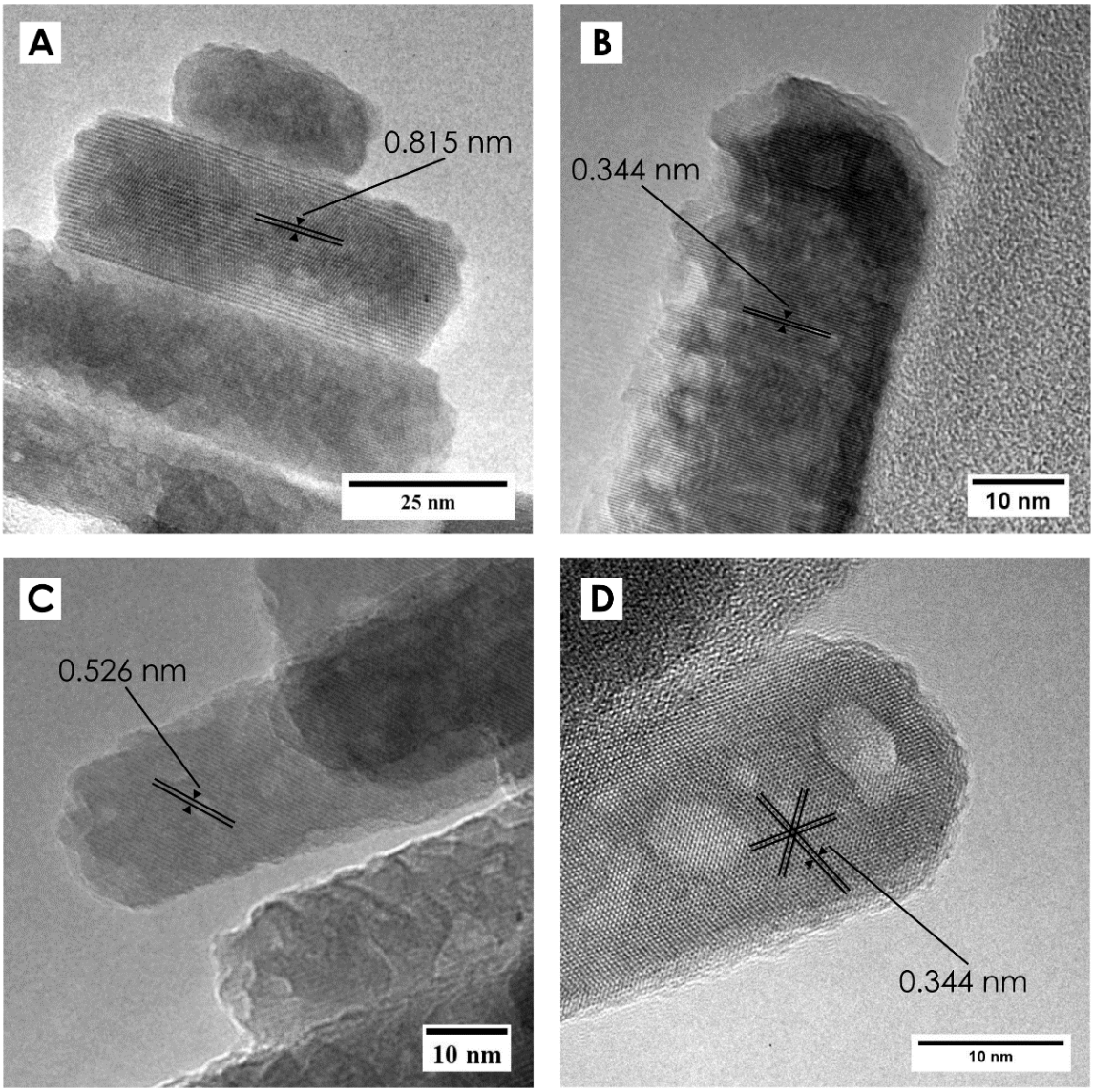

Figure 5.8. HRTEM micrographs of FHA samples. (A) 0.815 nm fringes that run along nanocrystal length. (B) 0.344 nm fringes orthogonal to nanocrystal length. (C) 0.526 nm fringes tilted 45 degrees to nanocrystal main axis. (D) Hexagonal fringe pattern with 0.344 spacing. Micrographs are taken from FHA 4h sample.

The isotropy of FHA and HA nanoparticles was evaluated by synchrotron small angle X-ray scattering. The SAXS scattering curves of FHA 4h and HA 4h are reported in Figure 5.9. The two materials present different curve shapes, suggesting different morphologies. The shape of the SAXS curve is mainly influenced by the structure and form factors associated to the thickness of the nanoparticles. For this reason it was chosen to adopt a lamellar model to fit the SAXS curves. Thickness and their standard deviation values (as calculated from the polydispersity values) are reported in Table 5.4.

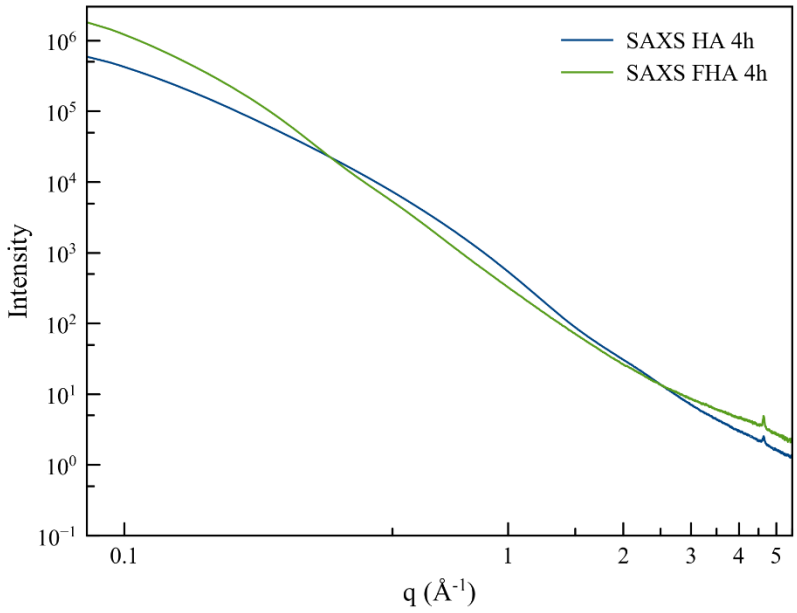

Figure 5.9. SAXS curve of FHA 4h (dark green line) and HA 4h (dark blue line).

Table 5.4. Mean thickness (T) of the samples extracted as lamellar fitting of SAXS data.

Sample	T
	(nm)
HA – 5m	6,8 ± 3,2
HA – 30m	7,1± 5,0
HA – 4h	5,5 ± 1,7
FHA – 5m	8,9 ± 6,2
FHA – 30m	7,1 ± 2,3
FHA – 4h	11,3 ± 7,1

The validity of the fitting was confirmed by comparing the thickness of HA calculated by SAXS to the values reported by Delgado-Lòpez *et. al.* by using synchrotron WAXS data and AFM [12]. Thickness of FHA nanoparticles is higher than HA nanoparticles, in particular at 4h of maturation. The thickness data confirm that FHA is more isotropic than HA, and evinces that FHA has a rod morphology, in contrast to HA that has a lamellar morphology.

5.1.4 Conclusions

In this work the precipitation of fluorine doped FHA nanorods has been carried out by thermal decomplexing reaction of Ca^{2+}/Cit/PO_4^{3-}/F^- solutions. Citrate-FHA nanocrystals have a peculiar rod-like morphology that closely resembles the morphology of dental enamel HA nanocrystals [46]. Interestingly, this morphology occurs due to the presence of fluoride ions in the reaction media, since fluoride-free HA nanocrystal have a different morphology and are nano-platelets. According to our data, fluoride ions plays different roles during the crystallization. First, their presence accelerates the crystallization kinetic and promotes nanocrystal growth and structural ordering as compared to the fluoride-free system. Second, F^- substitution of OH^- ions determined a shrinking of the crystal lattice parameters along the *a*(*b*) cell axis of ≈ 0.005 nm. Third, the crystal lattice distortion hindered the citrate adsorption, leading to lower citrate content in FHA compared to HA. Fourth, the hindered citrate adsorption leads to a thinner citrate-stabilized non-apatitic hydrated layer typical of citrate-apatites. Fifth, FHA has nanorod morphology instead of nano-platelet morphology of citrate-HA due to a less-oriented crystal growth [12, 14, 17]. Thus, the results presented therein suggest that the bioinspired citrate-FHA nanorods have different physico-chemical properties from HA and can be promising nanomaterials for advanced nanomedical applications.

5.2 Influence of small dicarboxylic acids on the formation of calcium phosphate nanoparticles

5.2.1 Introduction

As previously mentioned, the effect of citrate ions on HA crystallization is to bind selectively to the (1 0 -1 0) face of HA crystals, inhibiting the crystal growth along this direction and inducing HA nanocrystals to aggregate by attachment of citrate-free (0 0 0 1) faces, forming crystals elongated along the crystallographic *c*-axis [17]. Xie and Nancollas have proposed that the selectivity of citrate to the (1 0 -1 0) crystal face in HA is due to the fact that in this face the spacing between Ca^{2+} ions (0,320 nm or 0,688 nm) matches with either the spacing between the centers of two neighbor $-COO^-$ citrate groups (0,320 nm) or the distance between the two terminal carboxylates of citrate (0,688 nm) [11]. Consequently, citrate strongly binds selectively to the (1 0 -1 0) crystal face inhibiting its further growth. The citrate adsorption on other crystal faces is less favored since Ca distances do not match well with the carboxylate distances of the citrate. Accordingly, after crystal growth the (1 0 -1 0) crystal face became predominant, resulting in thin nanocrystals with plate-like morphology. In order to deepen the comprehension on the influence of small molecules on HA crystallization mechanisms, in the work reported in this subchapter HA was synthesized in presence of molecules that share the same backbone structure of citrate – two carboxylic groups separated by three carbon atoms. These molecules will be called thereafter as "dicarboxylic acids". After an initial screening of more than ten dicarboxylic acids (data not shown), it was chosen to use hydroxycitrate and glutaric acid. In comparison with citrate, these two dicarboxylic acids possess one extra hydroxyl group or lack one carboxyl and hydroxyl group, respectively (Figure 5.10). The aim of the work was to understand how small variations in the citrate functional groups can affect growth and size of HA nanocrystals and to observe if the "mismatch" in the number of functional groups influences the characteristics of the synthesized HA crystals while keeping the two terminal carboxylates of citrate at the same relative distance.

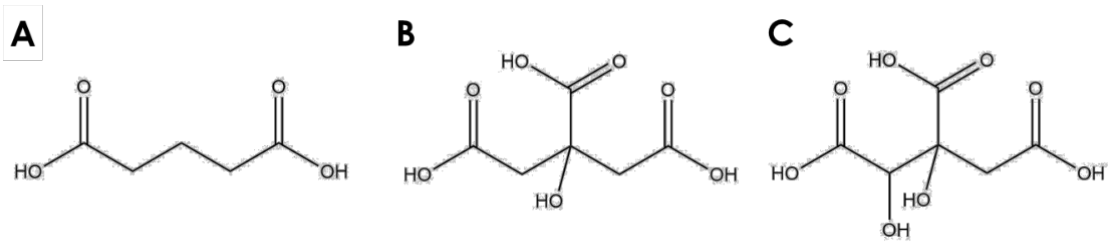

Figure 5.10. Molecular structure of (A) glutaric acid, (B) citric acid and (C) hydroxycitric acid.

5.2.2 Sample preparation and characterization

Dry powder dicarboxylic acid-HA was synthesized as reported in the work of Delgado-López *et al.* [14]. Namely, two solutions (1:1 v/v, 200 mL total) of (i) 100 mM $CaCl_2$ + 400 mM *X* and (ii) 120 mM Na_2HPO_4 were mixed at room temperature. *X* is the dicarboxylic acid, that was Na_3(Cit) (thereafter named Cit), glutaric acid (named Glr), or K_3(CitOH) (named CitOH). In the case of Glr-HA the solution (i) was basified with NaOH until pH 8.5 was reached in order to deprotonate the glutaric acid and produce sodium glutarate. In the case of CitOH-HA the final volume was of 20 mL total. After mixing the solution was thermostated at 80 °C under agitation in a water bath for five maturation times – that is to say 5 minutes, 2 hours, 4 hours, 16 hours and 24 hours. After maturation the particles were repeatedly washed with ultrapure water by centrifugation at 7000 rpm for 10 min and then freeze-dried overnight at -50 °C under a vacuum of 3 mbar. The lyophilized powders were subsequently grinded and sieved with a 50 μm sieve in order to achieve a uniform granulometry.

Physical-chemical characterizations

Samples were characterized by PXRD, Rietveld refinement, TEM, chemical composition analyses, FT-IR, electrophoretic potential, and TGA. Interpretation of the four TGA weight losses were attributed to adsorbed water (from room temperature to 150 °C), structural water (from 150 to 350 °C), dicarboxylic acid (from 350 to 700 °C) and carbonate (from 700 to 1000 °C).

Multiphase Rietveld refinement of OCP and HA of Glr-HA 5m PXRD pattern was performed with the software TOPAS5 [47]. The weight composition of the two phases and unit cell parameters were refined during Rietveld refinement considering a two-phase system, using tabulated atomic coordinates [31, 48]. Symmetrized spherical harmonics were used to cope, phenomenologically, with anisotropic peak broadening effects due to the anisotropic crystal shape.

5.2.3 Results and discussion

Chemical composition

The chemical composition of the samples is reported in Table 5.5. Cit-HA had the typical composition of a biomimetic, non-stochiometric calcium deficient hydroxyapatite – Ca/P ratio lower than 1.67, presence of carbonate ions, water (structural and adsorbed) and citrate ions. The presence of carbonate ions in the material was due to atmospheric CO_2 dissolved in the mother solution during synthesis. These data are in agreement with previous works on Cit-HA [14]. After 2 hours of maturation the chemical composition became stable and was unaltered for the rest of the maturation process. With maturation the amount of structural water, carbonate as well as of citrate slightly decreased due to the progressive reduction of the surface non-apatitic hydrated layer typical of Cit-HA, previously described by Rey *et al.* [43, 44].

Glr-HA has a Ca/P molar ratio that is slightly lower than Cit-HA (1.45), but with a higher Ca and P content. This was due to a lower content of dicarboxylic acid, carbonate and water in comparison with Cit-HA. Glr-HA 5m sample has a different Ca/P ratio, but it must be taken into account that this sample is composed by more than one calcium phosphate crystal phase (see below). Therefore in Glr-HA 5m the measured chemical composition was not representative of the apatitic component and can not be taken used for comparisons. With maturation there were no significant differences in composition.

CitOH-HA at long maturation time had a chemical composition and Ca/P ratio similar to Cit-HA, but was remarkably different at short maturation time. At early maturation the Ca/P ratio was higher (approx. 1.75) and decreased during crystallization. At the same time with maturation there was a significant increase of Ca and P content and a decrease of dicarboxylic acid, carbonate and water. In comparison to the other two dicarboxylic acids CitOH-HA had a notably higher content of dicarboxylic acid, water and carbonate ions at every maturation time.

In conclusion, the chemical composition analyses suggest that Cit-HA, Glr-HA and CitOH-HA have the same structural composition as apatitic materials, as evinced by the very similar Ca/P molar ratios, and their stoichiometry did not change significantly after the first moments of maturation. On the other hand, the three of dicarboxylic acids-covered apatites differentiated remarkably in the content of non-apatitic ions, with Glr-HA that had less dicarboxylic acid and water than Cit-HA while CitOH-HA had more dicarboxylic acid, water and carbonate ions than Cit-HA.

The surface charge of the samples was markedly different between the three classes of HAs. Compared to Cit-HA (that had a ζ-potential of approx. -17 mV), the presence of CitOH led to a comparable surface charge while Glr has a significantly less negative one (≈ -6 mV). According to Ivachenko *et al.* and Hu *et al.*, when the citrate is bound on the surface of hydroxyapatite it tends to expose outside its apolar $–CH_2–$ region, decreasing the hydrophilicity of HA [11, 41]. This hypothesis could explain the trend observed for surface charge of CitOH- and Glr- bound HA, since Glr has less polar groups compared to Cit and then induces a higher hydrophobicity. Considering the progressive maturation the surface charge had no significant changes in Cit-HA and CitOH-HA samples, while in Glr-HA is observed a progressive increase of ζ-potential toward more negative values.

Table 5.5. Chemical composition of the powder samples and ζ-potential.

Sample	Ca[a] (wt%)	P[a] (wt%)	Ca/P[a] (mol)	Dicarboxylic acid[b] (%wt.)	Carbonate[b] (%wt)	Structural water[b] (%wt)	ζ-potential[c] (mV)
Cit-HA 5m	26.4±0.2	13.2±0.2	1.54±0.02	2.0±0.2	1.1±0.1	4.1±0.4	-15.5±0.6
Cit-HA 2h	28.4±0.5	14.3±0.3	1.53±0.02	1.9±0.2	0.8±0.1	2.9±0.3	-13.4±0.3
Cit-HA 4h	28.1±0.1	14.3±0.1	1.53±0.01	1.6±0.2	0.7±0.1	3.0±0.3	-15.8±0.5
Cit-HA 16h	28.7±0.6	15.0±0.3	1.48±0.01	1.5±0.1	0.2±0.1	3.3±0.3	-17.1±0.3
Cit-HA 24h	28.4±0.5	14.3±0.4	1.53±0.02	1.5±0.2	0.8±0.1	2.5±0.3	-16.5±0.3
CitOH-HA 5m	24.3±0.8	10.8±0.7	1.74±0.07	9.4±0.9	3.4±0.3	6.9±0.7	-17.1±1.0
CitOH-HA 2h	24.1±0.5	10.7±0.3	1.75±0.02	8.5±0.9	3.8±0.4	7.9±0.8	-17.4±0.9
CitOH-HA 4h	30.4±0.5	16.2±0.4	1.45±0.04	6.4±0.6	2.2±0.2	6.9±0.7	-15.9±1.0
CitOH-HA 16h	28.0±0.1	14.5±0.3	1.50±0.03	4.1±0.1	0.6±0.1	6.1±0.6	-18.0±1.0
CitOH-HA 24h	28.3±0.5	14.1±0.6	1.52±0.02	2.8±0.3	0.7±0.1	7.6±0.8	-16.1±0.7
Glr-HA 5m[d]	29.4±0.2	17.5±0.1	1.30±0.01	1.7±0.2	-	3.6±0.4	-1.9±0.2
Glr-HA 2h	31.6±1.0	17.2±0.4	1.42±0.01	0.7±0.1	0.5±0.1	0.9±0.1	-1.5±0.1
Glr-HA 4h	32.3±1.1	17.4±0.4	1.43±0.01	0.4±0.1	0.5±0.1	0.9±0.1	-2.3±0.4
Glr-HA 16h	33.4±0.8	17.9±0.3	1.44±0.01	0.6±0.1	0.6±0.1	1.6±0.1	-3.9±0.4
Glr-HA 24h	31.7±0.9	16.9±0.6	1.45±0.03	0.4±0.1	0.9±0.1	1.4±0.1	-5.7±0.4

(a) Quantified by ICP-OES; (b) Quantified by TGA; (c) Measured by DLS; (d) Since Glr-HA 5m is a multiphase material, the chemical composition is not representative of the HA component.

Spectroscopic characterization

The representative FT-IR spectra of the samples at 24h of maturation are reported in Figure 5.11. All the samples displayed a main broad band at 1030 cm^{-1} with shoulders at 1046 and 1075 cm^{-1} due to the triply degenerated anti-symmetric stretching mode of PO_4 groups (ν_3PO_4). Other bands are present at 960 cm^{-1} (symmetric stretching mode ν_1PO_4) and at 603, 576 (as a shoulder) and 565 cm^{-1} (triply degenerated bending mode ν_4PO_4). These vibrational bands are coherent with an apatitic material. Additionally, the spectra also showed bands at 3567 and 630 cm^{-1} that corresponds to the stretching and librational modes of the apatitic hydroxyl groups, respectively [39].

The presence of carbonate ions observed in TGA analysis was confirmed in all the samples by the presence of weak bands in the 860 – 880 cm^{-1} range [40]. In the 1650 – 1350 cm^{-1} range were present the signals of carboxylate ions and water. In the case of Cit-HA, the bands in this range showed peaks located at ca. 1640, 1597, 1445, and 1410 and 1400 cm^{-1}. The sub-bands at ca. 1400 and ca. 1597 cm^{-1} were assigned respectively to $\nu_{sym}OCO$ and $\nu_{asym}OCO$ signal of citrate ions coordinated to Ca^{2+} cations on the HA surface [41]. The sub-bands at 1445 and 1410 cm^{-1} were attributed to carbonate ions in B-type substitution (CO_3 occupying PO_4 sites). The 1640 cm^{-1} component was attributed to adsorbed water.

Also Glr-HA showed similar bands in this region, but with different relative intensities. Water and carbonate bands were still present at 1640, 1460 and 1417 cm^{-1}, respectively, while the bands associated to the dicarboxylic acid were negligible in accordance with compositional data.

Remarkably, in CitOH-HA the situation was the opposite, where the bands in the 1650 – 1350 cm^{-1} range were more intense and dominated by the components at ca. 1400 and ca. 1597 cm^{-1}, that means to say the dicarboxylic acid components. In both cases the FT-IR spectra confirmed the compositional data, indicating that Glr-HA had less dicarboxylic acid and water while CitOH-HA had more dicarboxylic acid, water and carbonate, in comparison to Cit-HA. In addition, CitOH-HA ν_4PO_4 peaks were less resolved and had a broader FWHM compared to the other materials, suggesting a more disordered crystal structure [14, 49].

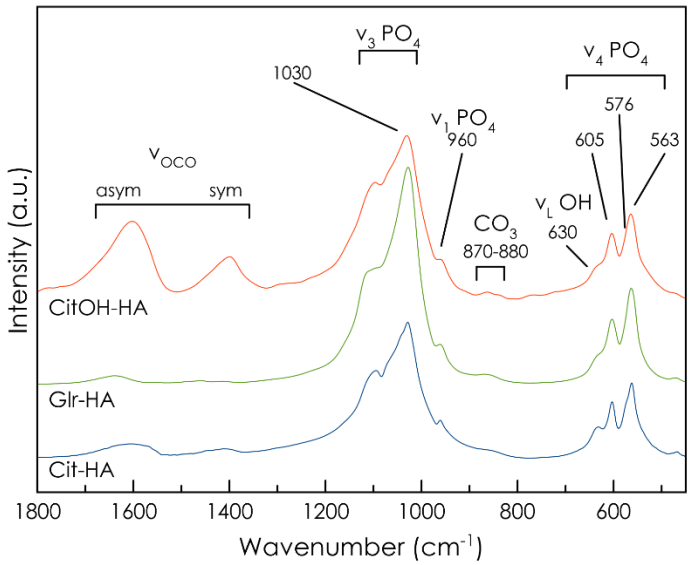

Figure 5.11. FT-IR spectra of Cit-HA 24h (blue line), Glr-HA 24h (green line) and CitOH-HA 24h (red line).

Crystallographic characterization

The PXRD patterns of all the samples are reported in Figure 5.12A-C. All the Cit-HA and CitOH-HA samples showed the typical diffraction peaks of HA as single phase (ASTM Card file No. 9-432). In particular, the most characteristics reflections appeared at 25.87° that corresponds to the crystallographic plane (002), and a broad peak centered at 32° that is due to the triplet at 31.77°, 32.19°, and 32.90°, which correspond to planes (211), (112), and (300). The other main peaks that were indexed are present at 39.81°, 46.71°, 49.46°, and 53.14°, which correspond to the planes (310), (222), (213), and (004), respectively [20]. In the cases of Cit-HA and CitOH-HA the diffraction peaks were broad and poorly defined, suggesting the presence of nanocrystals with a relatively low degree of crystal order at every maturation time [14]. A progressive peak sharpening with maturation was observed in all the samples. Peak sharpening evinced that with maturation the nanocrystals grew in size and improved their structural order.

Glr-HA, interestingly, was different. At 5 minutes of maturation the material was not composed only by HA, but there were several peaks that were indexed as octacalcium phosphate (OCP, $Ca_8H_2(PO_4)_6{\cdot}5H_2O$, marked with * in Figure 5.12C). Multiphase Rietveld refinement (Figure 5.12D) evinced that the composition of the samples was 33 wt.% HA and 67 wt.% OCP (R_{wp} = 5,792). This is a remarkable finding, since OCP is a common precursor of HA when prepared from wet precipitation process, but it is never present when HA is prepared in presence of citrate. It is thought that citrate stabilizes the ACP precursor formed in the beginning of the crystallization process and leads ACP to the direct conversion into HA as non-classical crystallization mechanism, instead of passing through the metastable phases DCPD

(dicalcium phosphate dihydrate, $CaHPO_4 \cdot 2H_2O$) -> OCP -> HA as predicted by Ostwald's rule of phases [17]. This implies that glutarate had not the same effect of citrate since at low crystallization time a significative amount of OCP was detected. However, it must be stated that Glr had an influence on OCP -> HA conversion since in citrate-free samples OCP was detected also at four hours of maturation [12] while in Glr-HA hydroxyapatite was present as single phase already at two hours of maturation. Glr-HA samples peaks were always more defined than Cit/CitOH-HA peaks at every maturation time, suggesting the presence of more ordered or bigger nanocrystals in this material.

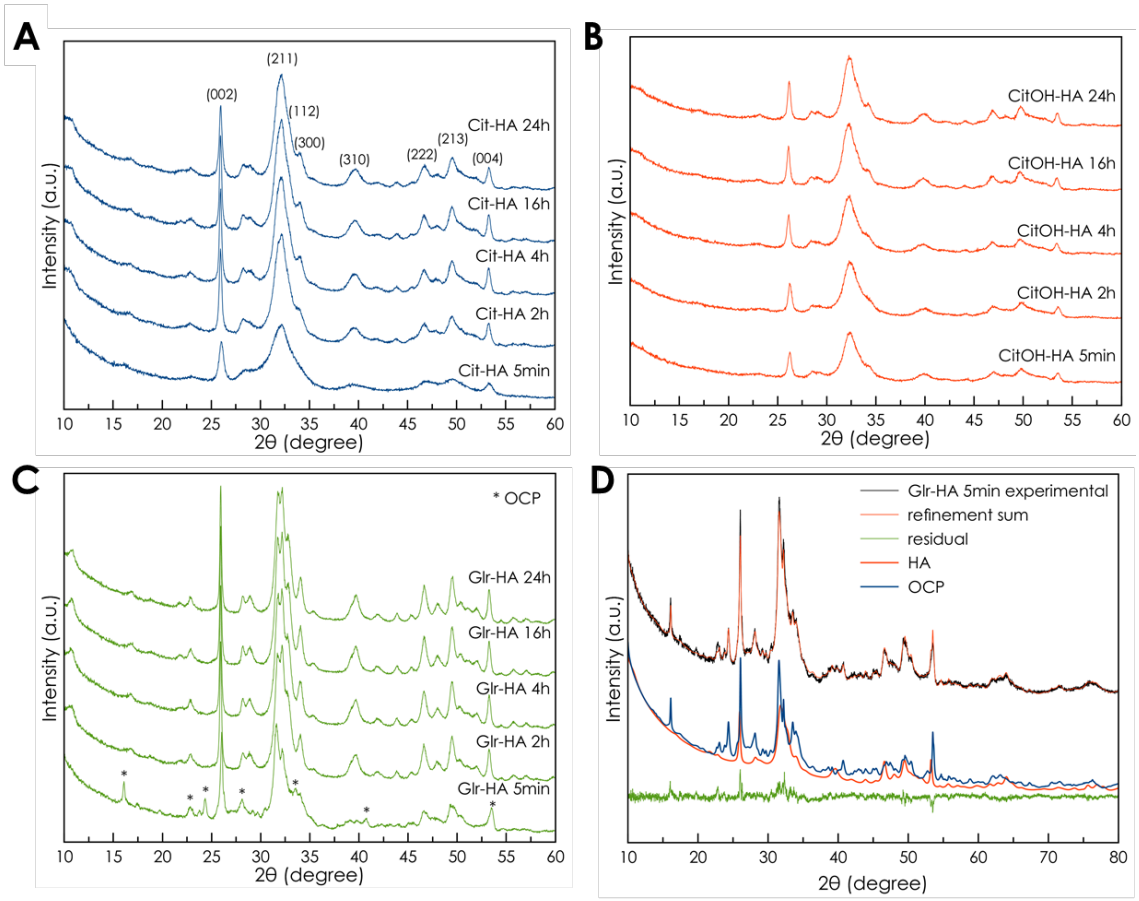

Figure 5.12. PXRD diffractograms of (A) Cit-HA at several maturation times, (B) CitOH-HA at several maturation times, and (C) Glr-HA at several maturation times. (D) represent the phase quantification analysis by Rietveld refinement of Glr-HA 5min.

The unit cell parameters extracted by Rietveld refinement show that the *c* unit cell parameter of Cit-HA and Glr-HA samples (Table 5.6) were comparable, while the *c* unit cell parameter of CitOH-HA samples were notably longer. This suggests that in CitOH-HA there was a less ordered structure along this direction compared to Cit-HA and Glr-HA, or that the presence of CitOH induced an expansion of the

unit cell along the *c*-direction, a more unlikely hypothesis. On the other hand, the *a* unit cell parameter of all the samples were comparable with no clear distinctions. The unit cell parameters shrank with maturation due to progressive structure ordering. The validity of these data extracted from laboratory PXRD has been validated by comparison with unit cell parameters of Cit-HA extracted from synchrotron WAXS data by Delgado-Lòpez *et al.* [12]. In all the samples, the *c* cell parameter was closer to the reference value (highly crystalline HA (PDF card 00-055-0592)) than *a*, suggesting a more ordered structure along this direction for all the samples.

The dimensions of the crystal domains were estimated along the $D_{(00l)}$ and $D_{(hk0)}$ directions, that correspond to the longest and the shortest axes of the hexagonal HA crystal, respectively. It was chosen to use the non-overlapped (002) and (310) reflections for $D_{(00l)}$ and $D_{(hk0)}$, respectively. The estimated crystal domain sizes are reported in Table 5.6. It must be taken into account that for Glr-HA 5 min the values are less precise since in this sample two crystal phases were present and was not possible to extract correctly peak broadening, since HA (002) and (310) peaks are convoluted with OCP peaks.

The average size of crystal domains of the samples along the c-axis ($D_{(002)}$) are notably different from one dicarboxylic acid to the other. Cit-HA $D_{(002)}$ grew steadily with maturation from ca. 20 nm to ca. 50 nm, in coherence with previous literature reports [14]. Glr-HA, interestingly, has significantly higher values at every time point, ranging from ca. 40 nm to ca. 65 nm. On the other hand, CitOH-HA showed an opposite behavior with shorter crystal domains between ca. 20 and ca. 30 nm. Also for $D_{(310)}$ the trend was the same, with a progressive domain growth with maturation time and relative domain size that followed the Glr-HA > Cit-HA > CitOH-HA order at almost every time point. For all the materials the values of $D_{(002)}$ are higher than those of $D_{(310)}$, as evinced by the $D_{(002)}/D_{(310)}$ aspect ratio, indicating that the crystals were elongated along the *c*-axis. No clear trend was observed for $D_{(002)}/D_{(310)}$ ratio in relationship to dicarboxylic acid nature.

Table 5.6. Crystallographic parameters of the samples extracted by Rietveld refinement.

	a-b cell parameters	c cell parameter	$D_{(002)}$	$D_{(310)}$	$D_{(002)}/D_{(310)}$
Sample	(Å)	(Å)	(nm)	(nm)	
Cit-HA 5m	9,536	6,891	17	3,1	5,5
Cit-HA 2h	9,463	6,887	35,4	6,2	5,7
Cit-HA 4h	9,455	6,886	41,4	8,8	4,7
Cit-HA 16h	9,453	6,884	43,6	9,2	4,7
Cit-HA 24h	9,446	6,887	50,1	13,6	3,7
CitOH-HA 5m	9,464	6,896	23,1	5	4,8
CitOH-HA 2h	9,462	6,895	23,8	4,6	5,2
CitOH-HA 4h	9,456	6,892	27,2	4,7	5,8
CitOH-HA 16h	9,451	6,889	29,9	6,7	4,5
CitOH-HA 24h	9,459	6,892	29,6	7,7	3,8
Glr-HA 5m	9,470	6,885	36,7	10,9	3,4
Glr-HA 2h	9,462	6,885	60,2	10,1	6,0
Glr-HA 4h	9,460	6,884	61,4	11,3	5,4
Glr-HA 16h	9,459	6,884	66,5	12,2	5,5
Glr-HA 24h	9,457	6,886	64,9	12,1	5,4

Nanoparticles morphology

Figure 5.13 represents TEM micrographs of Cit-HA, Glr-HA and CitOH-HA at 24h of maturation. TEM micrographs of Cit-HA nanocrystals are in accordance with previous works [14, 17, 22]. Cit-HA is composed of nanocrystals with platy morphology, whose main axis corresponds to the crystallographic *c* axis, and possess an average length of 65 ± 15 nm and an average width of 13 ± 3 nm at 24h of maturation (Figure 5.13A).

In comparison, CitOH-HA nanocrystals present a similar elongated morphology, but are much smaller and are less regular, and at 24h of maturation have an average length of 26 ± 9 nm and an average width of 8 ± 2 nm (Figure 5.13B). Glr-HA instead has an opposite morphology, with bigger nanocrystals that are less elongated (Figure 5.13C). In this latter material some particles appear as extremely long and thin and have higher electron density. It is thought that these particles were probably parallel to electron beam during image acquisition, and thus in these cases the thickness of the nanoparticles was observed. Therefore Glr-HA is composed by wide, ultra-thin nanoplatelets at 24h of maturation, with

an average length of 104 ± 36 nm, an average width of 47 ± 24 nm and an average thickness of 9 ± 2 nm.

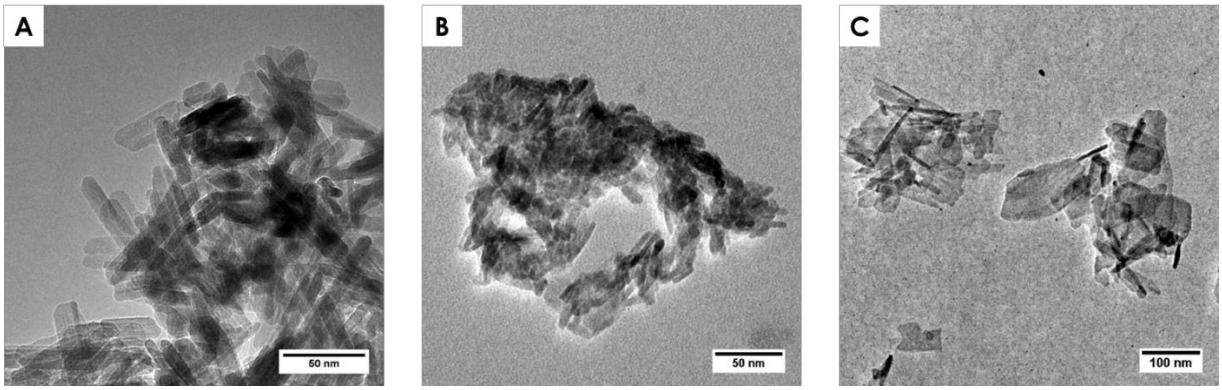

Figure 5.13. TEM micrographs of (A) Cit-HA 24h, (B) Glr-HA 24h, and (C) CitOH-HA 24h.

The mean length (L) along the longest axis, the mean width (W) orthogonal to L, and the mean aspect ratio (R, i.e., the ratio between L and W) of single nanocrystals were estimated from TEM observations and are reported in table 5.7 in comparison with the corresponding crystals domains.

Table 5.7. Mean length (L), mean width (W), and mean aspect ratio (R) of the samples.

Sample	L^a	$D_{(002)}{}^b$	W^a	$D_{(310)}{}^b$	R^a	$D_{(002)}/D_{(310)}{}^b$	T^a
	(nm)	(nm)	(nm)	(nm)			(nm)
Cit-HA 24h	65,3 ± 14,5	50,1	13,2 ± 2,8	13,6	5,0	3,7	-
CitOH-HA 24h	26,3 ± 9,4	29,6	8,0 ± 2,4	7,7	3,3	3,8	-
Glr-HA 24h	103,6 ± 36,2	64,9	46,5 ± 23,9	12,1	2,2	5,4	9,0 ± 2,4

[(a)] Measured from TEM micrographs. The mean value and the standard deviation were calculated measuring the sizes of 50 particles from different experiments. [(b)] Estimated from Rietveld refinement.

Comparing the nanocrystals dimensions and the crystals domains it is clear that in Cit-HA and CitOH-HA the average TEM values are comparable to the crystallite domains, albeit are slightly higher. This suggest that for these two materials the nanoparticles were composed by single nanocrystals, and the slight size difference might be due to the presence of the non-apatitic hydrated layer that does

contribute to nanoparticles dimension but does not contribute to crystal domains dimension. Glr-HA, remarkably, showed a great discrepancy between TEM values and the crystallite domains, especially regarding nanoparticles width. This suggest that Glr-HA nanoparticles are polycrystalline, composed of several nanocrystals fused side-by-side.

5.2.4 Conclusion

The three dicarboxylic acid Cit, Glr, and CitOH were proved to strongly influence HA crystallization with different outcomes, even if the three molecules share a very similar molecular structure. Cit-HA was used as the reference compound, since it is an already-known biomimetic nanomaterial that has been successfully used for several biomedical applications [18-22, 25]. Comparing the other dicarboxylic acid to Cit-HA in terms of nanocrystals morphology, dimensions, chemical composition and crystallographic properties is it evinced that:

- CitOH strongly inhibited HA crystallization, forming single elongated nanocrystals with small dimensions, low structural order, and higher content of non-apatitic molecules. Crystallization pathway seemed to be similar to Cit-HA, with direct conversion from amorphous precursor to hydroxyapatite.
- Glr inhibited crystallization less than Cit-HA forming thin and wide nanoplatelets that were polycrystalline. Glr-HA nanocrystals had bigger dimensions, higher structural order, low content of non-apatitic molecules, and low surface charge. Crystallization pathway seemed to follow Ostwald's rule of phases, with formation of an OCP precursor that converted to HA.

Therefore, these preliminary data suggest that the whole arrangement of citrate molecular structure influences HA crystallization. This is in contrast with the current theory, that ascribes the effect of citrate only to the spacing between the terminal carboxyl groups. More work is required to fully elucidate the crystallization mechanism of CitOH-HA and Glr-HA, but some preliminary explanation can be drawn.

In CitOH, the presence of the extra hydroxyl group leads to a stronger/more abundant binding of the dicarboxylic acid to HA surface, leading to inhibited nanoparticle growth, less crystal order but keeping the same preferential surface binding of Cit. This was shown by TEM micrographs, crystal domains estimation and PXRD peaks broadening. In addition, the molecule stabilizes the non-

apatitic hydrated layer, as evinced by the compositional analyses and the FT-IR spectra. The different behavior of CitOH suggest that the binding efficiency was not related only to the calcium-chelating carboxylate moieties, but also to hydroxyl groups. Moreover, this molecule further confirms that the non-apatitic hydrate layer is stabilized by citrate molecules, since with CitOH the non-apatitic components are more abundant.

In Glr, the lack of the central polar units leads to a weaker/less abundant binding of the dicarboxylic acid to HA surface, maybe due to the lack of a favorable conformation of the adsorbed molecule on HA surface. This leads to a lesser control and inhibition of HA crystallization, and HA was formed after conversion of OCP. The consequence was that HA growth was less oriented along *c*-axis, as evinced by morphological and crystallographic data. Moreover, Glr-HA nanocrystal tended to aggregate perpendicularly to their main axis forming polycrystalline nanoplatelets. The aggregation could be due to a reduced particle-particle electrostatic repulsion caused by the lower surface charge of Glr-HA.

In conclusion, these preliminary data suggest that all the functional groups of citrate are strongly involved in the regulation of HA crystallization. This has been proved by substituting citrate with hydroxycitrate or glutarate during HA crystallization. The addition/removal of polar central functional groups strongly changed the effect of the dicarboxylic acid on HA crystallization. More studies are needed to evaluate the whole crystallization pathway of CitOH-HA and Glr-HA, to finely understand the effect of dicarboxylic acids molecular structure on HA crystallization, and to confirm the hypotheses stated above. Nevertheless, this work highlights the potentialities on the control that can be exerted on HA formation and on the possible ways to produce advanced nanomaterials with tailored physicochemical properties.

5.3 Bibliography

1. Gómez-Morales, J., et al., *Progress on the preparation of nanocrystalline apatites and surface characterization: overview of fundamental and applied aspects.* Progress in Crystal Growth and Characterization of Materials, 2013. **59**(1): p. 1-46.
2. Iafisco, M. and J.M. Delgado-López, *Apatite: Synthesis, Structural Characterization, and Biomedical Applications*. 2014: Nova Science Publishers, Incorporated.
3. Ferraz, M., F. Monteiro, and C. Manuel, *Hydroxyapatite nanoparticles: a review of preparation methodologies.* Journal of Applied Biomaterials and Biomechanics, 2004. **2**(2): p. 74-80.
4. Norton, J., et al., *Recent developments in processing and surface modification of hydroxyapatite.* Advances in Applied Ceramics, 2006. **105**(3): p. 113-139.
5. Lin, K., C. Wu, and J. Chang, *Advances in synthesis of calcium phosphate crystals with controlled size and shape.* Acta biomaterialia, 2014. **10**(10): p. 4071-4102.
6. Sadat-Shojai, M., et al., *Synthesis methods for nanosized hydroxyapatite with diverse structures.* Acta biomaterialia, 2013. **9**(8): p. 7591-7621.
7. Newcomb, C.J., et al., *The role of nanoscale architecture in supramolecular templating of biomimetic hydroxyapatite mineralization.* Small, 2012. **8**(14): p. 2195-2202.
8. Wang, A., et al., *Size-controlled synthesis of hydroxyapatite nanorods in the presence of organic modifiers.* Materials Letters, 2007. **61**(10): p. 2084-2088.
9. Gómez-Morales, J., et al., *Amino acidic control of calcium phosphate precipitation by using the vapor diffusion method in microdroplets.* Crystal Growth & Design, 2011. **11**(11): p. 4802-4809.
10. Neira, I.S., et al., *An effective morphology control of hydroxyapatite crystals via hydrothermal synthesis.* Crystal Growth and Design, 2008. **9**(1): p. 466-474.
11. Hu, Y.-Y., A. Rawal, and K. Schmidt-Rohr, *Strongly bound citrate stabilizes the apatite nanocrystals in bone.* Proceedings of the National Academy of Sciences, 2010.
12. Delgado-López, J.M., et al., *Crystal Size, Morphology, and Growth Mechanism in Bio-Inspired Apatite Nanocrystals.* Advanced Functional Materials, 2014. **24**(8): p. 1090-1099.
13. Jiang, W., et al., *Atomic force microscopy reveals hydroxyapatite− citrate interfacial structure at the atomic level.* Langmuir, 2008. **24**(21): p. 12446-12451.
14. Delgado-López, J.M., et al., *Crystallization of bioinspired citrate-functionalized nanoapatite with tailored carbonate content.* Acta biomaterialia, 2012. **8**(9): p. 3491-3499.
15. Sakhno, Y., et al., *A step toward control of the surface structure of biomimetic hydroxyapatite nanoparticles: effect of carboxylates on the {010} P-rich/Ca-rich facets ratio.* The Journal of Physical Chemistry C, 2015. **119**(11): p. 5928-5937.
16. Chatzipanagis, K., et al., *Crystallization of citrate-stabilized amorphous calcium phosphate to nanocrystalline apatite: a surface-mediated transformation.* CrystEngComm, 2016. **18**(18): p. 3170-3173.
17. Iafisco, M., et al., *The growth mechanism of apatite nanocrystals assisted by citrate: relevance to bone biomineralization.* CrystEngComm, 2015. **17**(3): p. 507-511.
18. Di Mauro, V., et al., *Bioinspired negatively charged calcium phosphate nanocarriers for cardiac delivery of MicroRNAs.* Nanomedicine, 2016. **11**(8): p. 891-906.
19. Miragoli, M., et al., *Inhalation of peptide-loaded nanoparticles improves heart failure.* Science translational medicine, 2018. **10**(424): p. eaan6205.
20. Martínez-Casado, F.J., et al., *Bioinspired Citrate–Apatite Nanocrystals Doped with Divalent Transition Metal Ions.* Crystal Growth & Design, 2015. **16**(1): p. 145-153.
21. Sandhöfer, B., et al., *Synthesis and preliminary in vivo evaluation of well-dispersed biomimetic nanocrystalline apatites labeled with positron emission tomographic imaging agents.* Acs Applied Materials & Interfaces, 2015. **7**(19): p. 10623-10633.

22. Delgado-López, J.M., et al., *Bio-inspired citrate-functionalized apatite thin films crystallized on Ti–6Al–4V implants pre-coated with corrosion resistant layers.* Journal of Inorganic Biochemistry, 2013. **127**: p. 261-268.
23. Šupová, M., *Substituted hydroxyapatites for biomedical applications: a review.* Ceramics International, 2015. **41**(8): p. 9203-9231.
24. Gómez Morales, J., et al., *Bioinspired Mineralization of Type I Collagen Fibrils with Apatite in Presence of Citrate and Europium Ions.* Crystals, 2019. **9**(1): p. 13.
25. Gómez-Morales, J., et al., *Luminescent biomimetic citrate-coated europium-doped carbonated apatite nanoparticles for use in bioimaging: physico-chemistry and cytocompatibility.* RSC Advances, 2018. **8**(5): p. 2385-2397.
26. ten Cate, J.M., *Contemporary perspective on the use of fluoride products in caries prevention.* Br Dent J, 2013. **214**(4): p. 161-167.
27. Qu, H. and M. Wei, *The effect of fluoride contents in fluoridated hydroxyapatite on osteoblast behavior.* Acta biomaterialia, 2006. **2**(1): p. 113-119.
28. Wiegand, A., W. Buchalla, and T. Attin, *Review on fluoride-releasing restorative materials—fluoride release and uptake characteristics, antibacterial activity and influence on caries formation.* Dental Materials, 2007. **23**(3): p. 343-362.
29. Ten Cate, J. and J. Featherstone, *Mechanistic aspects of the interactions between fluoride and dental enamel.* Critical Reviews in Oral Biology & Medicine, 1991. **2**(3): p. 283-296.
30. Sun, R., et al., *Controlled synthesis and enhanced luminescence of europium-doped fluorine-substituted hydroxyapatite nanoparticles.* CrystEngComm, 2013. **15**(17): p. 3442-3447.
31. Roche, K.J. and K.T. Stanton, *Measurement of fluoride substitution in precipitated fluorhydroxyapatite nanoparticles.* Journal of Fluorine Chemistry, 2014. **161**: p. 102-109.
32. Rodríguez-Lorenzo, L.M., J.N. Hart, and K.A. Gross, *Structural and chemical analysis of well-crystallized hydroxyfluorapatites.* The Journal of Physical Chemistry B, 2003. **107**(33): p. 8316-8320.
33. Hammersley, A., *FIT2D: an introduction and overview.* European Synchrotron Radiation Facility Internal Report ESRF97HA02T, 1997. **68**: p. 58.
34. Kotlarchyk, M. and S.H. Chen, *Analysis of small angle neutron scattering spectra from polydisperse interacting colloids.* The Journal of chemical physics, 1983. **79**(5): p. 2461-2469.
35. Kotlarchyk, M., R.B. Stephens, and J.S. Huang, *Study of Schultz distribution to model polydispersity of microemulsion droplets.* The Journal of Physical Chemistry, 1988. **92**(6): p. 1533-1538.
36. Jha, L., et al., *Preparation and characterization of fluoride-substituted apatites.* Journal of Materials Science: Materials in Medicine, 1997. **8**(4): p. 185-191.
37. Rodrıguez-Lorenzo, L., J. Hart, and K. Gross, *Influence of fluorine in the synthesis of apatites. Synthesis of solid solutions of hydroxy-fluorapatite.* Biomaterials, 2003. **24**(21): p. 3777-3785.
38. Tonsuaadu, K., et al., *A review on the thermal stability of calcium apatites.* Journal of Thermal Analysis and Calorimetry, 2011. **110**(2): p. 647-659.
39. Koutsopoulos, S., *Synthesis and characterization of hydroxyapatite crystals: a review study on the analytical methods.* Journal of Biomedical Materials Research: An Official Journal of The Society for Biomaterials, The Japanese Society for Biomaterials, and The Australian Society for Biomaterials and the Korean Society for Biomaterials, 2002. **62**(4): p. 600-612.
40. Antonakos, A., E. Liarokapis, and T. Leventouri, *Micro-Raman and FTIR studies of synthetic and natural apatites.* Biomaterials, 2007. **28**(19): p. 3043-3054.
41. Ivanchenko, P., et al., *On the surface effects of citrates on nano-apatites: evidence of a decreased hydrophilicity.* Scientific Reports, 2017. **7**(1): p. 8901.

42. Socrates, G., *Infrared and Raman characteristic group frequencies: tables and charts*. 2004: John Wiley & Sons.
43. Rey, C., et al., *Physico-chemical properties of nanocrystalline apatites: implications for biominerals and biomaterials.* Materials Science and engineering: C, 2007. **27**(2): p. 198-205.
44. Rey, C., et al., *Bone mineral: update on chemical composition and structure.* Osteoporosis International, 2009. **20**(6): p. 1013-1021.
45. Selvig, K.A., *Periodic lattice images of hydroxyapatite crystals in human bone and dental hard tissues.* Calcified Tissue Research, 1970. **6**(1): p. 227-238.
46. Robinson, C., J. Kirkham, and R.C. Shore, *Dental enamel formation to destruction*. 2017: CRC press.
47. Coelho, A., *Topas Academic V5.* Coelho Software, 2012.
48. Espanol, M., et al., *Investigation of the hydroxyapatite obtained as hydrolysis product of α-tricalcium phosphate by transmission electron microscopy.* CrystEngComm, 2010. **12**(10): p. 3318-3326.
49. Bala, Y., et al., *Time sequence of secondary mineralization and microhardness in cortical and cancellous bone from ewes.* Bone, 2010. **46**(4): p. 1204-1212.

Chapter 6. Conclusion and future perspectives

Advancement of medical science generates a continuous demand of new advanced materials that possess excellent properties, minimize costs and side effects, and possess high efficacy to be applied in a plethora of different applications. Nanomaterials have the potentiality to fulfil all these features, and for this reason the field is in continuous expansion.

In this Ph. D. work, new calcium phosphate nanoparticles have been designed with the purpose to produce advanced nanomaterials for medical application. The applications listed in this Ph. D. Thesis vary significantly, spacing from cardiac drug delivery to dental regeneration, but nanoparticles design approach is the same. It was decided to use a "*functional by design*" approach, which means to design and tailor the nanoparticles properties to fulfill a specific function. This innovative approach is complex since CaP NPs are "made" with bottom-up methods and thus their properties are dependent to the synthesis process. However, scientific progresses reported in literature and in this Ph. D. Thesis have shown that is possible to finely control nanoparticles formation and growth and thus the functional by design approach can be applied.

In detail, in this Ph. D. work several different CaP NPs were prepared. For the treatment of cardiovascular diseases the nanoparticles were required to (i) have extra-small dimensions in order to cross the alveolar-capillary barrier in the lung and rapidly translocate to the myocardium lung, (ii) to possess a strong negative surface charge to avoid aggregation and to provide cellular permeability via the membrane internalization, and (iii) to deliver and protect the therapeutic molecule from immediate enzymatic degradation. For this reason CaP NPs synthesis was designed to encapsulate the payload during nanoparticles formation, and a strong excess of citrate was used both as regulator of nanoparticles growth and as negatively-charged surfactant using a biomineralization-inspired strategy. The results presented in this Ph. D. work show that these CaP NPs were able to cross the pulmonary barrier and penetrate cardiomyocytes *in vivo*, successfully delivering their payload and exerting a therapeutic action. This work is also a proof of concept demonstration of the efficacy of CaP NPs for drug delivery, and it is expected that in the future will be developed CaP NPs tailored to treat different diseases, target organs, and administration approaches.

In the case of dental regeneration, it was needed a material (i) able to dissolve quickly, generating a Ca^{2+}, PO_4^{3-}, and F^- supersaturation in the mouth environment while at the same time (ii) able to

attach to enamel/dentin surface and spontaneously form HA. CaP NPs synthesis was designed to produce amorphous calcium phosphate nanoparticles doped with F, Mg, and Sr ions. The amorphous phase was chosen to provide the fast dissolution rates and the doping ions were added to improve dental remineralization. In addition, citrate was use to stabilize dry ACP at room temperature and to control the degradation and crystallization kinetics. The results have proven that these CaP NPs dissolve and crystallize to hydroxyapatite at the same time when in contact with human oral environment, and this leads to an efficient enamel remineralization and dentinal tubules occlusion. The perspective is the development of several CaP NPs-based dental regeneration products tailored to treat different teeth diseases – enamel demineralization, dentinal hypersensitivity, bacterial biofilm formation, sealant detachment, etc.

Part of this Ph. D. work was devoted to deepen the "toolbox" for controlling CaP NPs properties. Nanoparticles properties are related to several factors involved in the synthesis and to achieve a specific result is a complex process, especially in the "functional by design" approach. For this reason there is a strong need to deeply understand the effect of growth regulators like dopants and template molecules on CaP NPs formation. Therefore in this Ph. D. work the effect of citrate, dicarboxylic acids, and fluoride ions on CaP NPs crystallization has been studied. The data shows that these molecules have a complex and interdependent effect on nanoparticles crystallization and the thoughtful use of these regulators can yield CaP NPs products with very different properties. Even if further studies are needed the overall picture suggest that the methods to control CaP NPs formation are extremely powerful and versatile and the number of custom CaP NPs that can be made is going to increase in the future.

In conclusion, in this Ph. D. Thesis are represented some of the potentialities and versatility of CaP NPs, where the nanoparticles can be designed knowingly to fulfill specific functions. It is foreseen that with the increase of knowledge on CaP NPs formation and methods to regulate nanoparticles properties the number of calcium phosphate nanoparticles for medical and non-medical application of will rise, prompting even more interest in nanomaterial science.

Peer-reviewed journal publications

1. F. Carella, L. Degli Esposti, D. Barreca, G. A. Rizzi, G. Martra, P. Ivanchenko, G. Escolano Casado, J. Gomez Morales, J. M. Delgado Lopez, A. Tampieri and M. Iafisco (2019), *Role of citrate on the formation of enamel-like calcium phosphate oriented nanorod arrays,* CrystEngComm, 21, 4684-4689.
2. L. Marchiol, A. Filippi, A. Adamiano, L. Degli Esposti, M. Iafisco, A. Mattiello, E. Petrussa, E. Braidot (2019), *Influence of Hydroxyapatite Nanoparticles on Germination and Plant Metabolism of Tomato (Solanum lycopersicum L.): Preliminary Evidence*, Agronomy, 9(4), 161.
3. J. Gómez Morales, R. Fernández Penas, C. Verdugo-Escamilla, L. Degli Esposti, F. Oltolina, M. Prat, M. Iafisco, J. Fernández Sánchez (2019), *Bioinspired Mineralization of Type I Collagen Fibrils with Apatite in Presence of Citrate and Europium Ions,* Crystals, 9(1), 13.
4. M. Iafisco, L. Degli Esposti, G. B. Ramírez-Rodríguez, F. Carella, J. Gómez-Morales, A. C. Ionescu, E. Brambilla, A. Tampieri, J. M. Delgado-López (2018). *Fluoride-doped amorphous calcium phosphate nanoparticles as a promising biomimetic material for dental remineralization*, Scientific reports, 8(1), 17016.
5. L. Degli Esposti, F. Carella, A. Adamiano, A. Tampieri, M. Iafisco (2018), *Calcium phosphate-based nanosystems for advanced targeted nanomedicine.* Drug development and industrial pharmacy, 44(8), 1223-1238.
6. M. Miragoli, P. Ceriotti, M. Iafisco, M. Vacchiano, N. Salvarani, A. Alogna, P. Carullo, G. B. Ramirez-Rodríguez, T. Patrício, L. Degli Esposti, F. Rossi, F. Ravanetti, S. Pinelli, R. Alinovi, M. Erreni, S. Rossi, G. Condorelli, H. Post, A. Tampieri, D. Catalucci (2018). *Inhalation of peptide-loaded nanoparticles improves heart failure.* Science translational medicine, 10(424), eaan6205.
7. S. Setua, M. Jaggi, M. M Yallapu, S. C Chauhan, A. Danilushkina, H. Lee, I. S. Choi, R. Fakhrullin, L. Degli Esposti, A. Tampieri, M. Iafisco, M. Shevtsov, G. Multhoff (2018). *Targeted and theranostic applications for nanotechnologies in medicine*. In Nanotechnologies in Preventive and Regenerative Medicine (pp. 399-511). Elsevier publisher.
8. L. Degli Esposti, F. Carella, M. Iafisco (2018). *Inorganic nanoparticles for theranostic use*. In Electrofluidodynamic Technologies (EFDTs) for Biomaterials and Medical Devices (pp. 351-376). Woodhead Publishing.

9. M. Bianchi, L. Degli Esposti, A. Ballardini, F. Liscio, M. Berni, A. Gambardella, S. CG Leeuwenburgh, S. Sprio, A. Tampieri, M. Iafisco (2017). *Strontium doped calcium phosphate coatings on poly (etheretherketone)(PEEK) by pulsed electron deposition*. Surface and Coatings Technology, 319, 191-199.

Manuscripts under review

1. L. Degli Esposti, A. Adamiano, A. Tapieri, G. B. Ramirez-Rodriguez, Y. Sakhno, G. Martra, D. Siliqi, C. Giannini, J. M. Delgado Lopez, M. Iafisco *"Citrate assisted synthesis of fluorine doped enamel-like hydroxyapatite nanorods"* submitted
2. R. Nadar, N. Asokan, L. Degli Esposti, A. Curci, A. Barbanente, L. Schlatt, U. Karst, M. Iafisco, N. Margiotta, M. Brand, J. J. J. P. van den Beucken, M. Bornhäuser, S. C. G. Leeuwenburgh (2019) *Preclinical Evaluation of Platinum-Loaded Hydroxyapatite Nanoparticles for Treatment of Bone Metastases*, submitted
3. H. Y. Yoon, J. G. Lee, L. Degli Esposti, M. Iafisco, P. J. Kim, S. G. Shin, J-R. Jeon, A. Adamiano "*Synergistic release of crop nutrients and stimulants from hydroxyapatite nanoparticles coated with humic substances: towards a multifunctional nano-fertilizer*" submitted

Scientific contributions to congresses

1. L. Degli Esposti, F. Carella, A. Adamiano, P. Carullo, A. Tampieri, M. Miragoli, D. Catalucci, M. Iafisco *Inhalable Calcium Phosphate Nanoparticles for Cardiac Drug Delivery,* ESB – 29th European Conference on Biomaterials, Dresden, Germany, 2019 – Best Student Poster Award
2. L. Degli Esposti *Citrate-stabilized amorphous calcium phosphate doped with fluoride ions: a new biomimetic nanomaterial in dentistry* TRACE-2: Tissue Regeneration: Advanced Ceramics and Composites, Loveno di Menaggio, Italy, 2019
3. L. Degli Esposti, F. Carella, J. Gómez-Morales, A. C. Ionescu, E. Brambilla, G. B. Ramírez-Rodríguez, A. Tampieri, J. M. Delgado-López, M. Iafisco *Citrate-stabilized amorphous calcium phosphate doped with fluoride ions: a new biomimetic nanomaterial in dentistry* BioMaH – Biomaterials and Novel Technologies for Healthcare, 2nd International Biennial Conference, Frascati, Italy, 2018.

4. L. Degli Esposti, F. Carella, A. Adamiano, A. Tampieri, J. M. Delgado-López, H. Amenitsch, M. Iafisco, *Influence of citrate and other small dicarboxylic acids on hydroxyapatite nanocrystal nucleation, growth and surface properties.* ISMANAM2018 - 25th International Symposium on Metastable, Amorphous and Nanostructured Materials, Roma, Italy, 2018.
5. L. Degli Esposti, J. Gómez-Morales, G. B. Ramírez-Rodríguez, A. Tampieri, J. M. Delgado-López, M. Iafisco *Citrate stabilized amorphous calcium phosphate doped with fluoride ions: a promising material for enamel remineralization* Bioceramics29, Toulouse, France, 2017.
6. L. Degli Esposti, F. Carella, A. Adamiano, A. Tampieri, M. Iafisco *Bio-Inspired Synthetic Strategies of Hydroxyapatite Nanocrystals: from Biomineralization to Regenerative Medicine and Drug Delivery,* Conferenza di dipartimento CNR, Alghero, Italia, 2017.
7. L. Degli Esposti, A. Adamiano, P. Colombo, F. Buttini, D. Catalucci, M. Iafisco *Improved calcium phosphate nanoparticles for targeted cardiac drug delivery* SIB, Milano, Italy, 2017

Acknowledgements

Funding

The Author is grateful to the following funding agencies:

- European Union for the EU H2020 RIA-funded project "CUPIDO – Cardiac Ultraefficient nanoParticles for Inhalation of Drug prOducts" (GA No. 720834).
- CERIC-ERIC Consortium for the access to SAXS experimental facility and financial support.

Scientific contribution

The Author is grateful to the following researchers:

- Dr. Heinz Amenitsch and Dr. Barbara Sartori of ELETTRA SAXS Austrian beamline for SAXS data collection and interpretation.
- Dr. Paola Ceriotti, Dr. Marco Vacchiano, Dr. Nicolò Salvarani, Dr. Pierluigi Carullo, Dr. Michele Miragoli, and Dr. Daniele Catalucci of Humanitas Clinical and Research Center and Dr. Alessio Alogna and Dr. Heiner Post of Berlin Charité Institute of Health for *in vitro* and *in vivo* test of drug-loaded CaP NPs.

- Dr. Andrei C. Ionescu and Dr. Eugenio Brambilla of the Oral Microbiology Laboratory of Galeazzi Orthopedic Institute for the *in vitro* test of ACP NPs.
- Dr. Cinzia Giannini and Dr. Dritan Siliqi of Institute of Crystallography, National Research Council for SAXS data fitting.
- Dr. José Manuel Delgado-Lopez of University of Granada for materials characterizations.
- Dr. Alessio Adamiano, Dr. Elisabetta Campodoni, Ms. Andreana Piancastelli of the Institute of Science and Technology for Ceramics, National Research Council for materials characterizations.